

DISSERTATION

SPIN CURRENTS AND FERROMAGNETIC RESONANCE IN MAGNETIC THIN FILMS

Submitted by

David Ellsworth

Department of Physics

In partial fulfillment of the requirements

For the Degree of Doctor of Philosophy

Colorado State University

Fort Collins, Colorado

Summer 2017

Doctoral Committee:

Advisor: Mingzhong Wu

Robert Camley
Carmen Menoni
Carl Patton
James Sites

Copyright by David Ellsworth 2017

All Rights Reserved

ABSTRACT

SPIN CURRENTS AND FERROMAGNETIC RESONANCE IN MAGNETIC THIN FILMS

Spin currents represent a new and exciting phenomenon. There is both a wealth of new physics to be discovered and understood, and many appealing devices which may result from this area of research. To fully realize the potential of this discipline it is necessary to develop new methods for realizing spin currents and explore new materials which may be suitable for spin current applications. Spin currents are an inherently dynamic phenomenon involving the transfer of angular momentum within and between different thin films. In order to understand and optimize such devices the dynamics of magnetization must be determined.

This dissertation reports on novel approaches for spin current generation utilizing the magnetic insulators yttrium iron garnet (YIG) and M-type barium hexagonal ferrite (BaM). First, the light-induced spin Seebeck effect is reported for the first time in YIG. Additionally, the first measurement of the spin Seebeck effect without an external magnetic field is demonstrated. To accomplish this the self-biased BaM thin films are utilized.

Second, a new method for the generation of spin currents is presented: the photo-spin-voltaic effect. In this new phenomenon, a spin current may be generated by photons in a non-magnetic metal that is in close proximity to a magnetic insulator. On exposure to light, there occurs a light induced, spin-dependent excitation of electrons in a few platinum layers near the metal/magnetic insulator interface. This excitation gives rise to a pure spin current which flows in the metal. This new effect is explored in detail and extensive measurements are carried out to confirm the photonic origin of the photo-spin-voltaic effect and exclude competing effects.

In addition to the spin current measurements, magnetization dynamics were probed in thin films using ferromagnetic resonance (FMR). In order to determine the optimal material configuration for magnetic recording write heads, FMR measurements were used to perform damping studies on a set of FeCo samples with different numbers of lamination layers. The use of lamination layers has the potential to tune the damping in such films, while leaving the other magnetic properties unchanged.

Finally, the sensitivity of the vector network analyzer FMR technique was improved. The use of field modulation and lock-in detection, along with the background subtraction of a Mach-Zehnder microwave interferometer working as a notch filter, is able to increase the sensitivity and lower the background noise of this measurement technique. This improved system opens the possibility of probing previously difficult samples with extremely low signals.

ACKNOWLEDGEMENTS

This dissertation is the result of the contributions and support of everyone who has given me advice, assistance, or encouragement over the last six years. I would like to express my gratitude to the following people in particular.

I would like to thank my advisor, Professor Mingzhong Wu, for his inspiration, advice, and guidance throughout my time at CSU. He was always available, despite his busy schedule, to share his wisdom on anything from research to writing.

I am also grateful to all of the colleagues I have had the pleasure to work with. Lei Lu helped to introduce me to magnetic research and patiently answered my novice questions. My other fellow graduate students, Houchen Chang, Praveen Janantha, Yiyang Sun, Jason Liu, Grant Riley, Daniel Richardson, and John Raguse were a fantastic source of discussion and assistance. Carl Patton and Boris Kalinikos provided sage advice.

Without the physics department and its excellent faculty and staff, I would not have had the opportunity to pursue my Ph.D. In particular, Wendy Johnson has gone above and beyond to support my graduate studies.

My sincere gratitude is extended to my family and friends, who encouraged me throughout my studies. Thank you to my parents, who supported me no matter what. Above all else, I would like to thank my wife, Heather. Her support, love, and understanding were essential in my studies and I would not be where I am today without her.

TABLE OF CONTENTS

ABSTRACT.....	ii
ACKNOWLEDGEMENTS.....	iv
CHAPTER 1 Introduction.....	1
1.1 Background and motivation.....	1
1.2 Dissertation outline.....	2
CHAPTER 2 Spin currents.....	5
2.1 Introduction to spin currents.....	5
2.2 Spin Hall effect.....	7
2.3 Spin pumping.....	10
2.4 Spin Seebeck effect.....	12
2.5 Summary.....	16
CHAPTER 3 Spin Seebeck effect in magnetic insulators.....	18
3.1 Overview.....	18
3.1.1 Yttrium iron garnets.....	19
3.1.2 Barium hexagonal ferrites.....	20
3.2 Experimental setup.....	21
3.3 Results and discussions.....	23
3.4 Summary.....	27

CHAPTER 4	Photo-spin-voltaic effect in Pt/magnetic insulator heterostructures	29
4.1	Overview	29
4.2	Experimental setup.....	31
4.3	Demonstration of the photo-spin-voltaic effect	32
4.3.1	Different illumination configurations	34
4.3.2	Different magnetic insulator films.....	36
4.4	Wavelength dependence of the photo-spin-voltaic effect.....	37
4.5	Physical mechanism of the photo-spin-voltaic effect	41
4.6	Comparison of experiment and theory.....	43
4.7	Mixing of the photo-spin-voltaic and spin Seebeck effects.....	48
4.8	Summary	52
CHAPTER 5	Distinction between the photo-spin-voltaic and spin Seebeck effects	53
5.1	Overview	53
5.2	Measurements of light-induced, concurrent PSV and SSE.....	54
5.3	Separation of entangled photo-spin-voltaic and spin Seebeck effect signals.....	57
5.4	Responses of photos-spin-voltaic and spin Seebeck effect signals to different lights ...	59
5.5	Control measurements.....	62
5.5.1	Measurement repeatability.....	63
5.5.2	Impact of light incidence direction	64
5.5.3	Comparison of voltage sign in different metals.....	67

5.5.4	Temperature measurements	68
5.5.5	Optical properties of the samples.....	70
5.6	Summary	71
CHAPTER 6 Ferromagnetic resonance.....		73
6.1	Introduction	73
6.2	Magnetization precession.....	74
6.2.1	Uniform motion	74
6.2.2	Modifications to the torque equation	76
6.2.3	Torque equation solution	78
6.3	Ferromagnetic resonance.....	80
6.4	Shorted waveguide and cavity FMR	83
6.5	Vector network analyzer ferromagnetic resonance	85
6.5.1	Susceptibility in terms of S-parameters	87
6.5.2	Fitting of experimental data	90
6.6	Summary	91
CHAPTER 7 Effects of lamination on damping of FeCo thin films.....		93
7.1	Overview	93
7.2	Experimental setup.....	94
7.3	Measurement results.....	95
7.4	Impact of lamination on film properties.....	98

7.5	Summary	100
CHAPTER 8 Increased sensitivity VNA-FMR measurement technique.....		101
8.1	Overview	101
8.2	Experimental setup.....	102
8.3	FMR measurement results with different systems	106
8.4	Comparison of different ferromagnetic resonance techniques.....	110
8.5	Summary	111
CHAPTER 9 Summary		112
9.1	Summary	112
9.2	Future work	113
References.....		115

CHAPTER 1 Introduction

1.1 Background and motivation

The electron has formed the foundation for technology in the 21st century. From computing to data storage, as well as telecommunications, signal and information processing, and scientific instrumentation, the electron is central to how our world operates. While electronics started by utilizing the charge property of the electron, increasingly the spin property of the electron has become a key feature. Thus, the study of electron spins has become important, both fundamentally and technologically.

The work performed for this dissertation was motivated primarily by two important problems. First, as the capabilities and capacities of electronic devices grow, so too does their power consumption. To address this issue, there is the possibility of driving electrons with different spins to flow in opposite directions, producing a pure spin current. Such spin currents do not suffer from the same high losses associated with charge currents, and can potentially be used to inspire a new generation of spin electronics, or spintronics, with significantly lower power consumption.

By developing new methods to generate and detect spin currents this new field of spintronics may be advanced. Additionally, the discovery of new material systems will also help propel this research and allow for further device optimization. Currently one common magnetic materials used in spintronics is yttrium iron garnet ($\text{Y}_3\text{Fe}_5\text{O}_{12}$, YIG), due to its very low intrinsic damping. While this is a very good candidate material, other magnetic insulators, for example M-type barium hexagonal ferrite ($\text{BaFe}_{12}\text{O}_{19}$, BaM), have unique advantages of their own, such as large anisotropy and remanence magnetization, which will enable new devices and applications.

The second motivation for the research presented here is the fact that the motion of magnetic moments does not follow a simple linear path. Instead the fundamental motion of magnetic moments is circular, like that of a precessing top. This property is of fundamental importance in magnetic recording, which stores information as a sequence of “up” or “down” magnetic moments. When one wishes to change a bit the magnetization needs to change its orientation, and how it does that involves the field of magnetization dynamics.

Of particular importance is the ferromagnetic resonance (FMR) measurement technique, which uses a small transverse AC magnetic field to drive the magnetization precession. The frequency of the AC magnetic field, and thus that of magnetization precession is in the microwave frequency range. By measuring the power absorption of the driving microwaves, it is possible to examine the relaxation, or damping, processes at work in a magnetic material. As devices become ever smaller it is important that measurement techniques improve apace to properly characterize and provide valuable feedback on how best to improve them.

1.2 Dissertation outline

This dissertation presents new work on the generation of spin currents and measurement of magnetization dynamics. The first half of this dissertation focuses on spin currents and presents three experiments in this field. The second half focuses on characterizing magnetization dynamic using FMR and is supported by two experimental projects.

Chapter 2 introduces the concept of spin currents and how they differ from traditional charge currents. The current means for generating and detecting spin currents are discussed, including the spin Hall effect, the inverse spin Hall effect, microwave spin pumping, and the spin Seebeck effect. The relative advantages and shortcomings of each method are addressed.

The spin Seebeck effect is examined in greater detail in Chapter 3, which gives experimental evidence of the effect in Pt/YIG and Pt/BaM thin films. The use of BaM in this work is the first report of the spin Seebeck effect in a self-biased magnetic insulator. This work is also the first demonstration of the spin Seebeck effect using light as a heat source.

Chapter 4 introduces an entirely new method for generating spin currents using unpolarized light in a Pt/YIG system: the photo-spin-voltaic (PSV) effect. In order to confirm this new effect, extensive measurements were carried out to exclude parasitic effects. Such measurements included temperature measurements, different illumination configurations, different magnetic insulator films, wavelength dependent measurements via optical filters, and other control measurements. A mechanism for the physical origin of the PSV effect is proposed and the experimental results are compared with the theoretical calculations, showing good agreement.

The PSV effect is further explored in Chapter 5. In this work, the PSV effect is experimentally demonstrated in additional nonmagnetic metals, including Pd, Au, and Cr. The PSV effect is also combined with the SSE and separated, introducing further evidence that the PSV effect is not of thermal origin. Finally, the wavelength dependence of the PSV effect in each metal is examined and shown to be rather different, indicating that the critical wavelength changes for different metals.

Chapter 6 gives an introduction to magnetization precession and the key experimental method for exploring magnetization dynamics – FMR. The mathematical framework for describing magnetization dynamics and damping are explained, including the Gilbert and Kittel equations. The experimental technique of FMR is described and the practical measurement methods of microwave cavity and vector network analyzer (VNA) FMR are discussed.

In Chapter 7 the effects of lamination on damping in FeCo thin films is studied using FMR. Films with no lamination, and with one, two, or three Al₂O₃ lamination layers are studied using shorted waveguide and cavity FMR techniques. The magnetic properties, including damping and anisotropy, of these films are determined through frequency- and field angle- dependent FMR measurements.

Chapter 8 shows how the sensitivity of the VNA-FMR measurement technique can be improved by utilizing field modulation and lock-in detection as well as background subtraction with the use of a microwave interferometer. The experimental data for cavity FMR, standard VNA-FMR, and the improved VNA-FMR techniques are compared, demonstrating the advantages of this new measurement method.

The final chapter, Chapter 9, summarizes the work completed in this dissertation and proposes several possible future investigations which utilize the discoveries and new techniques presented in this dissertation. Of note is potential work related to the PSV effect and utilizing the improved VNA-FMR measurement system.

CHAPTER 2 Spin currents

2.1 Introduction to spin currents

Electronics form the basis of many modern technologies. It is used both to power and control a wide variety of different devices at all length scales and to transfer, process, and store data. As the demand for more and better electronics grows, the demand for more power consumption grows as well. One of the primary avenues of loss in electronic devices is resistance induced heating due to the flow of charge current through channels with a finite resistance. Computing is one very power intensive technology sector, with one large data center consuming as much power as 25,000 individual households.^{1,2} Of this power consumption roughly half goes into the cooling of devices and systems.³

One approach to alleviate this large demand for energy is to reduce the amount of energy lost to resistance. In addition to using the charge property of the electron to enable devices it is also possible to use the electron's spin property. It is possible to drive electrons with different spins to flow in opposite directions, producing a so-called spin current. The different types of spin currents are shown schematically in Figure 2.1. The red spheres represent electrons moving in the direction of the green arrows. The electrons possess both a charge and a spin property. The spins are represented by the blue arrows, showing up- and down-spins. A typical charge current is shown in Figure 2.1(a). In this case the electrons are randomly spin polarized, with equal amounts of up-spins and down-spins. This results in a net flow of charge, represented by the orange arrow, and no net flow of spins. In the case where there are unequal amounts of up-spins and down-spins moving there will be both a net flow of charge and of spin, a so-called spin-polarized current. The

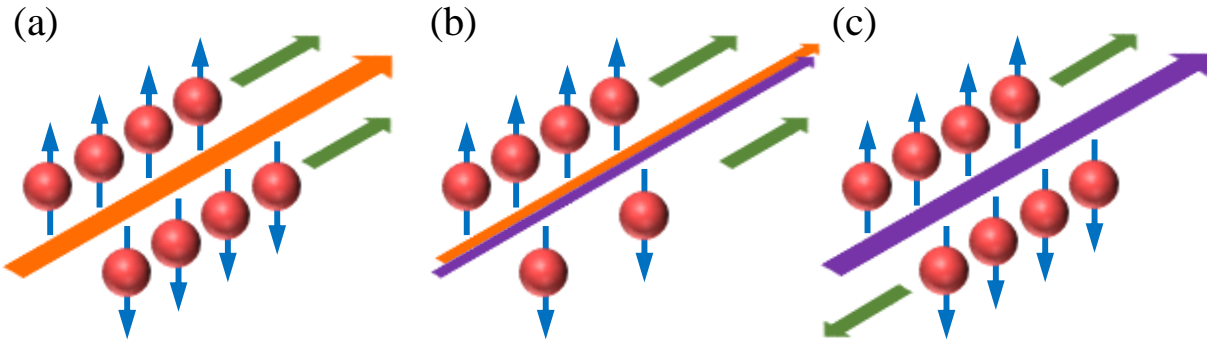


Figure 2.1 Different types of electric currents. The red spheres represent electrons with spin orientation shown in blue moving in the direction of the green arrows. (a) When equal amounts of up- and down-spins are traveling in the same direction, the result is a net flow of charge, hence a charge current, shown as the orange arrow. (b) In this case an unequal number of up- and down-spins are traveling in the same direction there is a net flow of both charge and spin, resulting in a spin-polarized current, represented by orange (charge) and purple (spin) arrows. (c) If equal amounts of up- and down-spin are flowing in opposite directions there is no net flow of charge but there is a net flow of spins, which is a pure spin current and is shown as the purple arrow.

case where there are more up-spins than down-spins flowing in a certain direction is represented in Figure 2.1(b), resulting in both a charge current, represented by the orange arrow, and a spin current, represented by the purple arrow. If equal amounts up-spins and down-spins are flowing in opposite directions there is no net flow of charge, but there is a net flow of spin. This case, known as a pure spin current, is shown in Figure 2.1(c), which shows that there is only a spin current, represented by the purple arrow.

When such pure spin currents are generated with no associated charge currents there are no losses associated with electrical resistance, thus it is possible to design a new generation of low-power devices harnessing the spin of the electron. This field has been called spin electronics, or spintronics, and represents an exciting new area of innovation.

The generation and detection of such spin currents, however, remains a challenging and pioneering research field. At present, there are three primary means of generating pure spin currents: the spin Hall effect, spin pumping, and the spin Seebeck effect. These three effects will

be covered in detail in this chapter. Each of these effects has both advantages and challenges as means of spin current generation. An entirely new method of spin current generation, the photo-spin-voltaic effect, will be discussed in detail in Chapters 4 and 5.

2.2 Spin Hall effect

The classical Hall effect, discovered by Edwin Hall in 1879, refers to the creation of an electric potential across a conductor which is transverse to an electric current and a magnetic field perpendicular to the current.⁴ A spin version of this effect was first proposed in 1971,⁵ first dubbed the spin Hall effect in 1999,⁶ and first demonstrated experimentally in 2012.⁷ In the spin Hall effect (SHE) when a charge current flows in a heavy metal with strong spin-orbit coupling, such as Pt or W, a spin-dependent accumulation of electrons is generated perpendicular to the current direction.⁸

The simple result of the SHE is a method to translate a charge current into a pure spin current, and, via the inverse effect, translate back from a pure spin current to a charge current. The SHE, and its inverse effect, are both important cornerstones of spintronics research because of their ability to convert between charge and spin currents. The SHE is critical not only for fundamental research, but also for the integration of spintronics with traditional electronics.

The typical explanation for the origin of the SHE is the spin-orbit coupling induced spin dependent scattering, however, other mechanisms have also been proposed.⁸ The influence of spin-orbit coupling can be explained by considering an electron interacting with a non-magnetic ion. It will experience an effective magnetic field

$$\mathbf{B} = -\frac{1}{c^2} \mathbf{v} \times \mathbf{E} = -\frac{1}{c^2} \mathbf{v} \times \left(\frac{kq}{r^3} \mathbf{r} \right) \quad 2.1$$

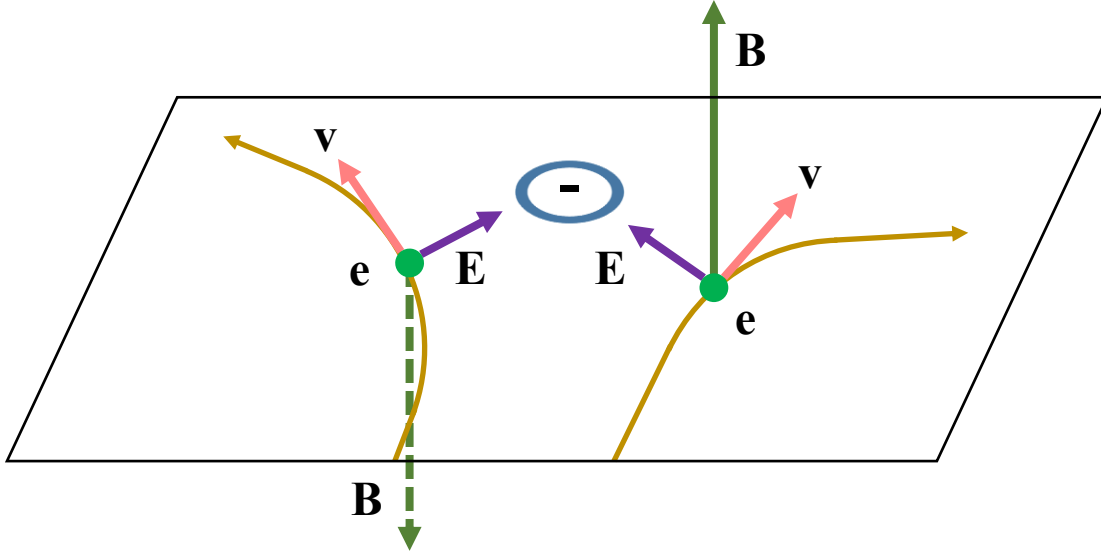


Figure 2.2 Schematic of electrons scattering from negatively charged ion. The electron experiences an effective magnetic field $\mathbf{B} \sim \mathbf{v} \times \mathbf{E}$ perpendicular to the path of the electron.

in the frame of the moving electron, where \mathbf{E} is the electric field of the ion, \mathbf{v} is the velocity of the electron, \mathbf{r} is the position vector of the electron relative to the ion, q is the charge of the ion, and k is Coulomb's constant. The scattering process due to the Lorentz force is shown schematically in Figure 2.2. If the electron spin is not exactly perpendicular to the trajectory plane, it will precess around \mathbf{B} during the scattering event. The Zeeman energy of the electron, in the frame of the electron, is

$$E_z = -\boldsymbol{\mu} \cdot \mathbf{B} = \frac{\mu_B k q}{c^2 r^3} (\mathbf{v} \times \mathbf{r}) \cdot \hat{\boldsymbol{\sigma}} \quad 2.2$$

where $\boldsymbol{\mu}$ is the magnetic moment of the electron which is pointing along $\hat{\boldsymbol{\sigma}}$, and μ_B is the Bohr magneton. Note, however, that the magnetic field, \mathbf{B} , is inhomogeneous in space because both \mathbf{v} and \mathbf{E} change as the electron moves along its path. For this reason, there is a spin-dependent force, which is proportional to the gradient of the Zeeman energy, acting upon the electron. This spin-dependent force is the origin of the spin Hall effect.

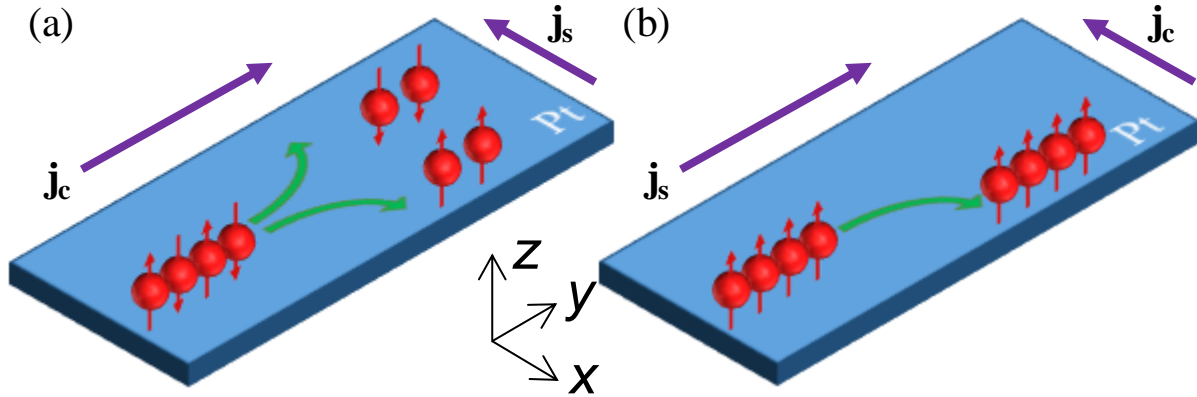


Figure 2.3 Diagram of spin Hall and inverse spin Hall effects. (a) A charge current with no spin polarization, \mathbf{j}_c , traveling in the y direction in Pt generates a spin current, \mathbf{j}_s , in the x direction via the spin Hall effect. (b) A pure spin current traveling in the y direction, \mathbf{j}_s , generates a charge current in the x direction, \mathbf{j}_c , via the inverse spin Hall effect.

The result of this spin-dependent force is an asymmetry in the scattering of electrons with opposite spins, where, in this case, spin-up electrons will mostly go to the right and spin-down electrons will mostly go to the left. The cumulative effect is the separation of spin-up and spin-down electrons, which will generate a pure spin current which is proportional to

$$\mathbf{j}_s \propto \Theta_{SH} \mathbf{j}_c \times \hat{\mathbf{v}} \quad 2.3$$

where \mathbf{j}_s is the spin current density, \mathbf{j}_c is the charge current density, and Θ_{SH} is the so-called spin Hall angle which is related to the strength of the spin-orbit coupling in the material.

The SHE is shown schematically in Figure 2.3(a) where a charge current, with no spin polarization traveling in the y direction, has its up-spins deflected to the left and the down-spins deflected to the right, creating a spin current in the x direction. Note that no external magnetic field is required to generate this spin current, only a charge current and a material with a strong spin-orbit interaction.

Typically, it is not possible to use traditional electronics equipment, such as a voltmeter, to detect a pure spin current, as there is no associated charge current. However, by utilizing the

inverse spin Hall effect (ISHE) a pure spin current can be converted to a charge current and detected by conventional means. The relationship for the ISHE can be obtained by inverting Equation 2.3

$$\mathbf{j}_c \propto \Theta_{SH} \mathbf{j}_s \times \hat{\mathbf{e}} \quad 2.4$$

Figure 2.3b) shows the case where a pure spin current, with up-spins flowing in the y direction, is converted to a charge current in the x direction. The down-spins, not shown in Figure 2.3, are flowing in the $-x$ direction and are also deflected in the same direction as the up-spins. Thus, a charge accumulation would develop in the x direction and thus a charge current, which may be detected by conventional electronic means. The inverse spin Hall effect is a very common method for detecting spin current, and will be utilized repeatedly in this work to detect spin currents generated by other methods, such as the spin Seebeck effect and photo-spin-voltaic effect.

While the SHE is an easy method for spin current generation and detection it still relies on charge currents to work. If a completely new low-power device is desired, which does not use charge currents at all in order to avoid resistive losses, the SHE is not a possible means for spin current generation. In order to avoid using such charge currents another method for pure spin current generation must be used.

2.3 Spin pumping

Spin pumping describes the transfer to angular momentum from a ferromagnet (FM) undergoing magnetic excitation to an adjacent nonmagnetic metal (NM) layer, as shown in Figure 2.4.^{9,10} Spin pumping has been extensively studied in a variety of FM metal/NM^{9,11-13} systems as well as FM insulator/NM systems.¹⁴⁻¹⁸ The study of spin pumping reveals important details about

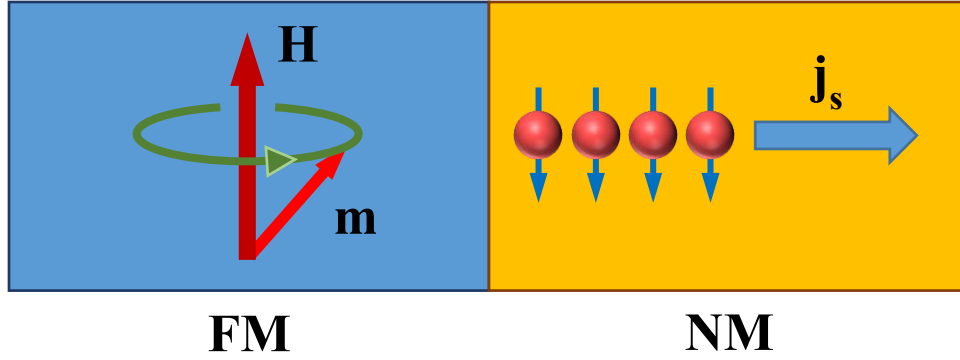


Figure 2.4 Spin pumping from a ferromagnet (FM) into a nonmagnetic metal (NM). Precession of the magnetization, \mathbf{m} , in the FM injects a pure spin current, \mathbf{j}_s , into an adjacent NM. The arrows in the NM represent the magnetic moments of the electrons.

the interface between the FM and the NM related to the transfer of angular momentum across the interface. Thus, is it of great importance to spintronic applications, which often make use of bilayer or multilayer films. Spin pumping is also an accessible method for generating pure spin currents by using microwaves as an excitation source.

Spin pumping transfers energy out of the magnetic material, which can be interpreted as a source of damping or loss, into the NM, as a pure spin current. The amount of spin current generated in the NM is proportional to the increase in damping in the FM. This is a manifestation of the conservation of angular momentum. This is commonly seen in multilayered structures. For additional information on FMR and loss see Chapter 6.

The spin current density generated by spin pumping can be described as

$$\mathbf{j}_s = \frac{\hbar}{4\pi} \text{Re}(g_{\uparrow\downarrow}) \hat{\mathbf{m}} \times \frac{\partial \hat{\mathbf{m}}}{\partial t} \quad 2.5$$

where $g_{\uparrow\downarrow}$ is the spin mixing conductance across the FM/NM interface and \mathbf{m} is the magnetization of the ferromagnet. This spin current density is equal to the net angular momentum transferred from the spins in the FM layer to the electrons in the NM layer through the interface per unit area

within a unit time. Note that the terms on the right side of Equation 2.5 has the same form as the damping term in Equation 6.11 and thus can be viewed as another source of damping, α_{SP} .

Spin pumping is an active area of spintronic research, both as a mechanism to generate pure spin currents and for its impact on magnetization precession and damping in bi-layered structures.^{19,20} Using microwaves to generate a spin current is desirable for certain device applications, however, in many practical applications microwaves are in undesirable means of manipulating currents. This is especially true in very small nano devices, where the length scales of microwave waveguides and other components limit the miniaturization of a device. While spin pumping is an active and exciting area of spintronics research, it will not be explored in detail in this work.

2.4 Spin Seebeck effect

The Seebeck effect is a thermoelectric effect which converts heat into electric potential at the junction of two different metals.²¹ In the same manner as the spin Hall effect is a spintronic version of the Hall effect, the spin Seebeck effect (SSE) is a spintronic version of the Seebeck effect. In the SSE a temperature gradient across a FM/NM interface generates a pure spin current which is injected into the NM, as shown in Figure 2.5.²²⁻²⁵ The SSE is one of the key phenomena that inspired the field of spin caloritronics, which examines charge and heat flow in spin-polarized materials.

The fundamental physics of the SSE can be understood as spin pumping caused by a difference in the magnon temperature between the FM and the electron, or phonon, temperature in the NM.^{23,26} The phonons, conduction electrons, and magnons in the FM and the conduction electrons and phonons in the NM can be considered as four separate subsystems, each with their

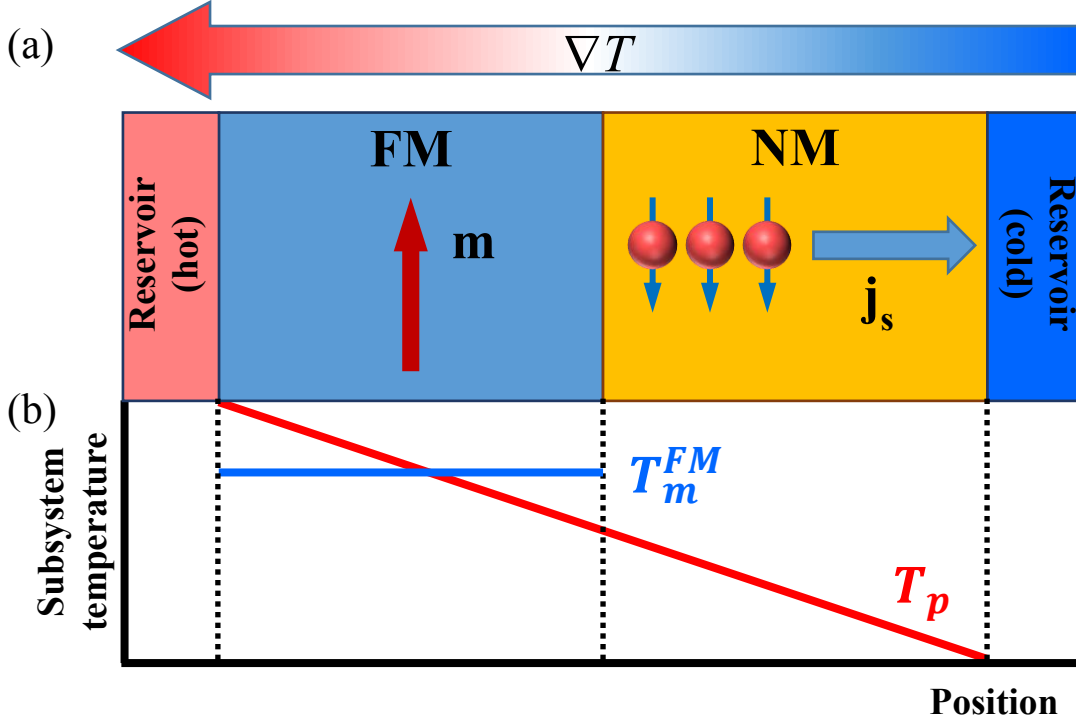


Figure 2.5 Schematic diagram of the spin Seebeck effect. The top diagram (a) shows a schematic of the experimental setup where a NM is in thermal contact with a low-temperature reservoir and a FM, with magnetization \mathbf{m} , is in thermal contact with a high-temperature reservoir creating a temperature gradient, ∇T , across the FM/NM interface, resulting in a spin current, \mathbf{j}_s , which is injected into the NM. The bottom diagram (b) shows a cartoon of the temperatures of the magnon subsystem, T_m^{FM} in blue, and the phonon subsystem, T_p in red, as a function of position within the bi-layered structure. The magnon subsystem is weakly coupled to the phonon subsystem in the FM, and its temperature is independent of the position. The phonon subsystem temperature changes gradually across the thickness of the sample. The difference in T_m^{FM} and T_p at the interface gives rise to the spin current in the NM.

own temperature: T_p^{FM} , T_e^{FM} , T_m^{FM} , T_e^{NM} , and T_p^{NM} , respectively. Note that when considering ferromagnetic insulators $T_e^{FM} = 0$.

Consider a temperature gradient applied across the film thickness with the NM in thermal contact with an ideal low-temperature reservoir, and the FM in thermal contact with an ideal high-temperature reservoir, as shown in Figure 2.5. Because the relaxation times in the spin, phonon, and electron subsystems are much shorter than the spin-lattice relaxation time each of these reservoirs becomes thermalized internally before they equilibrate with each other. Additionally,

the electron-phonon interaction is sufficiently strong such that $T_p^{FM} = T_e^{FM} \equiv T^{FM}$ and $T_p^{NM} = T_e^{NM} \equiv T^{NM}$. However, note that because the magnon-phonon interaction is relatively weak $T_m^{FM} \neq T^{FM}$. This is illustrated in the macrospin model, shown in Figure 2.5(b), where there is only one constant magnon temperature T_m^{FM} , and the electron and phonon temperatures, T_p , vary linearly across the thickness of the sample.

At finite temperature the magnetization order parameter in the FM is thermally activated, that is $\mathbf{m}(t) \neq 0$. At the FM/NM interface a spin current noise, \mathbf{I}_{sp} , is injected into the FM due to spin pumping according to

$$\mathbf{I}_{sp}(t) = \frac{\hbar}{4\pi} \left[g_{\uparrow\downarrow}^r \mathbf{m}(t) \times \frac{d\mathbf{m}(t)}{dt} + g_{\uparrow\downarrow}^i \frac{d\mathbf{m}(t)}{dt} \right] \quad 2.6$$

where $g_{\uparrow\downarrow}^{r,i}$ are the real and imaginary parts of the spin mixing conductance at the FM/NM interface. The thermally activated magnetization dynamics are determined by the magnon temperature, T_m^{FM} .

In addition to the spin current noise injected due to spin pumping, there is a fluctuating spin current, \mathbf{I}_{fl} , which is caused by thermal noise in the NM which can be described by a random magnetic field, $\mathbf{h}'(t)$, acting on the magnetization²⁷

$$\mathbf{I}_{fl} = -\mathbf{m}(t) \times \mathbf{h}'(t) \quad 2.7$$

This term is proportional to the temperature of the NM, T^{NM} .

At thermal equilibrium, we are interested in the DC component of the ensemble average of the spin current given by

$$\langle \mathbf{I}_S \rangle = \langle \mathbf{I}_{SP} \rangle + \langle \mathbf{I}_{fl} \rangle = S(T_m^{FM} - T^{NM}) \quad 2.8$$

where S is the spin Seebeck coefficient which is related to material parameters such as $4\pi M_S$ and $g_{\uparrow\downarrow}$.

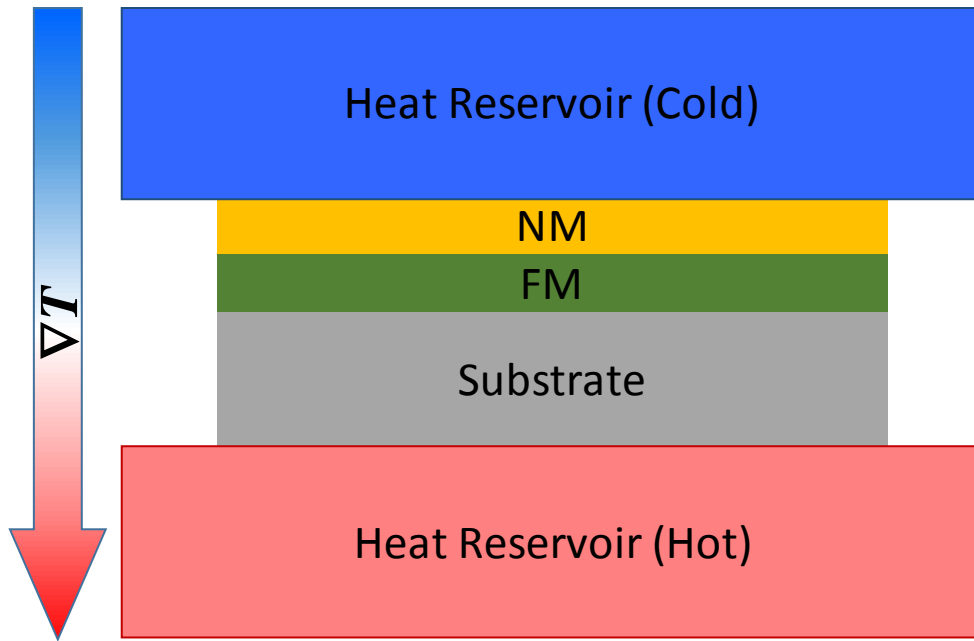


Figure 2.6 Longitudinal spin Seebeck effect experimental setup. A sample, consisting of a nonmagnetic metal (NM)/ferromagnet (FM) bilayer grown on a substrate, is placed between a hot reservoir and a cold heat sink such that a temperature gradient is created out of the film plane.

Thus, because of the temperature difference between the magnon and other subsystems at the FM/NM interface there will be a flow of angular momentum from the FM to the NM. This creates a spin current in the NM, which, via the ISHE, can be converted to a charge current and detected.

The most common configuration for SSE measurements is the so-called longitudinal configuration, shown in Figure 2.6.²⁸ A sample is placed between two heat sinks such that a temperature gradient is created out of the film plane. The experimental implementation of heat reservoirs varies widely across different experiments. Some common methods of creating the temperature gradient are using Peltier devices, resistive wire, Al block heat sinks, and laser heating.²⁹⁻³¹

One of the key advantages of this setup is that it avoids contamination due to other heating effects, such as the anomalous Nernst effect, which have the same magnetic field dependence as

the SSE.³²⁻³⁴ However, there are still experimental challenges when making SSE measurements in this configuration. For example, care must be taken during the measurement to ensure that the temperature gradient is entirely perpendicular to the film plane. Stray temperature gradients may contaminate measurements.³⁵

Additionally, it can be challenging to characterize the temperature gradients. One common method of measuring the temperature gradient is placing temperature sensors, such as thermocouples, above and below the sample. However, while the NM/FM structure is typically on the order of nm the substrates are on the order of μm or even mm. As discussed in the previous section it is the temperature gradient at the FM/NM interface which is responsible for the SSE. With such a temperature measurement configuration, it is difficult to determine the precise nature of the temperature gradient at the interface. It is possible to simulate or model the microscopic temperature gradient.³¹ While it is possible to compare measurements with the same sample or structure using such a measurement configuration, it is hard to compare different experiments which use very different methods for the generation of thermal gradient or temperature measurement.

2.5 Summary

The nature and origin of spin currents has been discussed. Three different methods for pure spin current generation have been described: the SHE, microwave spin pumping, and the SSE.

The SHE can convert a charge current into a transverse pure spin current, and the inverse SHE and does the opposite, converting a pure spin current into a transverse charge current. This technique is quite popular due to its simplicity and ease of implementation. It is also a powerful

tool for integrating the new field of spintronics into existing electronic devices. However, due to the use of charge currents its power saving advantages are fundamentally limited.

Microwave spin pumping uses excitations in a FM to transfer angular momentum into an adjacent NM. These excitations can be from ferromagnetic resonance, standing spin waves, or traveling spin waves. This technique is a very effective way to generate pure spin currents and does not involve the use of charge currents. However, microwave sources and their associated waveguides are not practical for all devices.

The SSE generates a pure spin current when a temperature gradient exists across a FM/NM interface. This method makes it possible to utilize what is normally waste heat to generate pure spin currents, thus turning an otherwise wasted resource into an efficient means of generating pure spin currents. However, it is not always easy to precisely characterize or control temperature gradients, which represents an engineering challenge for device implementation.

Spin currents represent a large potential advancement in modern technology. The ability to drastically reduce the power consumption of electronic devices would be a great improvement. However, due to the physically different means by which spintronic devices operate, much work still remains to fundamentally understand the physics of spin currents, as well as achieve practical methods for efficiently generating and detecting spin currents. It is because of these potential benefits, and challenges, that spintronics is such an active and exciting area of research.

CHAPTER 3 Spin Seebeck effect in magnetic insulators

3.1 Overview

Pure spin currents are very promising for information transfer and processing for future low power electronics. By using the spin Seebeck effect (SSE) a temperature gradient across a ferromagnetic (FM) thin film will produce a spin current into an adjacent normal metal (NM).^{22,25,28,36-42} One important feature of the SSE is that it not only occurs in magnetic metals^{22,36,42} and semiconductors,^{37,38,41} but also takes place in magnetic insulators,^{25,28,39,40} which significantly expands the landscape of suitable materials for generation of pure spin currents.

When using magnetic insulators in bi-layered structures for generating pure spin currents there are several advantages when compared to using magnetic metals. First, there is no possibility of current shunting through the ferromagnetic insulator. This increases the signal-to-noise ratio of such experiments. In SSE experiments, it is also possible to avoid other unwanted thermal effects, such as the anomalous Nernst effect.³³ Magnetic insulators also have lower damping than transition metals^{43,44} which are typically used in spin current devices. Due to the lower damping of these materials the loss of spin currents to magnetic relaxation is lower, thus devices utilizing magnetic insulators have a higher spin current generation efficiency.

This chapter reports on the generation of pure spin currents via the light-induced SSE in magnetic insulator thin films.⁴⁵ YIG or BaM thin-film samples were placed on an aluminum heat sink and exposed to light from a 100W incandescent bulb. The light produced a thermal gradient

across the sample thickness which produced, through the SSE, a pure spin current flowing into a neighboring Pt thin film. Via the inverse spin Hall effect (ISHE), the spin current generated an electric voltage across the Pt layer along the direction perpendicular to the magnetization in the sample. The voltage varied with time in the same manner as the temperature gradient. The voltage amplitude showed a linear dependence on the temperature gradient, and the sign of the voltage flips when the magnetization direction in the sample is reversed.

While previous work has shown the SSE in “soft” magnetic materials,^{25,28,39,40} this work is the first demonstration of the SSE in “hard” hexagonal ferrites. As such, the spin current generation approach presented here has a significant implication for future spin battery devices. Specifically, the use of a self-biased film allows for the development of miniature devices without the need for an external magnetic field.

The novel use of light as a heat source, demonstrated in this work, allows for rapid generation of spin currents. This experimental configuration also has potential applications harvesting solar energy, because the generation of electric voltage requires light only. To realize efficient sunlight-to-electricity conversion, one could replace the Pt layer with materials with much stronger spin-orbit coupling, such as topological insulators.

In this work two different magnetic insulators are used: yttrium iron garnet and barium hexagonal ferrite. The properties of these two important insulators are discussed below.

3.1.1 Yttrium iron garnets

One of the most common magnetic insulators used in all areas of magnetics research is yttrium iron garnet ($\text{Y}_3\text{Fe}_5\text{O}_{12}$, YIG). YIG is a ferrimagnetic oxide material with cubic symmetry, definite composition, and extremely low magnetic damping.⁴⁶⁻⁴⁸

YIG, and doped YIG, have the lowest relaxation rate of any magnetic material, with an intrinsic Gilbert damping constant, α , as low as 3×10^{-5} for bulk materials⁴⁹ and 8×10^{-5} for thin films,⁴⁴ which is about one order of magnitude smaller than other ferrites⁵⁰ and two orders of magnitude smaller than in transition metals^{43,50} which are commonly used in spintronic devices. This low damping is primarily due to the lack of conduction electrons or Fe^{2+} ions.⁵¹

The combination of its regular structure, insulating property, and record low damping make YIG ideal for experiments involving any kind of magnetization dynamics such as microwave devices, spin waves, ferromagnetic resonance, magneto-optical effects, and studies of pure spin currents, including the SSE.¹⁹ From a practical standpoint YIG is so desirable because, due to its low damping and insulating property, YIG based spintronic devices require significantly lower power compared to metal based devices. YIG based devices also circumvent any issues related to charge currents.

Due to its ubiquity in the field of magnetics YIG has been referred to as the “fruit fly of magnetism” by Dr. Charles Kittel.⁵²

3.1.2 Barium hexagonal ferrites

M-type barium hexagonal ferrite ($\text{BaFe}_{12}\text{O}_{19}$, BaM) is another common magnetic insulator used in spintronics. It is a good candidate material for spintronic devices due to its relatively low damping and strong uniaxial magnetic anisotropy.

Because of its strong internal field, BaM has a large remnant magnetization and the BaM film can remain self-biased in the absence of an external magnetic field. The remanence in BaM can be as large as 97% of the saturation magnetization⁴⁷ and thus BaM is classified as a “hard” ferromagnet. Devices using such “hard” ferromagnets can be much smaller and more energy efficient because they do not require any external magnetic fields to operate.

3.2 Experimental setup

The YIG sample used for SSE measurement is a bilayer of YIG (5.9 μm)/Pt (3.8 nm) grown on a 0.5-mm-thick (111) single crystal gadolinium gallium garnet ($\text{Gd}_3\text{Ga}_5\text{O}_{12}$, GGG) substrate. The sample is 22.9 mm long and 1.7 mm wide. From FMR measurements, the $4\pi M_s$ of the sample is 1.89 kG and the Gilbert damping constant α is 1.8×10^{-4} .

The BaM sample used in this work is a BaM (1.2 μm)/Pt (2.5 nm) bilayer grown on a 0.5-mm-thick a-plane sapphire substrate. The sample size is 5.0 mm by 1.0 mm. Vibrating sample magnetometer measurements indicate the $4\pi M_s$ of the film is 3.87 kG and there exists strong in-plane uniaxial anisotropy along the c axis with an anisotropy field H_a of about 16.5 kOe. The remnant magnetization of this film is about 89% along the c axis. This means the film is self-biased to a large degree at zero fields, which allows for spin-current generation in the absence of external magnetic fields.

Figure 3.1 shows a schematic diagram of the experimental setup. The sample, YIG or BaM, sits on an aluminum plate, which works as a heat sink, and is exposed to light from an incandescent bulb, which is placed directly above the sample. The light, together with the aluminum plate, produces a temperature gradient across the thickness of the sample. Via the SSE, the temperature gradient in the magnetic insulator then produces a pure spin current that flows into the Pt layer.²³ The spin current in turn generates an electric voltage across the length direction (the x axis) of the Pt layer via the ISHE.⁵³⁻⁵⁵

In this work, the experiments used a 100 W incandescent bulb placed 3-26 cm above the sample. A Keithley nanovoltmeter was used to measure the voltage (V) across the length direction of the Pt strip. Two type-T thermocouples were attached to the top and bottom surfaces of the

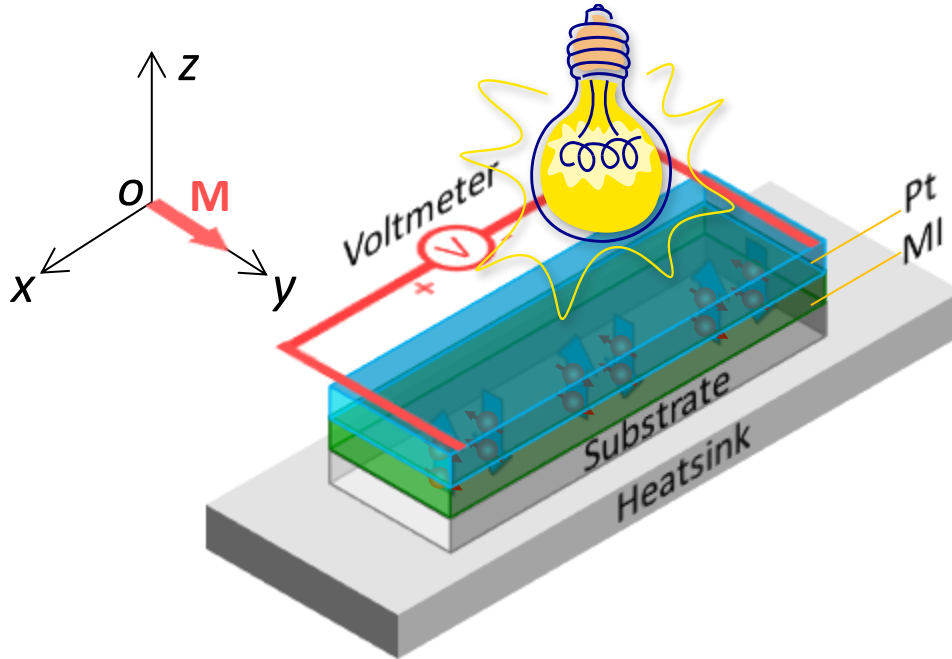


Figure 3.1 Schematic diagram of the SSE experimental setup. A Pt / magnetic insulator (MI) structure is placed on an Al heat sink. The sample is magnetized in the \hat{y} direction and illuminated from above by an incandescent light bulb. This generates a temperature gradient and pure spin current in the \hat{z} direction. The spin current flows into the Pt and, via the ISHE, is converted to a charge current in the \hat{x} direction which is measured by a nanovoltmeter.

sample structure to measure the temperature difference across the structure thickness ($\Delta T = T_{\text{top}} - T_{\text{bottom}}$).

For the YIG sample an external bias field of 1.08 kOe was applied in the sample plane by a pair of permeant magnets. For the BaM sample all measurements were taken in the absence of external magnetic fields. Prior to the measurements, however, an external field of 10 kOe was applied along the \hat{y} direction (or the $-\hat{y}$ direction) to set the magnetization (\mathbf{M}) of the BaM film in the \hat{y} direction (or the $-\hat{y}$ direction). Note the c axis of the BaM film is also along the y axis. This means that the magnetization \mathbf{M} is along the easy axis during the measurements.

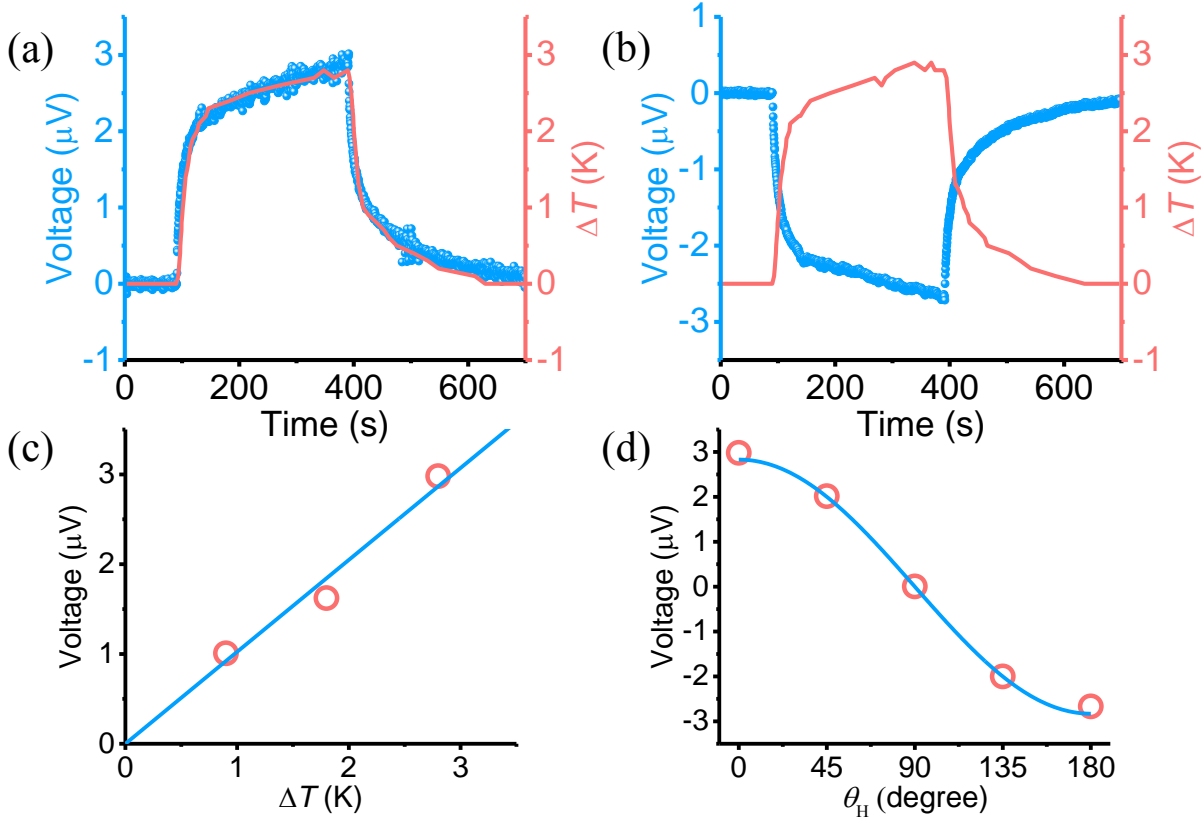


Figure 3.2 Light-induced generation of pure spin currents in YIG/Pt. (a) and (b) show the voltage and temperature difference (ΔT) between the top (Pt) and bottom (GGG) surfaces of the sample, respectively, in response to a light that was turned on at 100s and off at 400s. In (a) and (b) the magnetic field is oriented such that $\mathbf{H} \parallel \hat{y}$ and $\mathbf{H} \parallel -\hat{y}$, respectively. (c) gives the voltage amplitude as a function of ΔT . (d) gives the voltage amplitude as a function of the in-plane field angle θ_H .

3.3 Results and discussions

Figure 3.2 presents the light-induced generation of pure spin currents in the YIG/Pt sample. Figure 3.2(a) and (b) show the $V(t)$ and $\Delta T(t)$ signals, respectively, in response to light that was turned on at time $t=100\text{s}$ and then turned off at $t=400\text{s}$. The data shown in (a) and (b) were measured for $\mathbf{H} \parallel \hat{y}$ and $\mathbf{H} \parallel -\hat{y}$, respectively. Figure 3.2(c) shows the V vs. ΔT response. The circles show the V data, averaged from 380-395s, and the blue line is a linear fit to the data. Different ΔT

values were realized by changing the height of the bulb relative to the sample. Figure 3.2(d) shows the V as a function of the in-plane field angle θ_H , where $\theta_H = 0$ represents $\mathbf{H} \parallel \hat{\mathbf{y}}$. The circles represent the V and ΔT data, averaged from 380-395s, and the blue curve is a sine function fit to the data.

The data in Figure 3.2 indicate three key results. First, the voltage signal varies with the time in the exact same manner as ΔT , as shown in (a) and (b). Second, the voltage vs. ΔT response shows a linear response, as shown in (c). Third, the voltage response varies sinusoidally with θ_H . These results are consistent with the expectation that the strength of the SSE-produced spin current is proportional to $T_{\text{Pt}} - T_{\text{m}}$, where T_{Pt} and T_{m} denote the phonon (or electron) temperature in the Pt layer and the magnon temperature in the YIG film, respectively.^{23,56} Note that roughly $T_{\text{Pt}} - T_{\text{m}}$ changes linearly with ΔT . The data also show that the sign of the voltage varies sinusoidally with θ_H and the sign of the voltage flips when \mathbf{H} , and therefore the \mathbf{M} in YIG, reverses. This agrees with the fact that for a given temperature gradient, the polarization of the SSE-produced spin current is determined by the direction of \mathbf{M} in the magnetic film.^{39,40} These results clearly demonstrate the light-induced generation of pure spin currents.

Additional measurements done using the BaM film and no external magnetic field are summarized in Figure 3.3. Graphs (a) and (b) in Figure 3.3 present the $\Delta T(t)$ and $V(t)$ signals in response to light that was turned on at the time $t=100$ s and was then turned off at $t=200$ s. The data shown in (a) and (b) were measured for $\mathbf{M} \parallel \hat{\mathbf{y}}$ and $\mathbf{M} \parallel -\hat{\mathbf{y}}$, respectively. Graph (c) shows the V vs. ΔT responses. The empty circles show the data for $\mathbf{M} \parallel \hat{\mathbf{y}}$, while the solid circles show those for $\mathbf{M} \parallel -\hat{\mathbf{y}}$. For each data point in graph (c), the V and ΔT values are averages of V and ΔT in the 120-200s time window, and different ΔT values were realized by changing the height of the bulb relative to the Pt/BaM sample. Figure 3.3(d) shows data obtained when using both a light bulb,

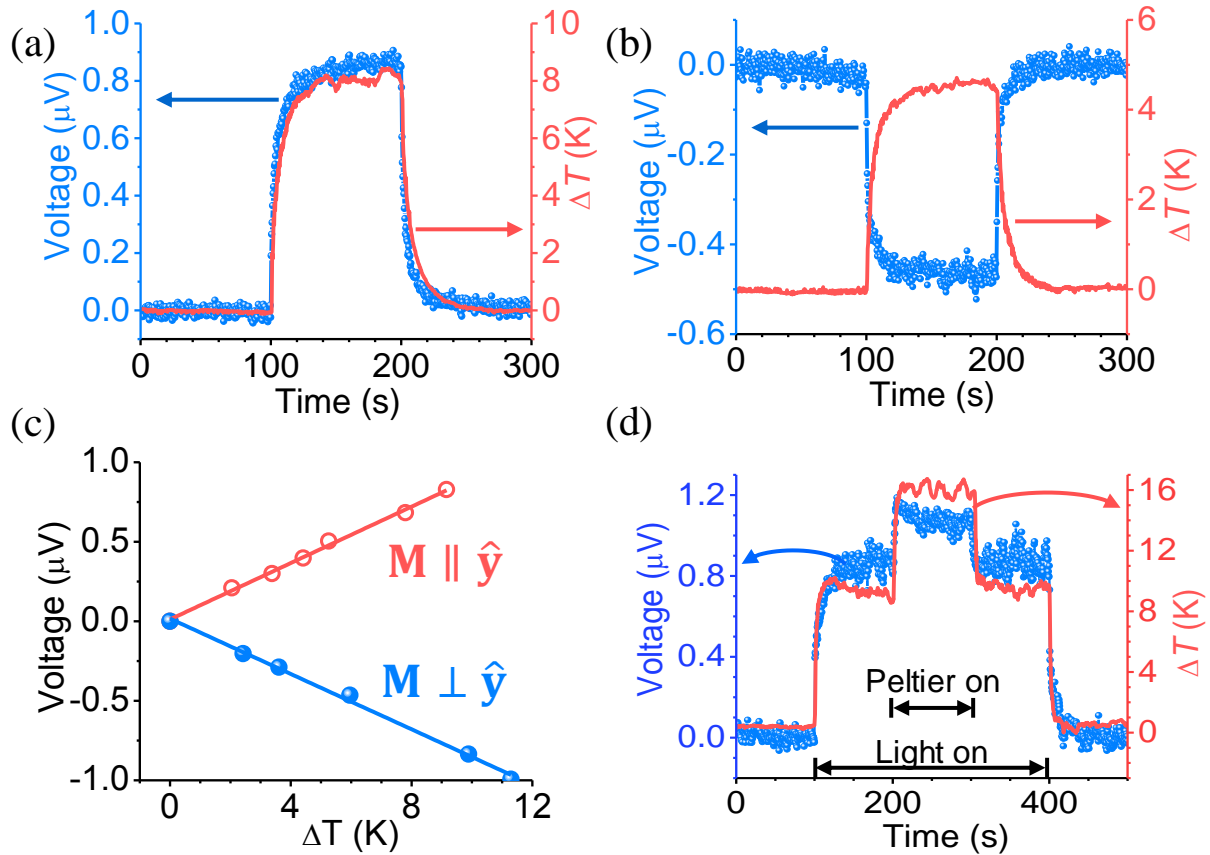


Figure 3.3 Light-induced generation of pure spin currents in BaM/Pt. (a) and (b) show the voltage and temperature difference between the top (Pt) and bottom (sapphire) of the film (ΔT) in response to a light that was turned on at 100s and off at 200s. In (a) and (b) the magnetic field is oriented such that $\mathbf{M} \parallel \hat{y}$ and $\mathbf{M} \perp \hat{y}$, respectively. (c) gives the voltage amplitude as a function of ΔT . (d) Voltage and ΔT signals obtained when both a light bulb and a Peltier cooler were used to control the temperature gradient.

which was turned on at 100 s and off at 400 s, and Peltier cooler, which placed under the Al block and was turned on at 200 s and off at 300 s, to control the temperature gradient

These results confirm the outcomes of the experiments using the YIG film. Figure 3.3 indicates that (1) the voltage signal varies with time in the exact same manner as ΔT , as shown in graph (a) and (b), and (2) the voltage vs. ΔT response show almost linear behavior, as shown in graph (c). These results are consistent with the results of measurements on YIG, the magnitude of the voltage signal is proportional to the temperature gradient and the sign of the voltage signal reverses when the direction of \mathbf{M} is reversed. Furthermore, the measurement using the Peltier

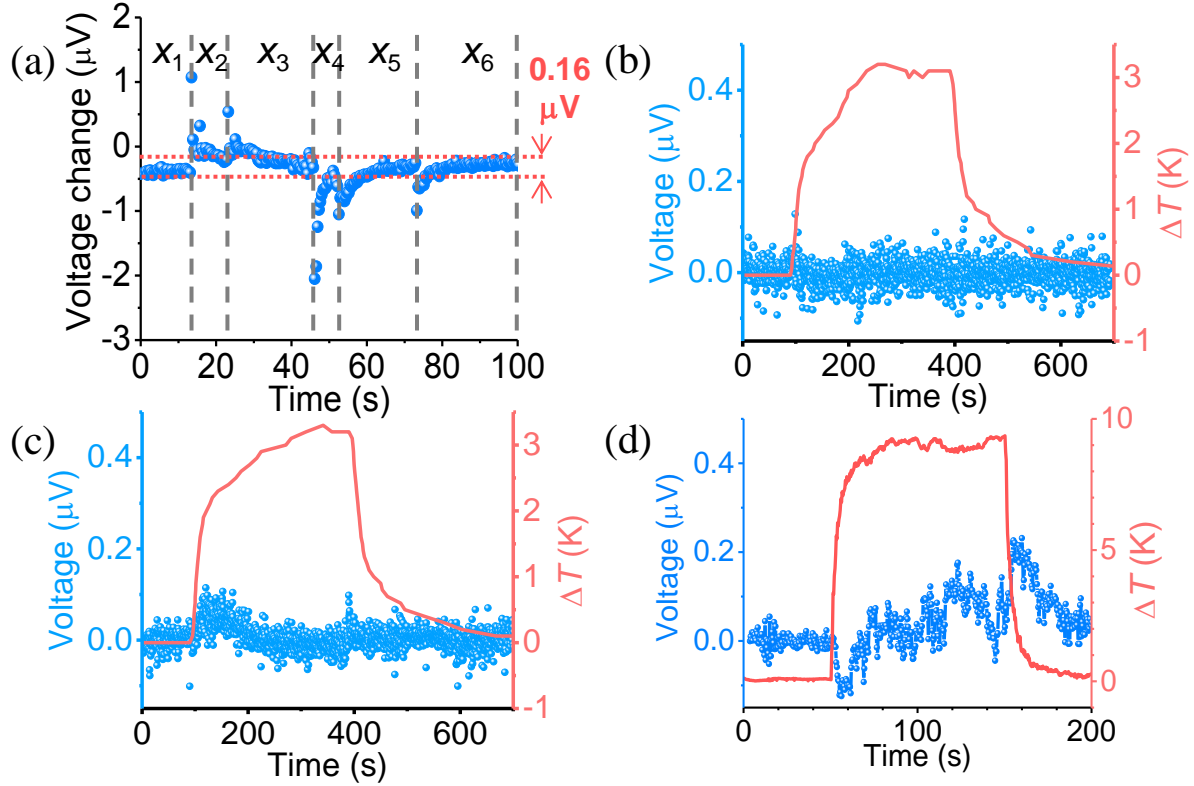


Figure 3.4 Control measurements. (a) Voltage changes caused by moving the bulb along the x -axis obtained with same sample used in Figure 3.3. Voltage and ΔT signals obtained with (b) a Pt(3.8 nm)/GGG(0.5 mm) sample with no magnetic film, (c) a Cu(16.8 nm)/YIG(5.9 μm)/GGG(0.5 mm) sample and (d) a Cu(9 nm)/BaM(1.2 μm)/sapphire(0.5 mm) sample.

cooler shows that the light performs a similar function as the heating/cooling device in previous SSE studies.^{22,28,36-40} It is evident that the voltage changed in almost the same manner as ΔT , independent of the approaches to realize ΔT . Finally, these measurements required no external magnetic field, demonstrating the light-induced generation of pure spin currents in a self-biased film.

Additional control measurements, shown in Figure 3.4, further support the conclusions from the YIG and BaM films. The voltage amplitude is sensitive to the bulb height, as demonstrated above, but it is not sensitive to the horizontal position of the bulb, as shown in Figure 3.4(a), where the data give the change of the voltage relative to its initial value in response to

moving the bulb to different positions (x_1, x_2, \dots, x_6) along the x axis. One can see that, except for the odd points due to the electric disturbance caused by position change, the voltage change is very small ($<0.16 \mu\text{V}$), indicating that the voltage signals in Figure 3.2 and Figure 3.3 were not due to the conventional Seebeck effect.⁵⁷

Second, if the magnetic film is removed there is no signal observed. The SSE is a magnetic effect which requires a magnetic material to manifest. Figure 3.4(b) shows the V and ΔT measurements of a Pt(3.8 nm)/GGG(0.5 mm) sample, which has no magnetic material. One can see that there is no measurable voltage response, despite a large temperature gradient. This measurement shows the absence of any SSE and confirms the magnetic nature of the previous measurements.

Finally, Figure 3.4(c) and (d) are a control measurements performed on Cu(16.8 nm)/YIG(5.9 μm)/GGG(0.5 mm) and Cu(9 nm)/BaM (1.2 μm)/sapphire(0.5 mm) samples, respectively. No signal was observed in this sample because the ISHE in Cu is very weak and cannot convert spin currents in the Cu thickness direction to measurable electric voltage signals across the Cu length. This control measurement shows the voltage is very weak and varies with time in a completely different manner than ΔT , indicating the absence of the SSE effect. Most likely, the V signal resulted from the conventional Seebeck effect which is associated with the temperature gradient along the sample length direction.⁵⁷

3.4 Summary

This work establishes a novel approach for the generation of pure spin currents, utilizing light to generate the SSE. The experiments used a μm -thick YIG or BaM thin film which was

capped by a nm-thick Pt layer. The BaM film has strong in-plane uniaxial anisotropy and is therefore self-biased.

Upon exposure to light, a temperature difference is established across the magnetic film thickness that gives rise to a pure spin current in the Pt via the SSE. Through the ISHE, the spin current produces an electric voltage across one of the Pt lateral dimensions which is perpendicular to \mathbf{M} in the magnetic insulator. The voltage varies with time in the same manner as ΔT and varies sinusoidally when \mathbf{M} is rotated in the film plane. This work demonstrates a spin battery that, when using BaM as the MI, requires neither a magnetic field, a microwave source, nor a heating/cooling device, but only light.

CHAPTER 4 Photo-spin-voltaic effect in Pt/magnetic insulator heterostructures

4.1 Overview

The generation of pure spin currents in a rapid and controllable manner represents a challenging research subject. At the present time, pure spin currents, with no associated charge current, can be generated by means of spin pumping and the spin Seebeck effect (SSE). Spin pumping involves the use of microwaves to drive the precession of magnetic moments in a ferromagnet and the transfer of spins from precessional moments to an adjacent normal metal.^{9,58,59} For the SSE, a temperature gradient across a ferromagnetic film induces a spin voltage in the film which can inject a spin current into an adjacent normal metal.^{22,24,25,36-39} Although spin pumping and the SSE offer two means for spin current generation, it is challenging to realize well-localized microwave fields or temperature gradients at nanometer scales in a rapid fashion. An alternative way to produce spin currents is to use the spin Hall effect, in which spin-orbit coupling converts a longitudinal charge current to a transverse spin current.^{5,6,8,60} This approach, however, requires charge currents, and hence involves unwanted power consumption.

This work reports on the discovery of a photo-spin-voltaic (PSV) effect that offers a new means for the generation of pure spin currents.⁶¹ A schematic of the effect is shown in Figure 4.1.

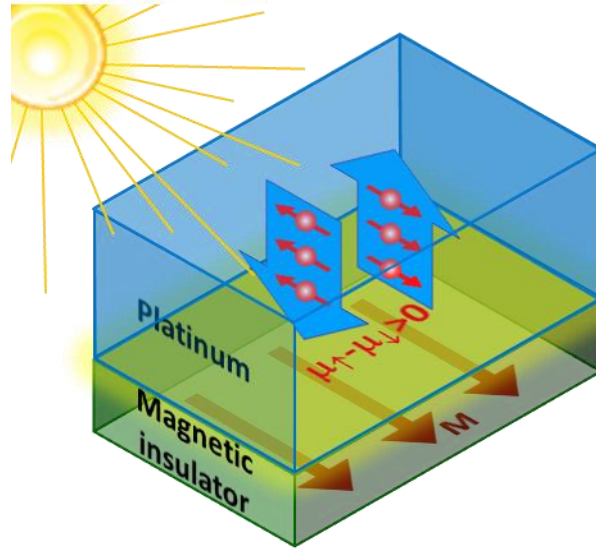


Figure 4.1 Photo-spin-voltaic effect in a Pt/MI bi-layered structure. The MI has in-plane magnetization, \mathbf{M} . When the structure is exposed to light, a spin voltage ($\mu_{\uparrow} - \mu_{\downarrow}$) arises in Pt atomic layers in close proximity to the MI. This spin voltage drives spin-up and spin-down electrons to move in opposite directions, resulting in a pure spin current across the Pt thickness.

The experiments used normal metal/magnetic insulator (MI) heterostructures where the normal metal was a Pt layer, several nanometers in thickness, and the MI was a film of YIG, Ga-doped YIG, or BaM with a thickness in the 10-10⁵ nm range. When light illuminates the Pt film, photons with appropriate energy excite electrons in the occupied bands to the unoccupied bands. For the Pt atomic layers in close proximity to the MI, the efficiency of the photon-driven electron excitation is different for electrons in different spin channels. This efficiency difference, together with the difference in the diffusion of the excited electrons and holes, gives rise to a spin voltage near the interface, and a corresponding pure spin current cross the Pt thickness. Such spin currents can produce a measurable electric voltage in the Pt film by means of the inverse spin Hall effect (ISHE).^{6,54} This new phenomenon is analogous to the photo-voltaic effect in semiconductors,⁶² but engages spin-dependent photon-driven electron excitation.

4.2 Experimental setup

Figure 4.2(a) shows a schematic of the experimental setup, where the core component is a Pt/MI/substrate structure. An in-plane magnetic field H is applied to magnetize the MI film to saturation. A halogen light bulb was used to illuminate the Pt/MI structure from either the top (as shown) or the bottom. A nanovoltmeter was used to measure the ISHE voltages across the Pt length.

The MIs used in this work are 4.9- μm -thick YIG, 10.4- μm -YIG, 21-nm-thick YIG, 78- μm -thick Ga-doped YIG, and 1.2- μm -thick BaM. The substrates for the YIG and Ga-doped YIG film samples were single-crystal (111)-oriented GGG. The 4.9- μm -thick YIG, 10.4- μm -YIG, and 78- μm -thick doped YIG (doped with 2.5% atomic Ga) films were grown by liquid phase epitaxy.⁶³ The 21-nm-thick YIG films were grown by RF sputtering.^{44,64} The 1.2- μm -thick BaM films were grown on single crystal c -axis in-plane sapphire substrates by pulsed laser deposition.⁴⁵ The Pt and Cu layers were grown by DC sputtering at room temperature. The YIG, doped YIG, and BaM films were characterized by field-in-plane ferromagnetic resonance (FMR) measurements. Fitting of the FMR frequency vs. field responses with the Kittel equation yielded an effective saturation magnetization ($4\pi M_s$) of 1920 G for the 4.9- μm -thick YIG films, 1757 G for the 21-nm-thick YIG films, 950 G for the 78- μm -thick doped YIG films, and 3870 G for the 1.2- μm -thick BaM films. Static magnetic measurements indicated that the BaM films had an effective uniaxial anisotropy field of 16.5 kOe and a remnant magnetization of 3440 G, both along the in-plane c axis.

For the PSV measurements, the magnetic field was provided by a pair of permanent magnetics, and was measured with by a LakeShore model 450 gaussmeter. The electrical voltages were measured by Cu wires attached to the sample with silver paste and connected to a Keithly

2182A nanovoltmeter. The temperatures were measured by National Instruments USB-TC01 thermometers with Omega 5SC-TT-T-40-36 Type-T thermocouples. In order to maximize the signal-to-noise ratio, the experimental setup was placed on an optical table to minimize mechanical vibrations and was covered with an enclosure to diminish air flows. To minimize the temperature gradients across the sample thickness and length, an 8 cm fan was used to circulate air within the sample enclosure. The primary light source was a 100W 120VAC halogen light bulb.

The optical spectra of different light sources were measured with an Ocean Optics IRRAD200 visible spectrometer, with a wavelength range of 350-1000 nm, and an Ocean Optics NIRQuest512-2.5 near-infrared (NIR) spectrometer, with a wavelength range of 950-2500 nm). The light was collected using an Ocean Optics QP600-2-VIS-NIR patch cord with a 600 μm fiber optic core and an Ocean Optics P450-1-FLUORIDE patch cord with a 450 μm core for visible and NIR measurements, respectively. The optical transmission properties of the samples and the optical filters were measured with the same spectrometers and patch cords by placing the sample or filter over the end of the patch cord, between the fiber and the light source.

4.3 Demonstration of the photo-spin-voltaic effect

Figure 4.2(b) shows the voltage signals measured in response to light illuminating the Pt side of the structure. The three signals are for different field angles (θ_H , as marked in Figure 4.2(a)). Figure 4.2(c) compares the responses to light incident on different sides of the sample. One can see three main results from the data in Figure 4.2(b) and (c). First, the light illumination gives rise to a notable voltage signal, demonstrating the PSV effect. Second, the voltage versus θ_H response can be fitted well by a sine curve, with the voltage flipping its sign when H is reversed, showing the magnetic nature of the PSV effect. Third, reversal of the direction of light illumination does

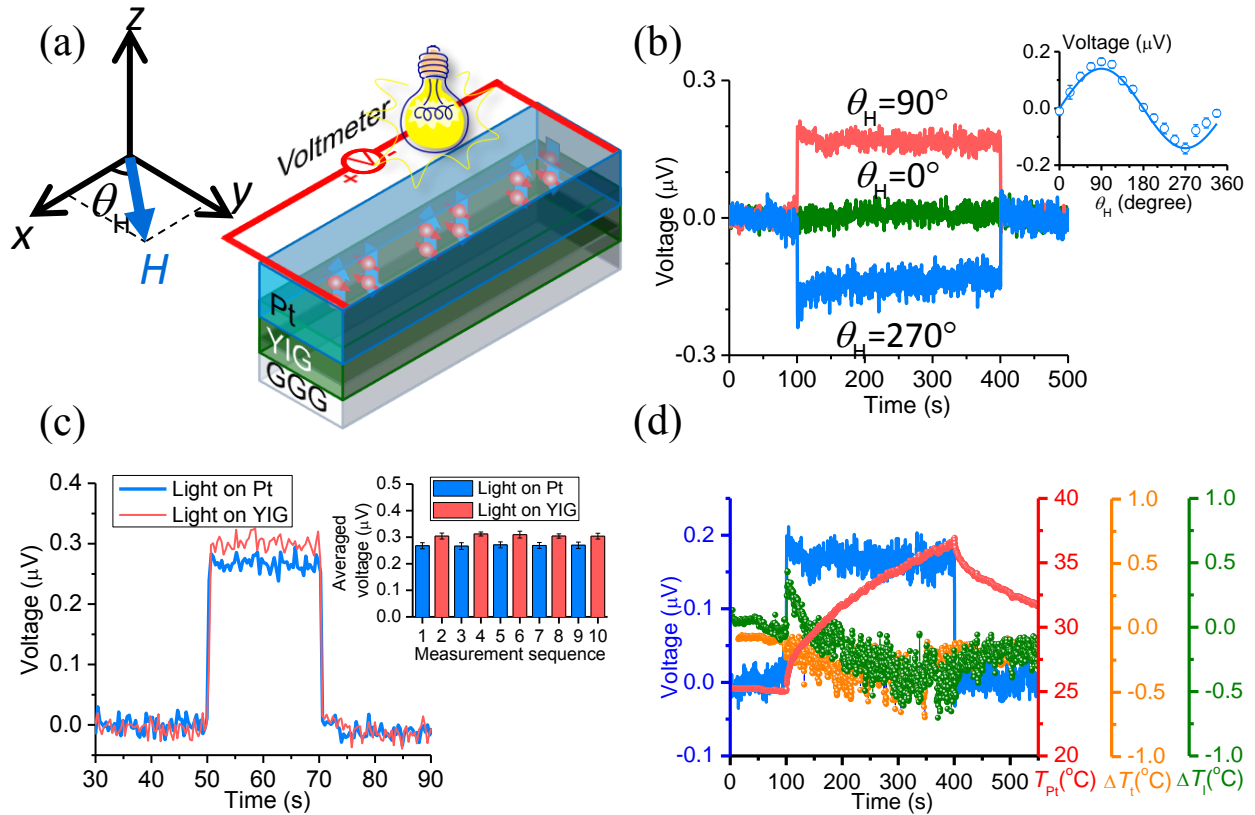


Figure 4.2 Main features of the PSV effect. (a) Experimental configuration to demonstrate the PSV effect. (b) Voltage signals measured for different field angles (θ_H) in response to light that was first turned on at 100 s and then turned off at 400 s. The inset shows the voltage as a function of θ_H . The circles show the voltage average over the entire period of light illumination; the error bars represent the standard deviation; the curve shows a sine function fit. (c) Voltage signals for different directions of light illumination in response to a light signal turned on at 50 s and off at 70 s. The inset shows the voltage values for ten measurements, which are averages over the time period 55–65 s; error bars are the standard deviation. (d) Voltage and temperature profiles obtained under the same condition as the data shown by the red curve in (b). All the data were obtained with a 3.5-mm-long, 1.5-mm-wide Pt(2.5 nm)/YIG(4.9 μm)/GGG(0.5 mm) sample, a magnetic field of $H=1090$ Oe, and a 100 W halogen light bulb placed 29 cm away from the sample. The data in (b) and (d) were measured with an electrode separation of 2.5 mm, whereas the data in (c) were measured with a separation of 3.0 mm. For the data in (c) and (d), the field angle θ_H is 90° .

not result in a change in the sign of the voltage, indicating that the PSV effect is unrelated to possible temperature gradients across the structure thickness.

Figure 4.2(d) presents measurements of the voltage and three temperatures, which further confirm the irrelevance of the temperature gradient. The blue curve shows the voltage. The red,

orange, and green symbols show the temperature of the Pt surface (T_{Pt}), the temperature difference across the entire structure thickness (ΔT_t), and the temperature difference along the x axis between the two electrodes for the voltage measurements (ΔT_l), respectively. It is obvious that the temperatures respond to the ‘on’ and ‘off’ operation of the light in a manner much slower than that of the voltage. ΔT_l even changes its sign during the period of light illumination. Furthermore, ΔT_t and ΔT_l are both very small, with their absolute values less than 0.5°C . If one takes into account the GG substrate thickness and assumes a linear temperature distribution across the structure thickness, the temperature difference across the YIG film thickness would be less than 0.005°C . These results together clearly confirm that the observed voltage signals cannot be attributed to any effects associated with a temperature gradient, including the Seebeck effect,^{21,57} the SSE,^{22,24,25,36-39} the Nernst effect,³² the anomalous Nernst effect,^{33,65} and the planar Nernst effect.^{33-35,66} Note that when ΔT_t (ΔT_l) is large and the SSE overwhelms the PSV effect, the voltage signal changes with time in exactly the same manner as ΔT_t (ΔT_l), as shown in Figure 4.9.

The above-described PSV effect was further examined through additional measurements which varied the illumination direction and utilized different MI films.

4.3.1 Different illumination configurations

Figure 4.3 shows data obtained with different light/field configurations using four different samples. Figure 4.3(a) shows the data for the same samples as described in Figure 4.2. The data were obtained for three different light configurations and two different magnetization (\mathbf{M}) orientations. The numbers beside the voltage profiles indicates the voltage levels. Three important results are evident from Figure 4.3(a). First, for a given \mathbf{M} orientation, the voltage signal is the strongest when the two bulbs are used to illuminate both the sides of the sample; and there is no change in the voltage sign when one switches between the light-on-Pt and light-on-MI

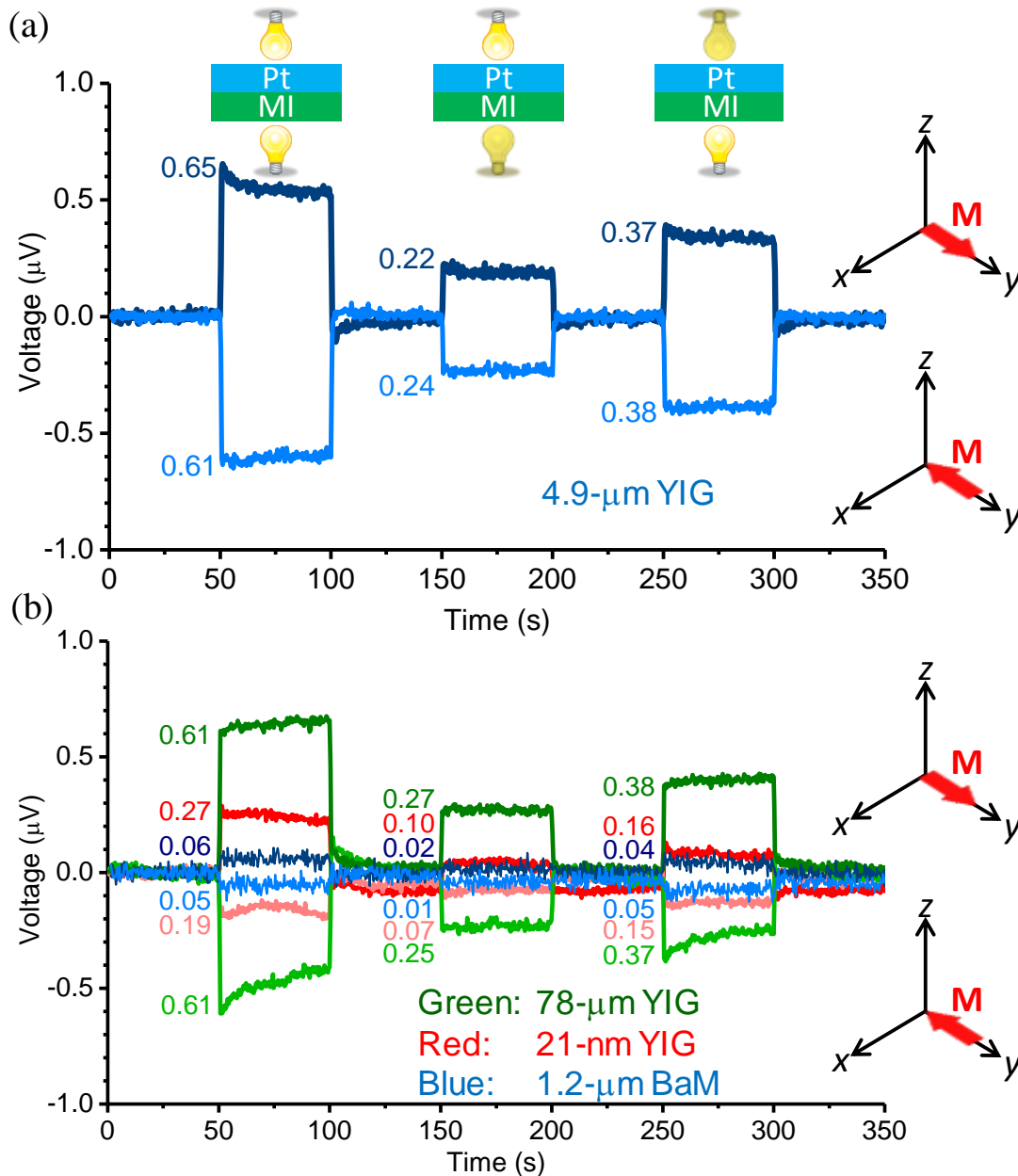


Figure 4.3 Measurements for different illumination/magnetization configurations. The data show PSV voltages in response to three different light illumination configurations (see small diagrams on the top) for two different magnetization (\mathbf{M}) orientations (see diagrams on the right) for four different samples. (a) Results for the same sample as that described in Figure 4.2. (b) Results for three further samples: 78 μm Ga-doped YIG, 21 nm YIG, and 1.2 μm BaM. All the data were obtained with 100 W halogen light bulbs. The light-to-sample distances were 20 cm, and the electrode separation was about 3.8 mm.

configurations. These results further verify that the observed effect is not due to any effects associated with a temperature gradient. If the effect is associated with temperature gradients, one

would expect that, for the three light configurations in Figure 4.3(a), the leftmost one should have the smallest temperature gradient across the MI thickness, and should therefore yield the weakest voltage signal. Second, the data also show that the voltage obtained with two bulbs illuminating both sample sides is approximately equal to the sum of the voltages for the light-on-Pt and light-on-MI configurations. This result indicates that it is the light intensity, not the illumination direction which is important for the PSV effect. Third, reversing \mathbf{M} results in a flip in the sign of the voltage, but produces only trivial changes in the voltages magnitude, confirming the magnetic nature of the PSV effect shown in Figure 4.3(a).

4.3.2 Different magnetic insulator films

Figure 4.3(b) presents the data measured with three different samples, where the MI layers are a 78- μm -thick opaque Ga-doped YIG film, a 21-nm-thick transparent YIG film, and a 1.2- μm -thick brown-color BaM film. The data are presented in the same format as in Figure 4.3(a). One can see that the data in Figure 4.3(b) evidently confirm all the results shown in Figure 4.3(a). Moreover, they also suggest it is most likely that visible light does not play a dominant role in the PSV effect. If visible light were to be involved then one would expect that the samples consisting of non-transparent MI films should yield much weaker signals for the light-on-MI configuration than for the light-on-Pt configuration.

The data in Figure 4.3 indicate a very important result: in spite of very different magnetic films, the four samples yielded voltage signals that differ by no more than one order of magnitude. This result has two implications: the signals are not due to the SSE, which depends strongly on the MI thickness;⁶⁷ and the effect is not associated with magnon excitations in the MI, but is probably related to excitations in the Pt. If the MI is responsible for the PSV effect, one would expect that the voltage levels of the signals from the three YIG samples should be significantly different. In

addition, the data also indicate that, independent of the thickness and transparency of the MI, the light-on-MI configuration gives stronger signals than the light-on-Pt configuration, consistent with the data shown in Figure 4.2(c).

4.4 Wavelength dependence of the photo-spin-voltaic effect

The above results indicate that it is very likely that the PSV effect relies on excitation in the Pt and visible light is not the dominant contributor to the voltage signal. These indications were further clarified by measurements using different light sources and optical filters. Figure 4.4 shows representative data. Figure 4.4(a) presents the optical transmission values of four samples grown on GGG substrates, as well as the transmission of a bare GGG substrate. Although not shown, the transmission values in each case remained the same when the samples were flipped over. In comparison with the bare GGG, the two YIG samples show much lower transmission values in the 350-450 nm range. This is consistent with the fact that YIG films have a bandgap of about 2.8 eV.⁶⁸ The comparison between the data of the YIG and Pt/YIG samples clearly shows that the growth of a Pt capping layer results in a notable reduction in the transmission of the sample. This result, together with the fact that the Pt layers are significantly thinner than the YIG films, indicates strong light-Pt interactions, thereby indirectly supporting the above-discussed results that the PSV effect is related to the excitation in the Pt.

Figure 4.4(b) presents the voltages obtained when optical filters were inserted between the light bulb and the sample. The figure shows the voltage data for 12 filter combinations, all

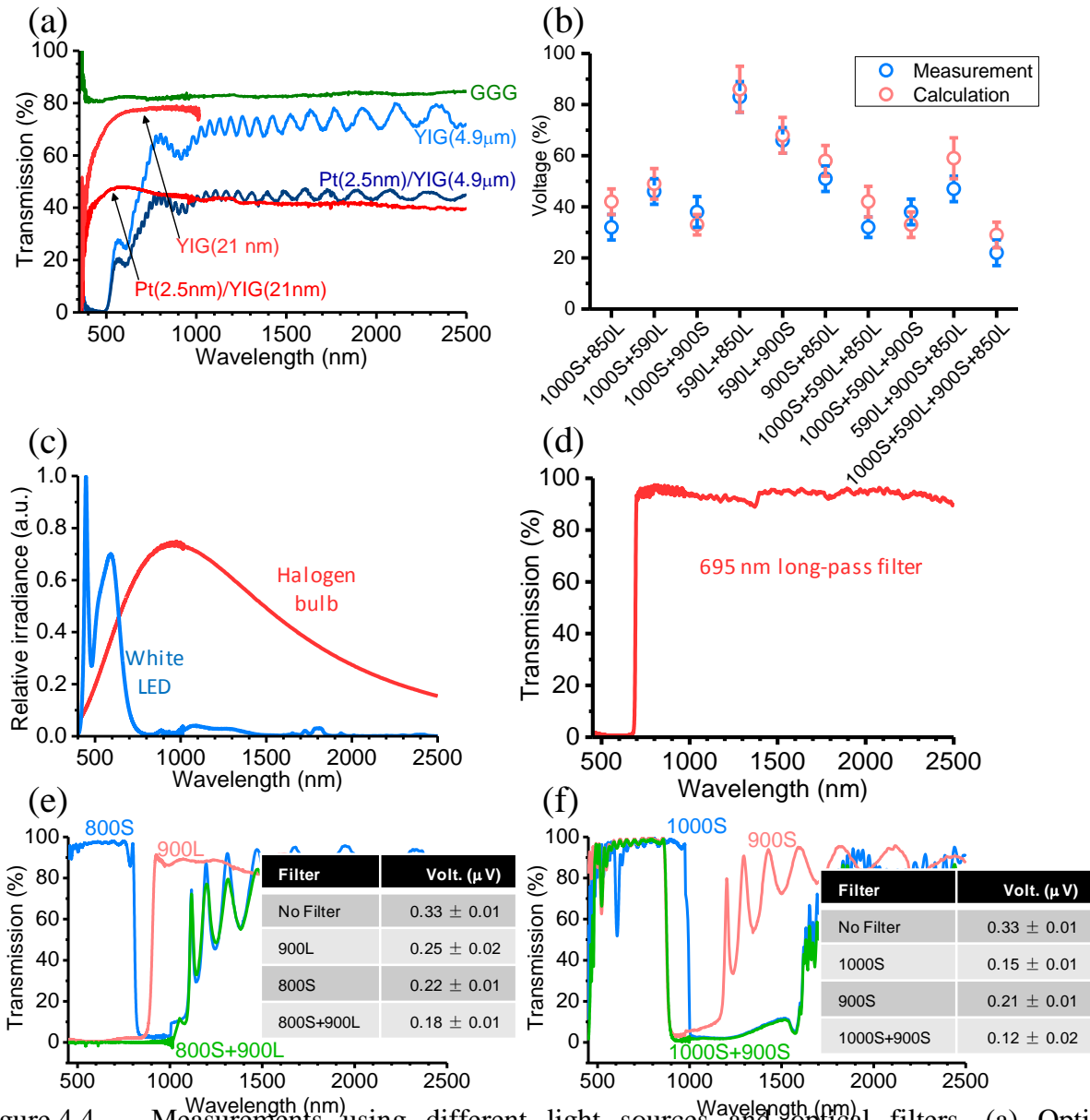


Figure 4.4 Measurements using different light sources and optical filters. (a) Optical transmission values of five samples. (b) Voltages obtained using different filters (normalized to the voltage with no filter). The blue and red symbols show the measured and calculated voltages, respectively. ‘###S(L)’ denotes a ###-nm short-(long-)pass filter. The error bars are the standard deviations of the voltage measured during light illumination. (c) Optical spectra of a 100 W halogen light bulb and a 40 W LED lamp. (d) Transmission profile of a long-pass filter. (e) Optical transmission values of two filters used either separately or together. The table in (e) presents the measured voltages for the four filter configurations shown. (f) Data of another two filters shown in the same format as in (e).

normalized to the voltage measured with no filters. The figure also includes results which were calculated by using a multiplication rule and the data measured with a single filter inserted.

The multiplication rule states that the degrading factor of the observed PSV signal due to the use of multiple filters is the product of the degrading factors due to each single filter. If one defines the PSV signal with no filter, with only filter A, with only filter B, and with both filters A and B as V_0 , V_A , V_B , and V_{AB} respectively, the multiplication rule can be expressed as

$$\frac{V_{AB}}{V_0} = \frac{V_A}{V_0} \times \frac{V_B}{V_0} \quad 4.1$$

The establishment of the multiplication rule observed in the experiment implies that the PSV must be generated by the light in a relatively narrow wavelength (λ) range, as argued below.

From experimental observations, it is reasonable to write down the PSV signal as

$$V = \int T(\lambda)I(\lambda)C(\lambda)d\lambda \quad 4.2$$

where $T(\lambda)$ is the general transmission of the light filter(s), $I(\lambda)$ is the general incident total light intensity, and $C(\lambda)$ is the general conversion function between the incident light intensity and the PSV signal. All of these three parameters are functions dependent on λ . Then the multiplication rule implies that the following relation for the two filters, A and B, is satisfied

$$\begin{aligned} & \int I(\lambda)C(\lambda)d\lambda \times \int T_A(\lambda)T_B(\lambda)I(\lambda)C(\lambda)d\lambda \\ &= \int T_A(\lambda)I(\lambda)C(\lambda)d\lambda \times \int T_B(\lambda)I(\lambda)C(\lambda)d\lambda \end{aligned} \quad 4.3$$

Considering the complicated behaviors for $I(\lambda)$, $T_A(\lambda)$, and $T_B(\lambda)$, generally Equation 4.3 is not satisfied since the integration and multiplication operations do not commute. To satisfy Equation 4.3, the special condition $C(\lambda) = C_0\delta(\lambda - \lambda_0)$ must be satisfied, where $\delta(\lambda)$ is the Dirac delta function. This condition signifies that the main contribution for the PSV signal must come from the light in a narrow wavelength region centered around λ_0 .

One can see from Figure 4.4(b) that the experimental voltages agree well with the calculated values for all 12 configurations, which evidently indicates that only a relatively narrow

wavelength range, rather than a broad spectrum, is responsible for the PSV effect. Note that the response of the various short-pass and long-pass filters used in this experiment are not ideal. The short-pass filters in particular function more like band-stop than edge filters. See, for example, the blue curve in Figure 4.4(e) for the 800 nm short-pass filter. However, it was possible to take advantage of the complicated response of these filters and do more extensive comparisons to the theory described below.

To further identify the critical wavelength, several measurements were carried out as described below. First, measurements were performed that used a 40 W white LED lamp with the spectrum shown in Figure 4.4(c), instead of the halogen bulb. The measurements, however, yielded very weak signals. This result confirms the above conclusion that the visible light does not make a major contribution to the voltage signal. Second, measurements that used a filter with the transmission shown in Figure 4.4(d) gave a very strong signal (92.2% of the signal obtained with no filters). This result further confirms that light with $\lambda < 700$ nm does not play a leading role. Third, as shown in Figure 4.4(e), measurements using an 800 nm short-pass filter and a 900 nm long-pass filter indicate that light in the range $700 \text{ nm} < \lambda < 1000 \text{ nm}$ also makes a very small contribution to the PSV effect. Note that the voltage ($0.18 \mu\text{V}$) measured with both the 800S and 900L filters used is very close to the value ($0.17 \mu\text{V}$) calculated using the multiplication rule, which firmly suggests that light in the range $700 \text{ nm} < \lambda < 1000 \text{ nm}$ is not responsible for the PSV effect. Finally, as shown in Figure 4.4(f), measurements using a 900 nm short-pass filter and a 1000 nm short-pass filter indicate that light in the range $900 \text{ nm} < \lambda < 1600 \text{ nm}$ does not make a significant contribution to the PSV effect either. As for the situation shown in Figure 4.4(e), the data in Figure 4.4(f) also show that the voltage ($0.12 \mu\text{V}$) measured with both the two filters used is very close

to the value (0.11 μV) calculated using the multiplication rule, which further suggests that the wavelength critical for the PSV effect lies in the range 1600-2000 nm.

In addition, the data obtained using the LED lamp and the 695 nm long-pass filter also confirm that the PSV effect is not associated with the excitation in the YIG. This statement is based on the facts that YIG films have a bandgap of about 2.8 eV (443 nm) and light with $\lambda < 443$ nm can induce excitations in the YIG.⁶⁸ If the PSV effect relies on the excitations in YIG, one would expect stronger voltage signals when the LED was used, because the LED emits a higher intensity of light in the range $\lambda < 443$ nm than the halogen bulb, as shown in Figure 4.4(c); one would also anticipate no measurable signals when the 695 nm long-pass filter was used, because the filter shows no transmission in the $\lambda < 695$ nm range.

4.5 Physical mechanism of the photo-spin-voltaic effect

On the basis of the experimental observations, it is believed that the PSV effect results from the photon-driven, spin-dependent excitation of electrons in the Pt atoms that are in close proximity to the MI. More explicitly, this effect involves physical processes which are sketched in Figure 4.5(a) and can be explained through density function theory (DFT) calculations for optical absorption⁶⁹ and spin diffusion analyses. The main macroscopic processes are described below.

First, when light illuminates the Pt/MI structure, photons with an appropriate energy excite electrons in the occupied bands in the Pt to the unoccupied bands, as indicated by the left vertical arrow in the top diagram of Figure 4.5(a) and the two vertical arrows in Figure 4.5(b).

Second, in the paramagnetic Pt atomic layers, the light-induced excitation is expected to have the same efficiency for electrons in the two spin channels. However, the excitation is spin dependent for Pt atoms in close proximity to the MI (the gridded region in Pt in Figure 4.5(a)),

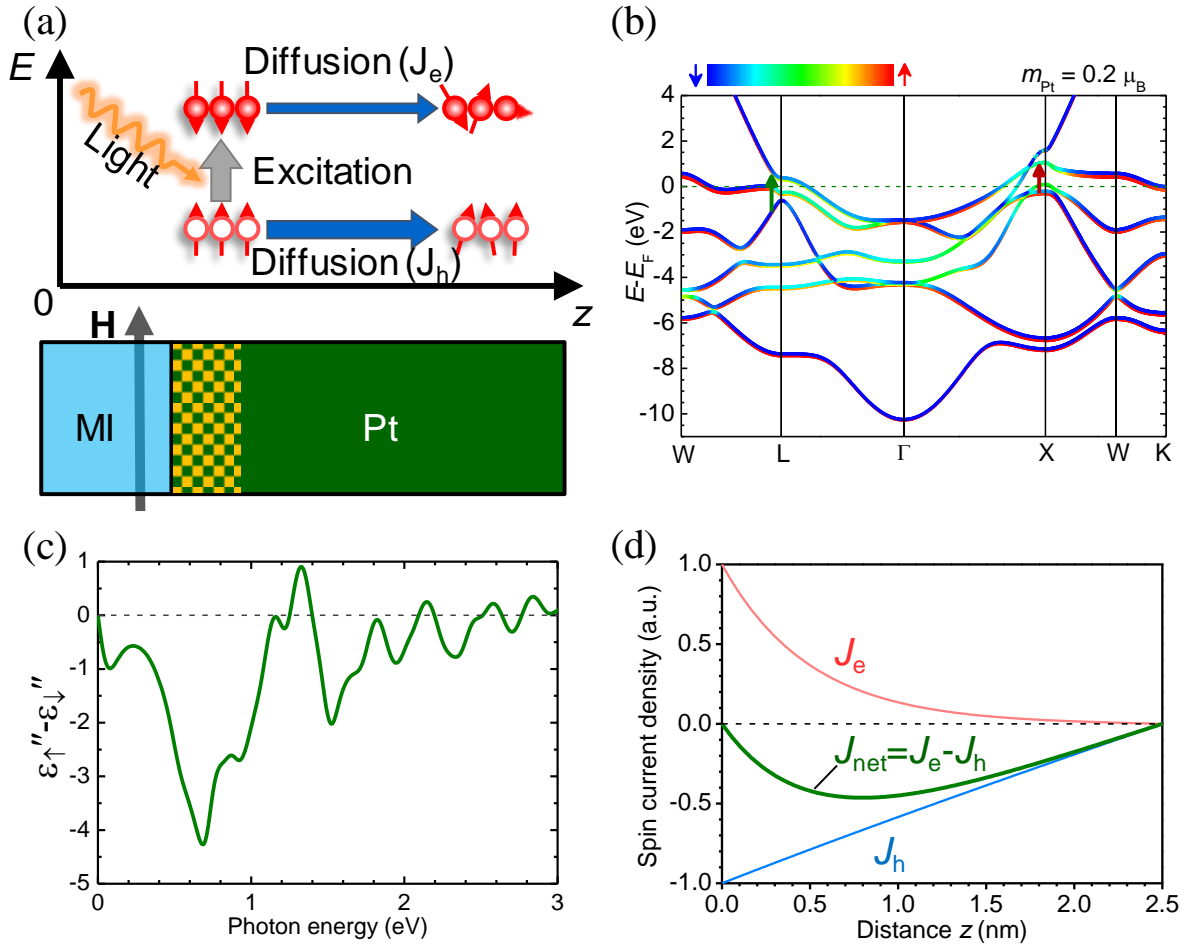


Figure 4.5 Theoretical interpretation of the PSV. (a) Sketch of the physical mechanism underlying the PSV effect. When light illuminates the sample, photons excite electrons and generate non-equilibrium hot electrons and holes in the Pt atomic layers that are in proximity to the MI (the gridded region). The excited electrons and holes diffuse from the Pt/MI interface to the Pt surface (along the $+z$ direction), giving rise to spin currents (J_e and J_h). (b) Band structure of Pt calculated using DFT with spin-orbit coupling in the presence of a magnetic moment of $0.2 \mu_B$ per atom. (c) Calculated difference between the imaginary parts of the dielectric functions for the spin-up and spin-down channels. (d) Spatial distributions of spin currents carried by hot electrons and holes. For the calculations, the Pt thickness was chosen to be 2.5 nm, and the spin mean free paths for the hot electrons and holes in the Pt film were chosen to be 0.5 nm and 5.0 nm, respectively.

because those atoms are spin polarized and show ferromagnetic-like behavior.^{25,70-72} In other words, there are proximity-induced magnetic moments in the Pt atomic layers near the interface, and the presence of these moments gives rise to a difference in the excitation efficiency for electrons in the two spin channels. In fact, the DFT calculations, performed at UC Riverside,⁶¹

indicate that the excitation of spin-down electrons is more efficient than that of spin-up electrons, as shown in Figure 4.5(c). The excitation process sketched in the top diagram of Figure 4.5(a) is consistent with this result.

Third, the diffusion of the excited electrons and holes in the Pt from the ferromagnetic region to the paramagnetic region gives rise to spin currents J_e and J_h , respectively, as shown in the top diagram in Figure 4.5(a). At first glance, there is no net spin flow because the electrons and holes carry exactly opposite spins. In practice, however, the holes in the occupied bands have lower energy, and thereby a longer spin mean free path than the electrons in the unoccupied bands. This difference results in a much larger spin current for the holes than for the electrons, and thus a net spin current $J_{\text{net}} = J_e - J_h$, as shown in Figure 4.5(d). The configuration shown in Figure 4.5(a) corresponds to a net spin current that has a polarization along \mathbf{M} , which is consistent with the spin flows depicted in Figure 4.2(a).

4.6 Comparison of experiment and theory

The above interpretation is qualitative in the sense that there is no clear boundary between the ferromagnetic and paramagnetic regions in the Pt. Nevertheless, the interpretation captures the essence of the physical process of the PSV effect and is supported by the experiments, as explained below.

First, because the PSV effect relies on the excitations in the Pt, not in the MI, one can expect similar voltage signals from samples made of different MIs. This expectation is met by the data shown in Figure 4.3 which were obtained with four samples with very different MIs. One can also expect the absence of the PSV effect in samples where the Pt layer is replaced by other normal

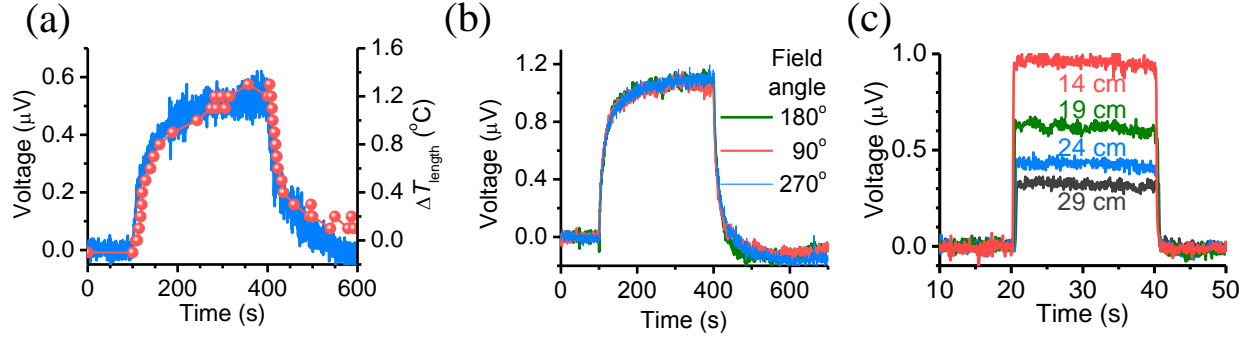


Figure 4.6 Control measurements. (a) Voltage (curve) and temperature (symbols) signals measured across the length of a 20-mm-long, 1.75-mm-wide Cu(16 nm)/YIG(36 μm)/GGG(0.4 mm) sample with \mathbf{M} along the $+y$ direction. (b) Voltage signals obtained for three different field orientations from a 21-mm-long, 1.7-mm-wide Pt(8.5 nm)/GGG(0.5 mm) sample. (c) Voltage responses for different light-to-sample distances obtained with an 18-mm-long, 1.65-mm-wide Pt(2.6 nm)/Ga-doped YIG(78 μm)/GGG(0.4 mm) sample with \mathbf{M} along the $+y$ direction. All the data were obtained using a 100 W halogen light bulb placed above the Cu or Pt side of the sample. For the data in (a) and (b) the bulb was 10 cm away from the sample and was turned on at 100 s and off at 400 s. For the data in (c), the bulb was turned on at 20 s and off at 40 s. The electrode separation was about 3.8 mm for all the measurements.

metals supporting no spin-dependent electron excitations. In fact, measurements using Cu/YIG and Cu/BaM yielded no notable PSV signals when ΔT_t and ΔT_l were comparable to those cited above. When ΔT_l was relatively large, we did observe voltage signals, which, however, changed with time in the same manner as ΔT_l , as shown in Figure 4.6(a). These signals resulted from the Seebeck effect.²¹

Second, the sign of the spin voltage at the interface depends on the magnetic ordering in the Pt atomic layers in proximity to the MI, whereas the latter is induced by \mathbf{M} in the MI.⁷⁰⁻⁷² For this reason, it is expected that a rotation of \mathbf{M} in the MI will result in a change in the polarization of the spin current in the Pt, and the absence of the MI will give rise to no PSV signals. The first expectation is clearly shown by the dependence on the \mathbf{M} orientation shown in Figure 4.2(b) and Figure 4.3(a) and (b). The second is proven by measurements on Pt/GGG samples. When ΔT_l in the Pt/GGG was relatively large, we observed only Seebeck-effect-produced voltages signals,²¹

which changed with time in the same manner as ΔT_1 , and showed no dependence on the field direction, as shown in Figure 4.6(b).

Third, the excitation processes in the Pt should be independent of the direction of light illumination, which is consistent with the experimental observations for different light configurations shown in Figure 4.2(c) and Figure 4.3(a) and (b). This expectation is further confirmed by the data shown in Figure 4.9. The processes, however, depend on the light intensity, which is clearly indicated by the data in Figure 4.6(c) as well as by the fact, shown in Figure 4.3, that the voltage signal measured for light illuminating both sides of a sample is equal to the sum of the signal for light illuminating one side of the sample.

Fourth, the theoretical results in Figure 4.5(c) suggest that the PSV effect is strong in a relatively narrow wavelength region centered at about 0.7 eV. This agrees with the above-discussed experimental observations that the PSV effect depends only on a relatively narrow light wavelength range, and such wavelengths are most likely within the range 1600-2000 nm.

Finally, in addition to the qualitative agreements between the experimental observations and the theory discussed above, there exist also quantitative agreements between the experimental and theoretical results. Figure 4.7 shows the comparison of measured and calculated voltages when using filters. The solid circles show the experimental voltages normalized to the voltage obtained without using any filters. The empty circles give the voltages calculated by

$$V = \frac{\int I(\lambda)T(\lambda)(\varepsilon_{\uparrow}'' - \varepsilon_{\downarrow}'')d\lambda}{\int I(\lambda)(\varepsilon_{\uparrow}'' - \varepsilon_{\downarrow}'')d\lambda} \quad 4.4$$

where $I(\lambda)$ is the experimentally measured light intensity of the halogen lamp, as shown in Figure 4.4(c), $T(\lambda)$ is the experimentally measured filter transmission, examples of which are shown in Figure 4.4(d), (e), and (f), and $\varepsilon_{\uparrow}'' - \varepsilon_{\downarrow}''$ is theoretically calculated using DFT, as shown in Figure 4.5(c). One can see that the measured voltages match very well with the calculated voltages for

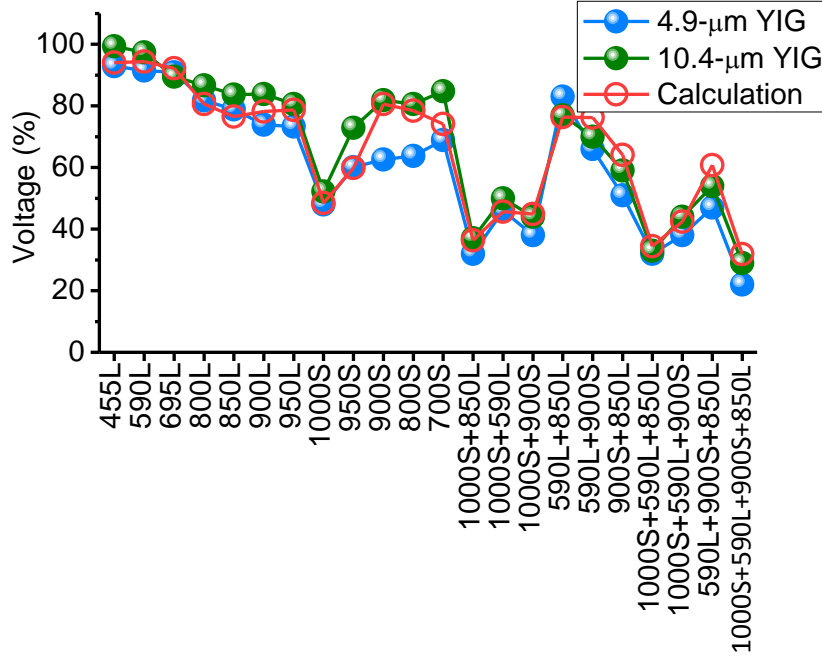


Figure 4.7 Comparison of voltages measured and calculated when optical filters were used. The measured voltages are normalized to the voltage obtained without using any filters. The calculations were carried out with Equation 4.4. ‘###S(L)’ denotes a ###-nm short-(long-)pass filter. ‘4.9-μm YIG’ denotes the same sample as described in Figure 4.2 and Figure 4.3(a). ‘10.4-μm-YIG’ denotes a 5.8-mm-long, 1.8-mm-wide Pt(2.6 nm)/YIG(10.4 μm)/GGG(0.4 mm) sample. The measurements were performed with the same light and field configurations as for the data shown by the red curve in Figure 4.2(b).

the majority of the 22 different filter configurations. What is more, such matching is true for both of the two samples.

One important point should be made about the above experiment/theory – if one shifts the peak center of the profile $|\epsilon_{\uparrow}'' - \epsilon_{\downarrow}''|$ from 0.7 eV to 1.3 eV, the level of agreement between the calculated and measured voltages decreases notably, as shown in Figure 4.8. Specifically, Figure 4.8 gives three sets of voltage values calculated using three different $|\epsilon_{\uparrow}'' - \epsilon_{\downarrow}''|$ profiles: (1) the actual DFT result as presented in Figure 4.5(c), (2) a Gaussian profile that best fits the main peak of the DFT result which is centered at 0.7 eV and has a width of 0.5 eV, and (3) a Gaussian profile that is the same as (2) but with its center shifted to 1.3 eV. While the agreement between the experimentally measured voltages and the theoretically calculated voltage values are satisfactory

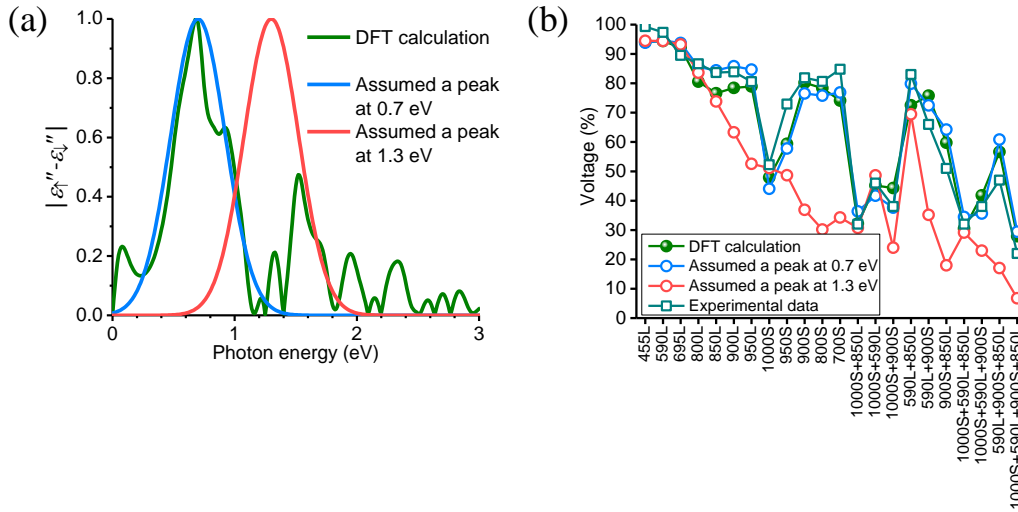


Figure 4.8 Wavelength characteristics of the PSV effect. (a) $|\epsilon_{\uparrow}'' - \epsilon_{\downarrow}''|$ profiles, which are the difference between the imaginary parts of the dielectric functions for the spin-up and spin-down channels. The green profile was obtained by DFT calculations and is the absolute value of the value shown in Figure 4.5(c). The blue profile shows a Gaussian profile that fits the main peak of the green profile centered around 0.7 eV. The red profile shows a Gaussian profile that is the same as the blue profile but with the peak center shifted to 1.3 eV. (b) Comparison of voltages measured and calculated when the optical filters were used. The measured voltages are normalized to the voltage obtained without using any filters. ‘###S(L)’ denotes a ###-nm short-(long-)pass filter. The measurements were performed with the same light and field configurations as for the data shown by the red curve in Figure 4.2(b), and the sample was a 5.8-mm-long, 1.8-mm-wide Pt(2.6 nm)/YIG(10.4 μ m)/GGG(0.4 mm) structure. The calculations were carried out using Equation 4.4 and the three $|\epsilon_{\uparrow}'' - \epsilon_{\downarrow}''|$ profiles given in (a).

for both cases (1) and (2), it is much worse for case (3). This result clearly indicates the importance of having the correct data of the absorption spectra. This result, together with that shown in Figure 4.7, indicates the strong dependence of the PSV effect on the band structure of the Pt or, more explicitly, the strength of the spin-orbit coupling in the Pt.

The results of Figure 4.7 and Figure 4.8 also indicate the critical wavelength range for the PSV effect in the Pt/MI system which should be around 1800 nm (0.7 eV). This agrees with the experimental observation presented in Figure 4.4, namely, that there exists a narrow wavelength range over 1600–2000 nm that is critical for the PSV effect. This agreement, together with the facts that the Pt layer-caused reduction in the transmission of the sample is almost constant over the

entire λ range and the light-on-Pt configuration yield weaker PSV signals than the light-on-MI configuration, provides evidence that the PSV effect mainly originates from an optical effect, not a thermal effect, when illuminated by the halogen lamp. In case that light-induced Pt heating plays an important role, one would expect that the Pt layer would cause a larger reduction in the optical transmission at a relatively narrow λ range centered at about 1800 nm, and the voltage signals for the light-on-Pt configuration should be stronger than those for the light-on-MI configuration.

4.7 Mixing of the photo-spin-voltaic and spin Seebeck effects

There have been previous experiments on using light to create a temperature gradient and thereby realize the SSE.^{45,73-75} Those experiments also used Pt/MI structures, the same as this work. It is possible that the SSE and the PSV effect occur simultaneously in a Pt/MI structure upon exposure to light. When the temperature difference across the sample thickness, ΔT_t , is very small, one can expect that the PSV effect overwhelms the SSE, and the measured voltage signals resulted mainly from the PSV effect. This is exactly the case in this work, where the experimental setup was constructed to minimize ΔT_t . When ΔT_t is relatively large, the SSE is dominant, which is the case studied in Chapter 4 and References [45],[73]-[75]. Note that in the experiments reported in References [73]-[75] the SSE might be the only effect, because the wavelength of the laser used for heating is far shorter than the critical wavelength range identified in this work, and the PSV effect might be completely absent. In a regime where ΔT_t is neither very small nor very large, the two effects may coexist. This situation is shown in Figure 4.9. One can see from the data in Figure 4.9 that, different from the PSV effect, the SSE voltage signal flips its sign when the light

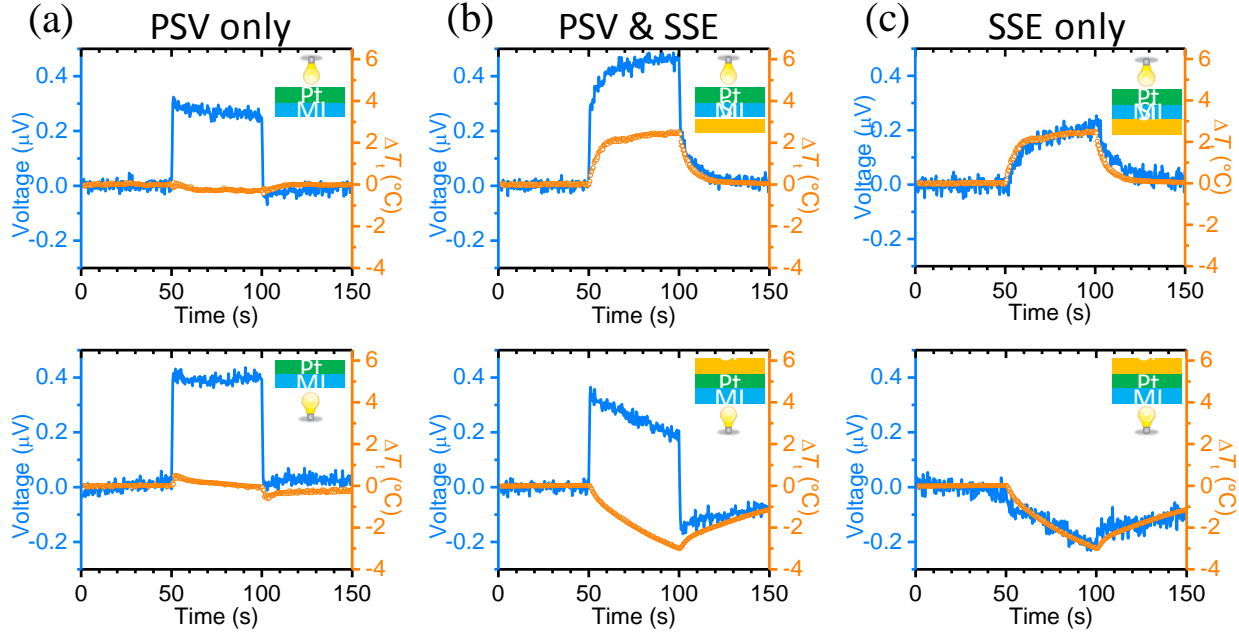


Figure 4.9 Comparison between PSV- and SSE-produced voltage signals. (a) and (b) present the voltage and temperature ΔT_t signals measured without and with the use of a heat sink, respectively, where ΔT_t is the temperature difference measured across the sample thickness. The sample and measurement configurations were almost identical to those described for the data in Figure 4.2(c), and for all the measurements the light was turned on at $t=50$ s and then off at $t=100$ s. The situation in (a) corresponds to a regime where ΔT_t is very small and the PSV effect overwhelms the SSE. The situation in (b) corresponds to a regime where ΔT_t is relatively large due to the use of a heat sink and the PSV effect and the SSE take place simultaneously and both contribute to the voltage signals. (c) presents the SSE voltage signals where were obtained by subtracting the PSV voltage signals in (a) from the voltage signals in (b). The temperature signals in (c) are the same as presented in (b).

illumination direction is reversed, and the SSE voltage varies with time in the same manner as ΔT_t . These results evidently confirm that the PSV effect is essentially different from the SSE. Note that it has been studied previously that the SSE voltage vs. time responses should follow the ΔT_t vs. time response.^{45,75}

It is possible that upon the exposure of a Pt/Mi sample to light, the light absorption raises the temperature of the electrons in the Pt and thereby quickly triggers imbalance among electron, phonon, and magnon systems at the interface, potentially leading to an interface-related SSE. It is believed that such an interface SSE should be weak in the experiments in this work, because it is

a thermal effect and should not depend on the wavelength of the light, while the observed voltage signals exhibit strong wavelength dependence, as shown in Figure 4.4, Figure 4.5, and Figure 4.7. The interface SSE is expected to be weak because the exchange of angular momentum between hot electrons (and holes) and quasiparticles (magnons and phonons) is low due to their large energy mismatch. The hot electrons have an energy of a few tenth eV, while the magnons and phonons have an energy of a few meV only. What is more, even though the hot electrons may interact with the magnons, this interaction would have weak spin dependence due to the high energy of the hot electrons. Besides, the current SSE theory is based on the quasi-equilibrium of magnon, phonon, and electron systems; and in the theory both the temperatures and their gradients are well defined.²³ This is not applicable to the PSV effect, for which the electrons in the Pt are far from their equilibrium state and the temperature of electrons is not defined. Of course, the spin-selective reflection of hot electrons from the Pt/MI interface may also contribute to spin currents in the Pt.

It is known that the efficiency of the light-induced heating somewhat depends on the product of $\varepsilon_{\uparrow}'' + \varepsilon_{\downarrow}''$ and the photon energy, E . This product was calculated from the band structure of Pt, as shown in Figure 4.10(b). One can see a broadband response in the 0.5-3 eV range (or 410-2500 nm in wavelength). The broadband behavior of $(\varepsilon_{\uparrow}'' + \varepsilon_{\downarrow}'') \times E$ is in contrast to the peak behavior of the $\varepsilon_{\uparrow}'' - \varepsilon_{\downarrow}''$ spectrum shown in Figure 4.10(a). Two important points should be made about the results shown in Figure 4.10. First, the results indicate that the peak heating efficiency should occur at the photon energy of about 0.98 eV (1270 nm), but the experimental data clearly indicate that the critical wavelength is not in this region. Second, these results also indicate that the heating efficiency at 2.06 eV (600 nm) should be large, but the experimental data show that the measurements using a white LED source, at 600 nm, yielded very weak PSV signals. These

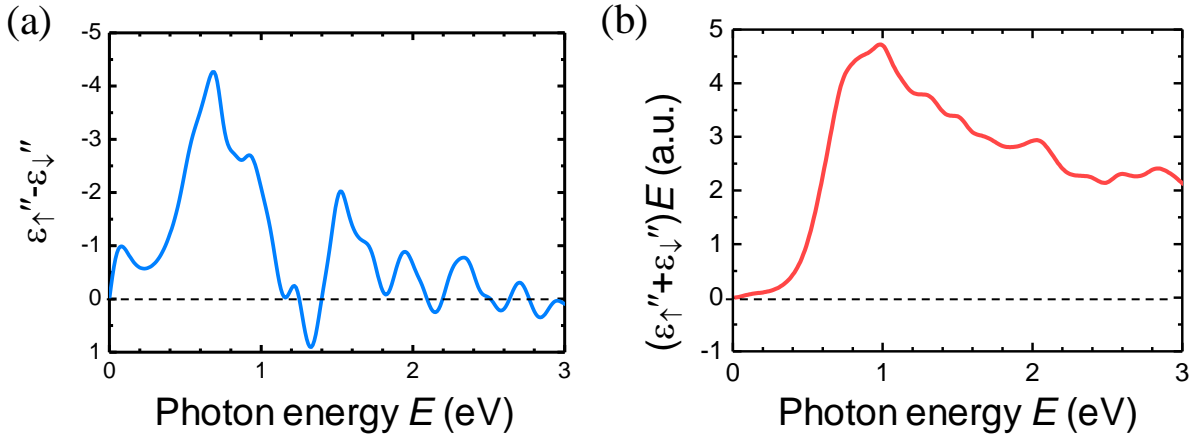


Figure 4.10 Calculated absorption profiles. (a) $(\epsilon''_{\uparrow} - \epsilon''_{\downarrow})$ profile. (b) $(\epsilon''_{\uparrow} + \epsilon''_{\downarrow}) \times E$ profile. ϵ''_{\uparrow} and ϵ''_{\downarrow} are the imaginary parts of the dielectric functions for spin-up and spin-down channels, respectively, and E is the photon energy. The ϵ''_{\uparrow} and ϵ''_{\downarrow} data were obtained through DFT calculations and are the same as those used to calculate $\epsilon''_{\uparrow} - \epsilon''_{\downarrow}$ in **Error! Reference source not found.**(a).

two facts provide additional support to the conclusion that heating effects are weaker than the PSV effect in the experiments presented in this work.

There are three additional notes which should be made. First, the wavelength characteristics of the PSV effect results from the energy dependence of the light-induced hot electron excitation. The spin-orbit coupling in the Pt that converts spin currents to charge currents is energy independent, just as in the SSE. Second, for the SSE voltage signal presented in Figure 4.9, the physical process involves lattice-heated Pt electrons, not the hot electrons directly excited by light. Those heated electrons have lower energy than the hot electrons. Finally, there might exist a charge current across the thickness of the Pt layer at the onset of illumination due to the different diffusion properties of the excited hot electrons and holes. However, this current, if present, should be transient because there is no complete circuit for it to flow in. For this reason, the PSV produced spin current is not a spin-polarized electron current, but a pure spin flow, and there is neither the ordinary Hall effect nor the anomalous Hall effect in the structure.

4.8 Summary

This work reports that a spin voltage can be created by photons in a non-magnetic metal that is in close proximity to a magnetic insulator: the photo-spin-voltaic effect. The PSV effect presented here differs from the phenomena of light-induced generation of pure spin currents reported previously,^{45,73-83} as explained below.

First, the effects demonstrated in Refs. [76]-[82] occur in semiconductors only, not in normal metals. Furthermore, except for the case in Ref. [82] they also require the use of polarized light. Second, the spin current generation presented in Ref. [83] relies on the excitation of surface plasmon resonances. Finally, the effects reported in Refs. [45],[73]-[75] made use of light to create a temperature gradient and the SSE to produce spin currents. In this case, the PSV effect and the SSE might coexist, as shown in Figure 4.9.

One can also expect that the PSV effect may open the door to new optical-spintronic applications, including light-based spin batteries, sensing orientations of magnetic moments or fields, and converting light energy to electricity.

CHAPTER 5 Distinction between the

photo-spin-voltaic and spin Seebeck effects

5.1 Overview

The work presented in Chapter 4 has demonstrated that plain light can induce a spin voltage in a Pt thin film in proximity to a magnetic insulator (MI) via the photo-spin-voltaic effect.⁶¹ This effect offers a new method for spin current generation, as an alternative to spin pumping,^{9,58,59} the spin Hall effect,^{5,6,8,60,84} and the spin Seebeck effect.^{22,24,25,36-39} It is believed that the essence of the PSV effect is the photon-driven, spin-dependent excitation of electrons in Pt atomic layers near the interface that show ferromagnetic-like behavior due to proximity to the MI; the excited electrons and holes diffuse away from the interface in different manners, producing an effective spin voltage at the interface and a corresponding pure spin current across the Pt thickness. Although this interpretation has been supported by previous experiments to some degree,⁶¹ a number of fundamental questions remain outstanding, including whether the PSV effect shows a different wavelength and temperature characteristic from the SSE and whether the PSV effect occurs in non-magnetic metals other than Pt. The first question is of great importance because light illumination can also produce heat and thereby induce a temperature gradient and the SSE. The SSE also generates a pure spin current across the Pt thickness that varies with the magnetization orientation in the MI²² and the intensity of the light^{45,74} in exactly the same manner as the PSV effect, leading to entanglement of the two effects. This entanglement calls for experimental evidence distinguishing the PSV effect from the SSE. The second question regards the proof of

the universality of the PSV phenomenon, which is not only fundamentally intriguing but is also a necessity in terms of searching for materials exhibiting the strongest PSV effect.

This work reports experiments that confirm the difference between the PSV effect and the SSE. Experiments use normal metal (NM)/MI bi-layered structures where the NM layers is Pt, Pd, Au, or Cr and the MI layer is YIG, and four light sources that cover different parts of the optical spectrum. One cannot compare directly the PSV strength for different light sources, as the light intensity varies between them. Instead, the experiments are conducted in a configuration where the PSV effect and the SSE coexist, and the PSV strength is compared to the SSE strength. This configuration is realized by illuminating the sample on one side while placing a heat sink on the other side of the sample, establishing a temperature gradient across the sample thickness. The PSV- and SSE-produced pure spin currents are probed by the inverse spin Hall effect (ISHE),^{6,8,54} and the PSV and SSE components of the ISHE voltage signals are separated based on the different time dependence of the two effects.^{45,61} The data show that for all the NM/YIG samples, the PSV effect can be stronger than, similar to, or weaker than the SSE depending on the light source, providing direct evidence for the wavelength dependence of the PSV effect. The trend of the PSV strength when using different light sources changes in the four samples, indicating the different wavelength-dependent contribution from each NM to the PSV effect voltage.

5.2 Measurements of light-induced, concurrent PSV and SSE

Figure 5.1(a) shows a schematic diagram of the experimental setup. The core component is a NM/YIG sample where the YIG layer is magnetized to saturation by an in-plane magnetic

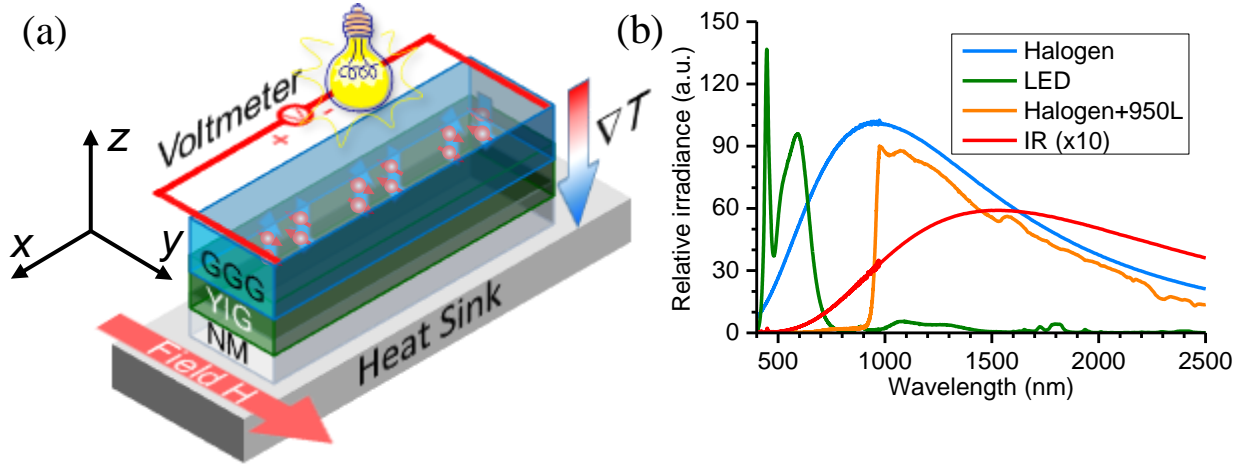


Figure 5.1 Experimental setup and light sources. (a) Experimental setup. (b) Optical spectra of four different light sources, as indicated.

field H . For the PSV/SSE measurements, the samples were placed NM-side-down on an Al heat sink and covered with a 3.71 mm by 1.22 mm mask for the Pt sample, and a 7.19 mm by 2.41 mm mask for the other samples. A light source was placed 5.5 cm over the sample. The magnetic field was provided by a pair of permanent magnets and had a magnitude of 1.1 kOe as measured by a LakeShore model 450 gaussmeter. The electric voltages were measured by a Keithly 2182A nanovoltmeter.

When the light bulb illuminates the sample from the top, it gives rise to the PSV effect in the sample and a spin current across the NM thickness.⁶¹ Together with the heat sink placed at the bottom of the sample, the light also results in a temperature gradient ∇T across the sample thickness, leading to the SSE in the sample which also produces a spin current across the NM thickness.^{22,24,25,36-39} Via the ISHE,^{6,8,54} the PSV- and SSE-produced spin currents are converted to electric voltage V_{PSV} and V_{SSE} , respectively, across the sample length (i.e. along the x axis). It is also possible that the light illumination gives rise to a temperature gradient in the sample plane and produces a non-magnetic voltage V_0 through the conventional Seebeck effect.²¹ The net effect is an overall voltage signal $V = V_{PSV} + V_{SSE} + V_0$, which can be measured by the nanovoltmeter.

The light sources used were a 40 W 120 VAC white LED bulb, a 100 W 120 VAC halogen bulb, and a ThorLabs SLS202 7.2 W infrared light source. The optical spectra of these light sources were measured with an Ocean Optics IRRAD200 visible spectrometer (350-1000 nm) and an Ocean Optics NIRQuest512-2.5 near-infrared (NIR) spectrometer (950-2500 nm). The light was collected using an Ocean Optics QP600-2-VIS-NIR patch cord with a 600 μm fiber optic core and an Ocean Optics P450-1-FLUORIDE patch cord with a 450 μm core for visible and NIR measurements, respectively.

Figure 5.1(b) presents the optical spectra of four light sources – a white LED lamp, a halogen bulb, an infrared (IR) light bulb, and a source where the halogen bulb is used together with a 950-nm long pass filter (“halogen+950L”). The spectral data clearly indicate that the four light sources cover different parts of the optical spectrum and exhibit the largest irradiances at very different wavelengths, thereby facilitating the analysis of the wavelength (λ) characteristics of the PSV effect in a given NM/YIG sample.

The experiments were carried out using four samples with four different normal metals (NM), 3.5 nm Pt, 3 nm Pd, 3 nm Au, and 3 nm Cr with 1.2 nm Al_2O_3 as a capping layer to prevent oxidation. As the Cr layer is only 3 nm thick, it is paramagnetic at room temperature,⁸⁵ although bulk Cr shows antiferromagnetic behavior with a Neel temperature of 311 K.⁸⁶ All of the NMs were deposited on YIG using DC sputtering at room temperature. The resistances of the NM layers were 1073 Ω , 569 Ω , 162 Ω , and 1707 Ω , respectively. The Pt, Pd, and Au samples used 10.4 μm , 5.9 μm , and 5.9 μm YIG films, respectively, and these YIG thin films were grown by liquid phase epitaxy (LPE) on single-crystal (111) GGG substrates. The Cr film was deposited on a 0.5 mm thick polycrystalline YIG slab. The dimensions are 5.82 mm by 1.63 mm for the Pt/YIG sample,

9.30 mm by 3.20 mm for the Pd/YIG sample, 9.14 mm by 2.79 mm for the Au/YIG sample, and 9.30 mm by 2.69 mm for the Cr/YIG sample.

5.3 Separation of entangled photo-spin-voltaic and spin Seebeck effect signals

Figure 5.2 shows the procedure for separating the voltage components V_{PSV} , V_{SSE} , and V_0 . The separation is based on the following two facts. First, when \mathbf{H} is reversed, V_{PSV} and V_{SSE} flip their signs because for both the PSV effect and the SSE the orientation of the magnetization \mathbf{M} in the YIG film dictates the polarization of the spin current in the NM layer, while V_0 does not change its sign as the conventional Seebeck effect is not a magnetic effect.²¹ Second, when the light is turned on, the PSV signal appears almost instantaneously,⁶¹ while the SSE signal arises gradually,^{45,61} showing a time dependence the same as the temperature difference across the sample thickness, as demonstrated previously.

The data in Figure 5.2 were measured with the Pt/YIG sample using the halogen bulb which is turned on at 50 s and off at 100 s. The voltage signals in Figure 5.2(a) and (b) were measured with opposite magnetic fields, as indicated, and can be denoted, respectively, as

$$V_{H>0} = V_{PSV} + V_{SSE} + V_0 \quad 5.1$$

$$V_{H<0} = -V_{PSV} - V_{SSE} + V_0 \quad 5.2$$

The appearance of the minus signs in Equation 5.2 reflects the above mentioned dependence of V_{PSV} and V_{SSE} on the direction of \mathbf{H} . It is apparent that one can eliminate the nonmagnetic V_0 by taking $(V_{H>0} - V_{H<0})/2$. This process results in the magnetic signal $V_{PSV} + V_{SSE}$ which is

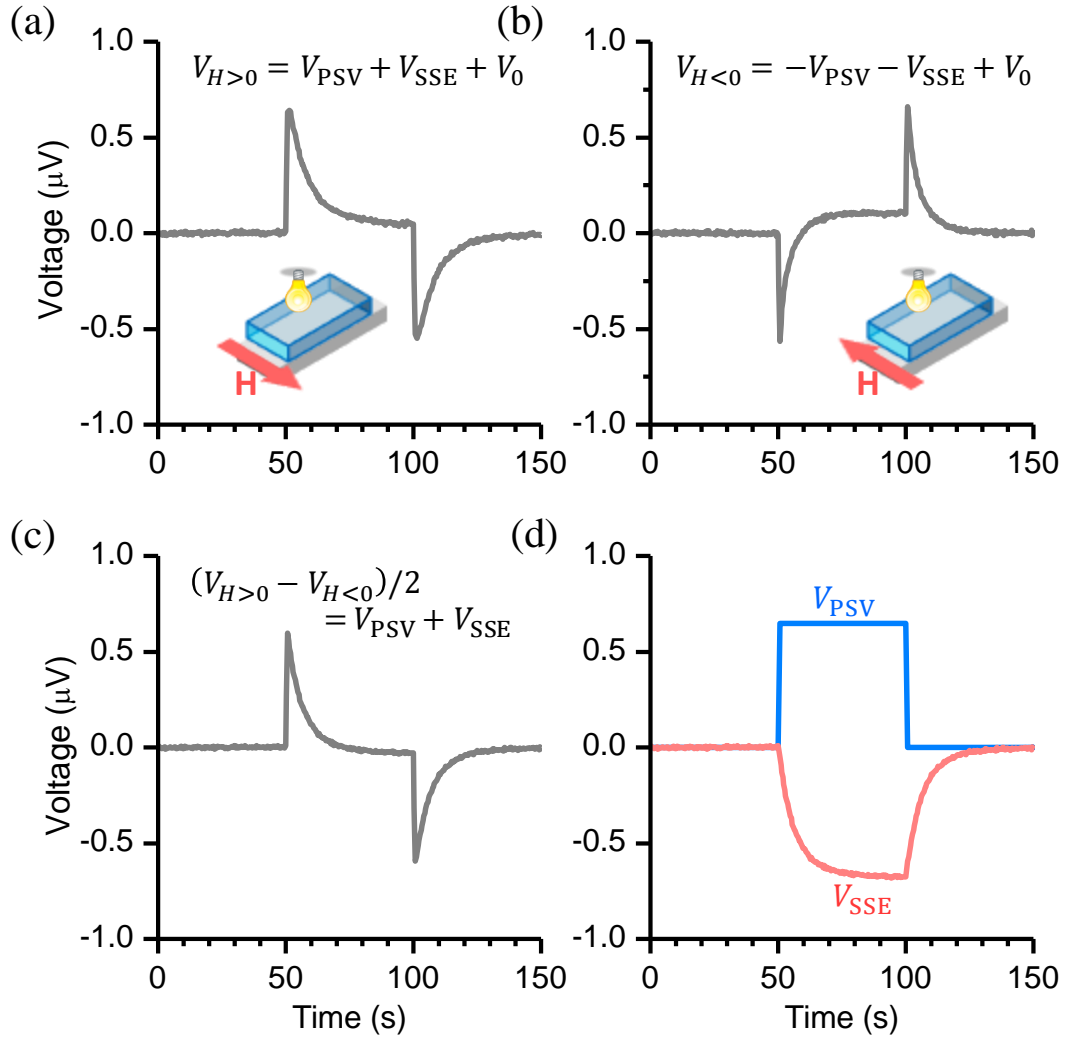


Figure 5.2 Separation of PSV and SSE signals. (a) and (b) present voltage signals measured with opposite magnetic fields. (c) shows the signal after the removal of the nonmagnetic component V_0 . (d) presents the separated V_{PSV} and V_{SSE} signals.

presented in Figure 5.2(c). Based on the configuration shown in Figure 5.2(a), one can expect that the spin currents produced by the PSV effect and the SSE have opposite polarization and the signal in Figure 5.2(c) consists of a positive PSV voltage and a negative SSE voltage. Thus, one can assume a positive, square pulse function for the PSV voltage and obtain the SSE signal by subtracting the square pulse from the magnetic signal. The resulting PSV and SSE signals are shown in Figure 5.2(d).

5.4 Responses of photos-spin-voltaic and spin Seebeck effect signals to different lights

The separation of the PSV and SSE signals allows for direct comparisons of the responses of the two signals to different light illuminations. Figure 5.3 shows representative data, with each row showing the data for a particular NM sample and each column showing the data for particular light source. In each diagram, the blue and red profiles show V_{PSV} and V_{SSE} , respectively. Each data set is the resulting magnetic signal after subtracting the averages over five measurements each for $H>0$ and $H<0$. For easy comparison, absolute voltage values are presented. In each row, the voltage scales are intentionally set so that the V_{SSE} signals have about the same level, as indicated by the horizontal red dashed line.

Several important results are evident from the voltage data in Figure 5.3. First, the PSV effect is clearly observed in all four samples, proving that the effect is universal, rather than a unique effect existing only in Pt/MI structures. Note that previous experiments made use of Pt-based samples only.⁶¹

Second, the data show that the PSV strength can be either larger than, equal to, or smaller than the SSE strength, depending on the light source. Further, this is true for all four samples. This result serves as strong evidence for the photonic nature of the PSV effect, as opposed to the thermal nature of the SSE. If the PSV effect has thermal origins like the SSE, one would expect the PSV signal to vary with the light in the same manner as the SSE signal, which is clearly not the case for the data shown in Figure 5.3.

Third, the response of the PSV signal to four light sources varies for different samples. For example, when one changes the LED source to the halogen bulb, for the Pt/YIG sample the ratio

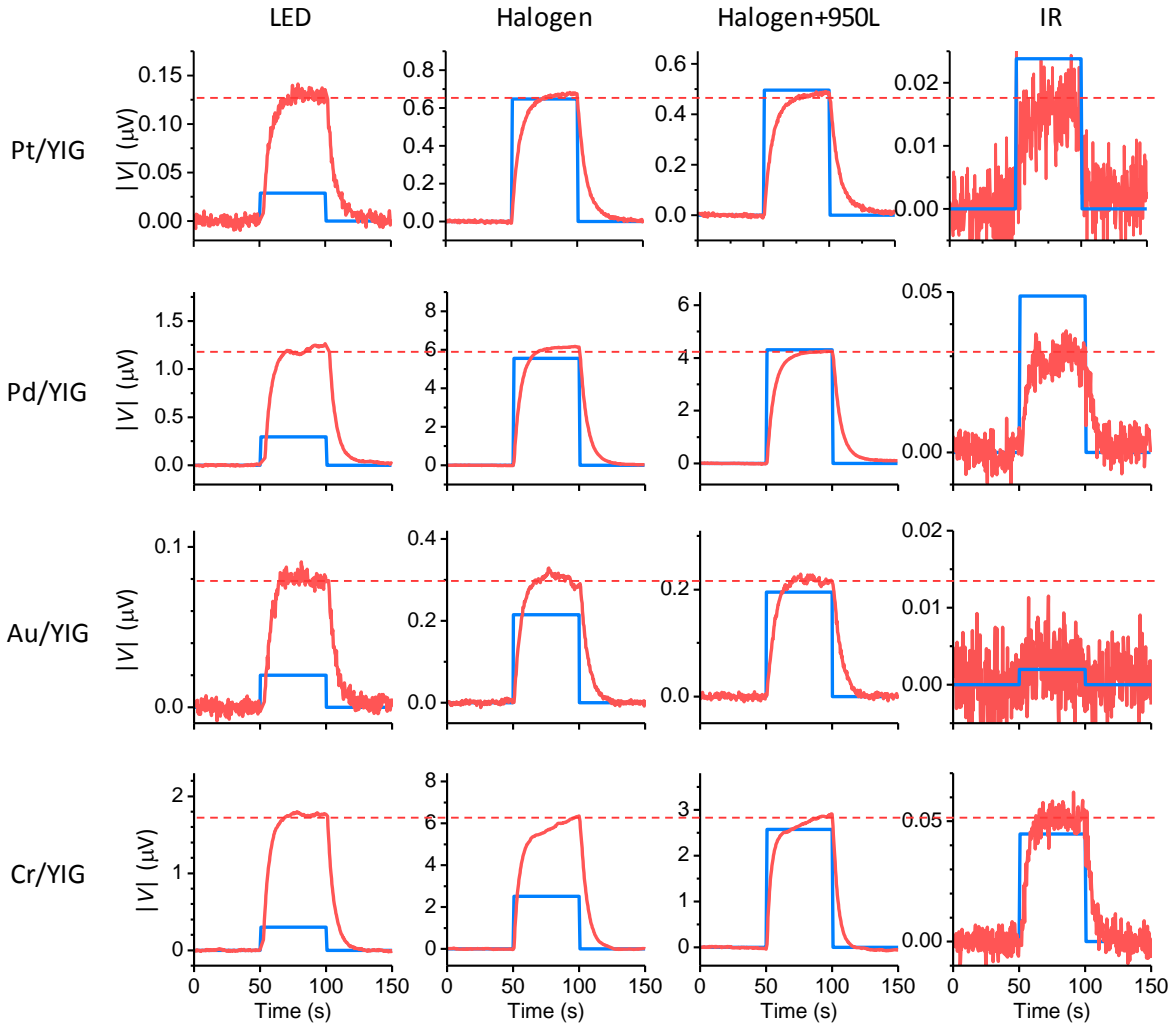


Figure 5.3 Comparisons of PSV and SSE signals. Each row shows the V_{PSV} and V_{SSE} signals obtained with the sample labeled on the left, and each column shows the signals obtained using the light labeled on top. In each diagram, the blue and red profiles show the V_{PSV} and V_{SSE} signals (absolute values), respectively. For each measurement, the light was turned on at 50 s and off at 100 s. For easy comparison of the V_{PSV} and V_{SSE} signals in response to different light illuminations, in each row the V_{SSE} signals are scaled to about the same level, as indicated by the horizontal red dashed line.

$|V_{PSV}|/|V_{SSE}|$ increases substantially as shown in the first row of Figure 5.3, while for the Cr/YIG sample the ratio increase is much smaller as shown in the last row. One can also see that, when one changes the “halogen+950L” source to the IR light, for the Pd/YIG sample the ratio $|V_{PSV}|/|V_{SSE}|$ increases notably, while for the Cr/YIG sample the ratio remains almost the same. This result evidences the unique wavelength dependence of each metal that originates from the

fact that different metals have different band structures and thereby exhibit different photon-absorption behaviors.

Finally, it should be mentioned that, with the sample dimension difference taken into consideration, the PSV signals in the Au/YIG sample are found to be one order of magnitude weaker than in the other three samples. There are two possible reasons for this observation. First, previous studies, both experimental⁸⁷⁻⁹⁰ and theoretical,²⁵ have shown that the proximity-induced moments in Au are considerably smaller than that in Pt and Pd. For example, $0.031 \mu_B/\text{atom}$ has been reported for Au atoms in proximity to Co,⁸⁷ while $0.17\text{-}0.29 \mu_B/\text{atom}$ for Pt in proximity to Ni⁹¹ and $0.14\text{-}0.40 \mu_B/\text{atom}$ for Pd in proximity to Fe⁹² have been reported. Second, the ISHE in Au is weaker than that in Pt, Pd, and Cr, as reported previously.⁹³

The $|V_{\text{PSV}}|/|V_{\text{SSE}}|$ ratio averages over four separate measurements are presented in Figure 5.4. The averaging-yielded standard deviations are shown as error bars in the figure. The ratio data shown in Figure 5.4 evidently support the results indicated by the voltage data in Figure 5.3. Specifically, for each sample the PSV strength can be smaller than, similar to, or larger than the SSE strength, depending on the wavelength characteristics of the light. What is more, the trend of the variation of the ratio with the different light illumination changes for different samples. In addition, one can see the other two results from the data in Figure 5.4. First, for the Pt/YIG sample the comparison of $|V_{\text{PSV}}|/|V_{\text{SSE}}|$ for four light sources clearly suggests that the PSV effect is stronger for the IR light. This results is consistent with previous results obtained through measurements using different optical filters.⁶¹ Second, when using the LED source, the PSV signals are much weaker than the SSE signals for all four samples, indicating that the photon energy of the LED

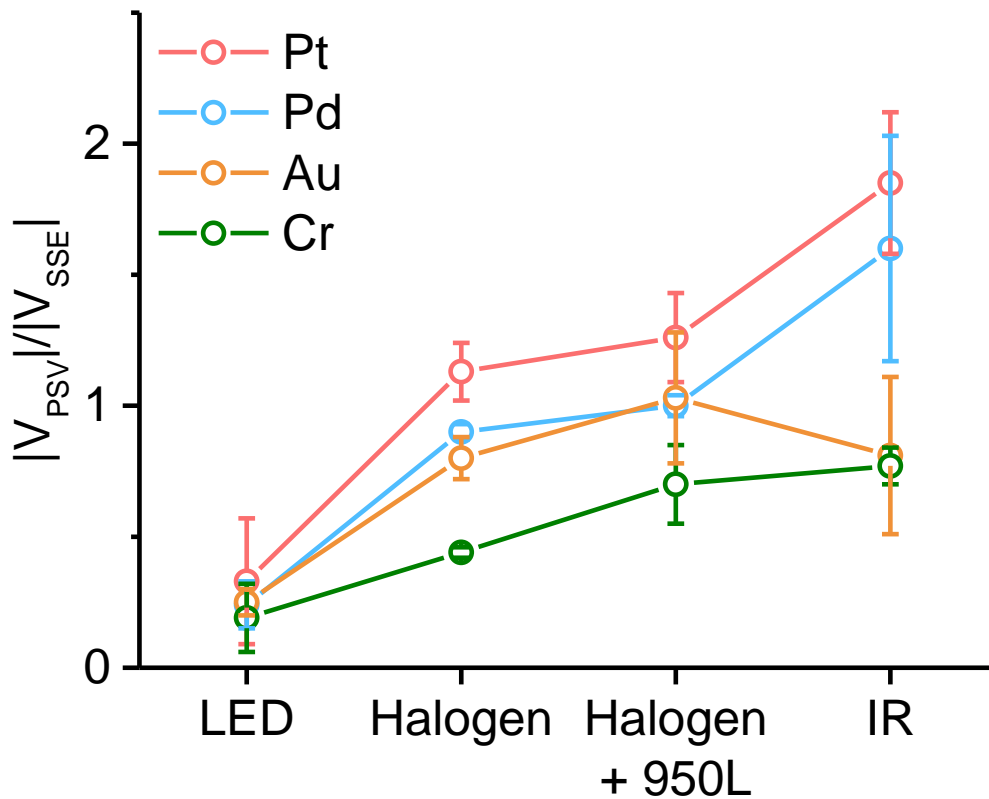


Figure 5.4 Comparison of responses to different light illuminations. The ratios of the PSV signal $|V_{PSV}|$ to the SSE signal $|V_{SSE}|$ obtained for four samples (vertical axis), as indicated, compared for four different light sources (horizontal axis).

light largely mismatches the energy at which the metal shows strongest spin-dependent photon absorption.

5.5 Control measurements

In order to ensure the accuracy of the above measurements several control measurements were carried out.

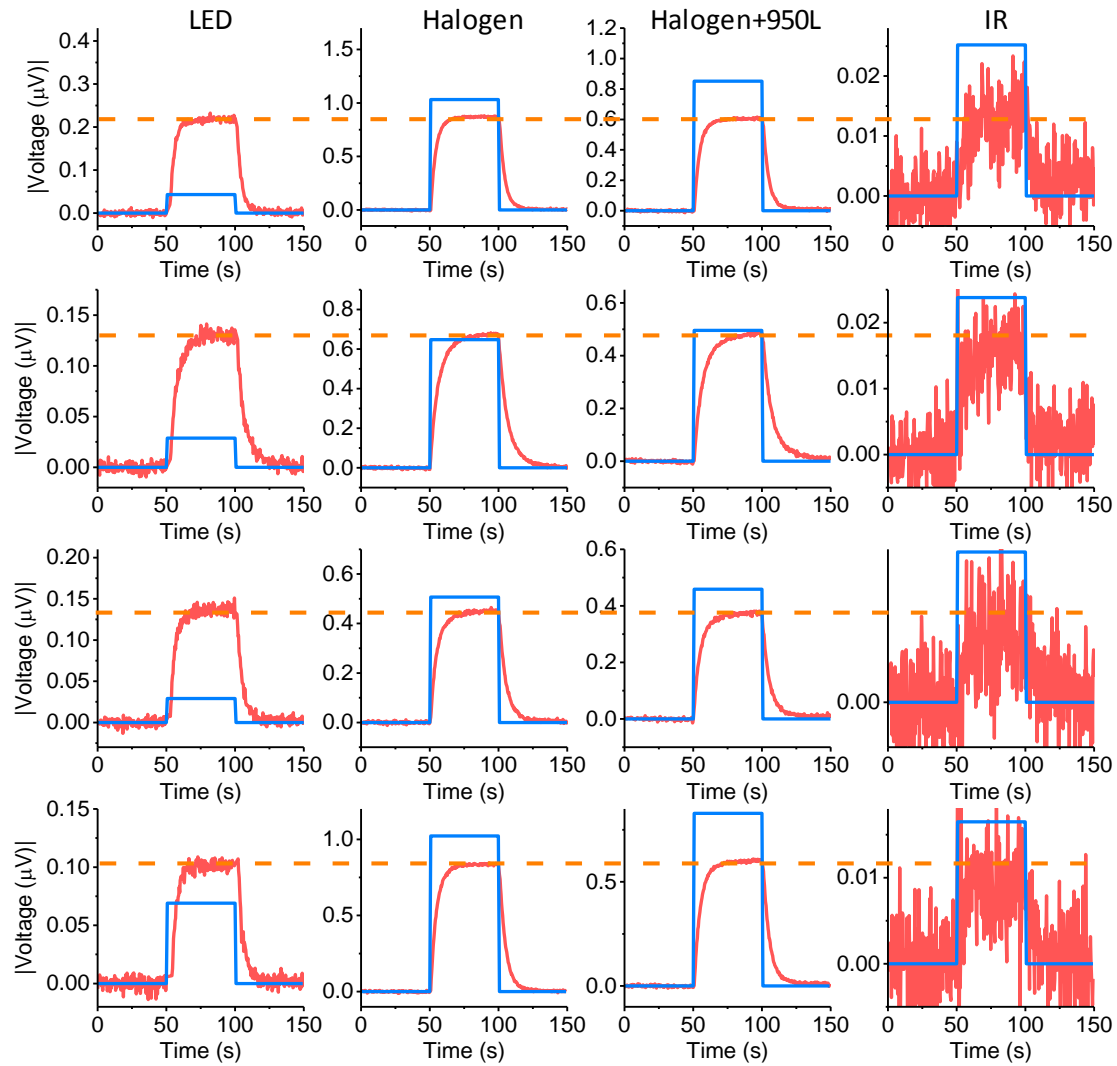


Figure 5.5 Comparison of PSV and SSE signals for Pt/YIG sample. The separated V_{PSV} and V_{SSE} signals are shown in blue and red, respectively, obtained from measurements with the light source shown on top. Each row is a different measurement instance. Between each measurement, the sample was removed and repositioned before repeating the data collection.

5.5.1 Measurement repeatability

To check the robustness of the results discussed above, the samples were removed and then re-assembled, and the measurements that yielded the data shown in Figure 5.4 were repeated three times. The full data for each sample and light source are shown in Figure 5.5-Figure 5.8, in the

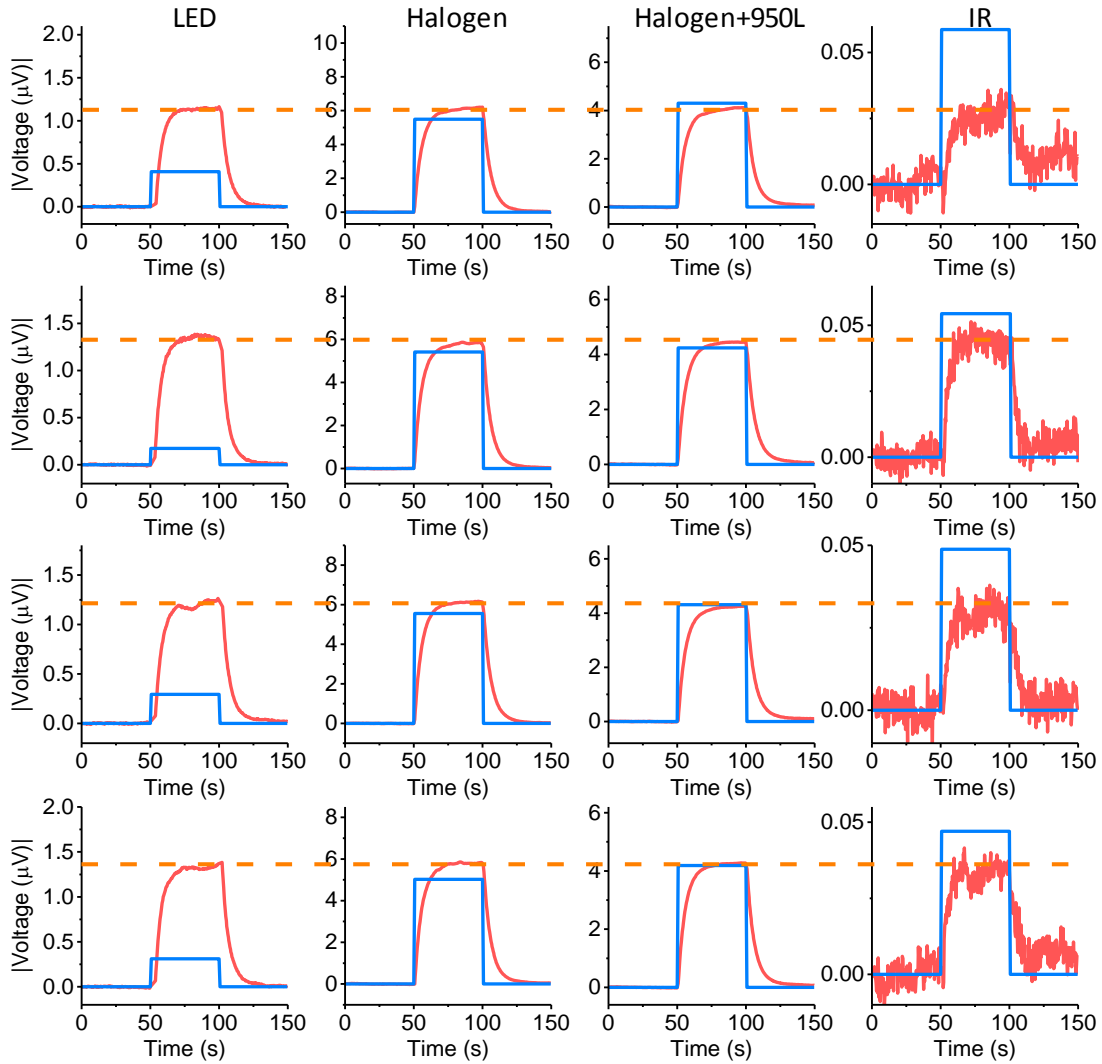


Figure 5.6 Comparison of PSV and SSE signals for Pd/YIG sample. The separated V_{PSV} and V_{SSE} signals are shown in blue and red, respectively, obtained from measurements with the light source shown on top. Each row is a different measurement instance. Between each measurement, the sample was removed and repositioned before repeating the data collection.

same format as for Figure 5.3. As shown by these repeated measurements, the results of these experiments are highly reproducible.

5.5.2 Impact of light incidence direction

All the previous data were measured with the sample placed on the Al heat sink with the NM side facing down (i.e. facing the heat sink) and the YIG side facing up (i.e. facing the light).

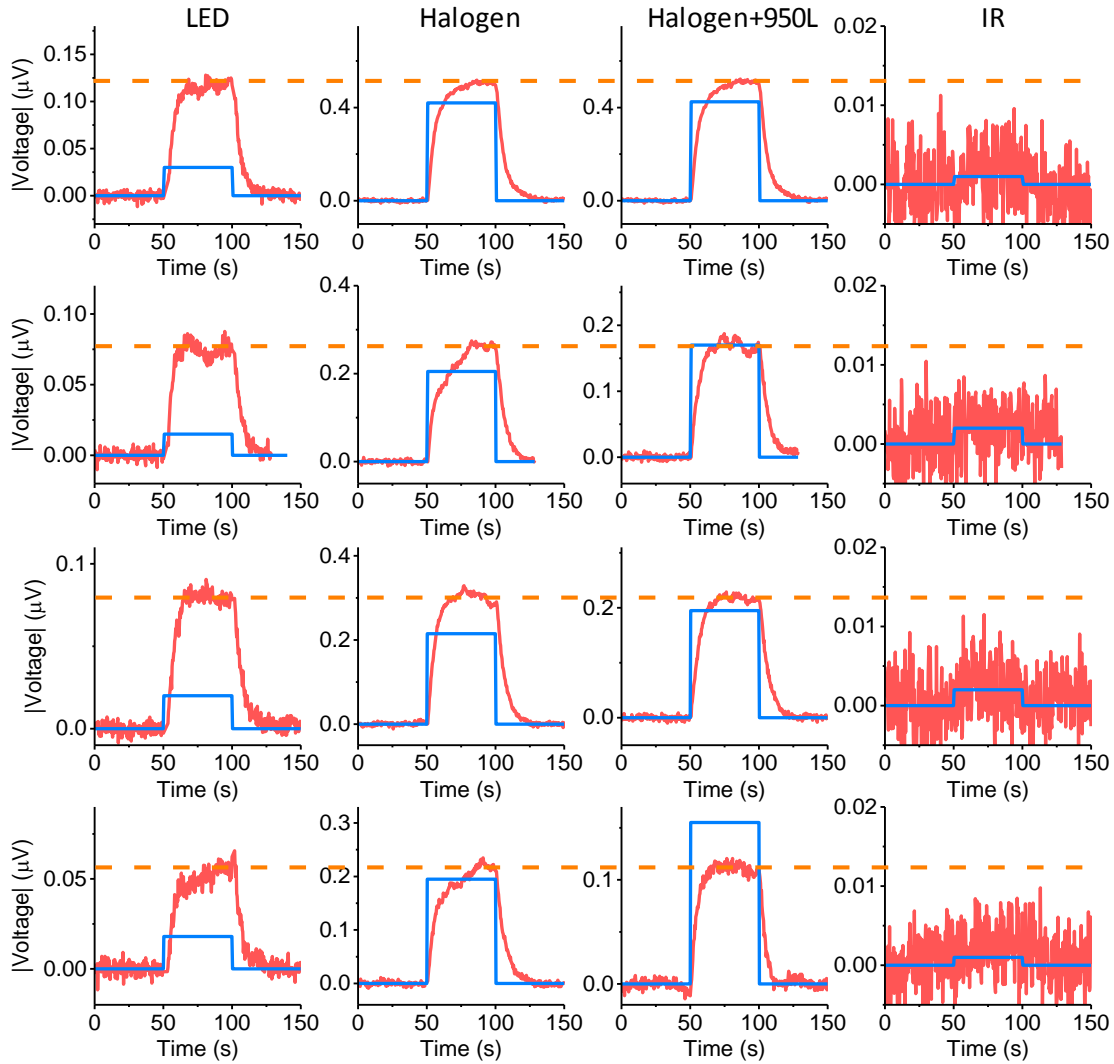


Figure 5.7 Comparison of PSV and SSE signals for Au/YIG sample. The separated V_{PSV} and V_{SSE} signals are shown in blue and red, respectively, obtained from measurements with the light source shown on top. Each row is a different measurement instance. Between each measurement, the sample was removed and repositioned before repeating the data collection.

In principle, one can also carry out the same measurements with the NM side facing up and the YIG side facing down. This light-sample configuration, however, is disadvantaged compared to the NM-side-down configuration for several reasons. First, the PSV signals for NM-side-up are weaker, as reported previously.⁶¹ This is probably because for this configuration the light reaches the NM/YIG interface with a lower intensity due to the fact that the NM layer, although thin, has a proportionally larger light absorption compared to the GGG and the YIG.⁶¹ Second, the SSE

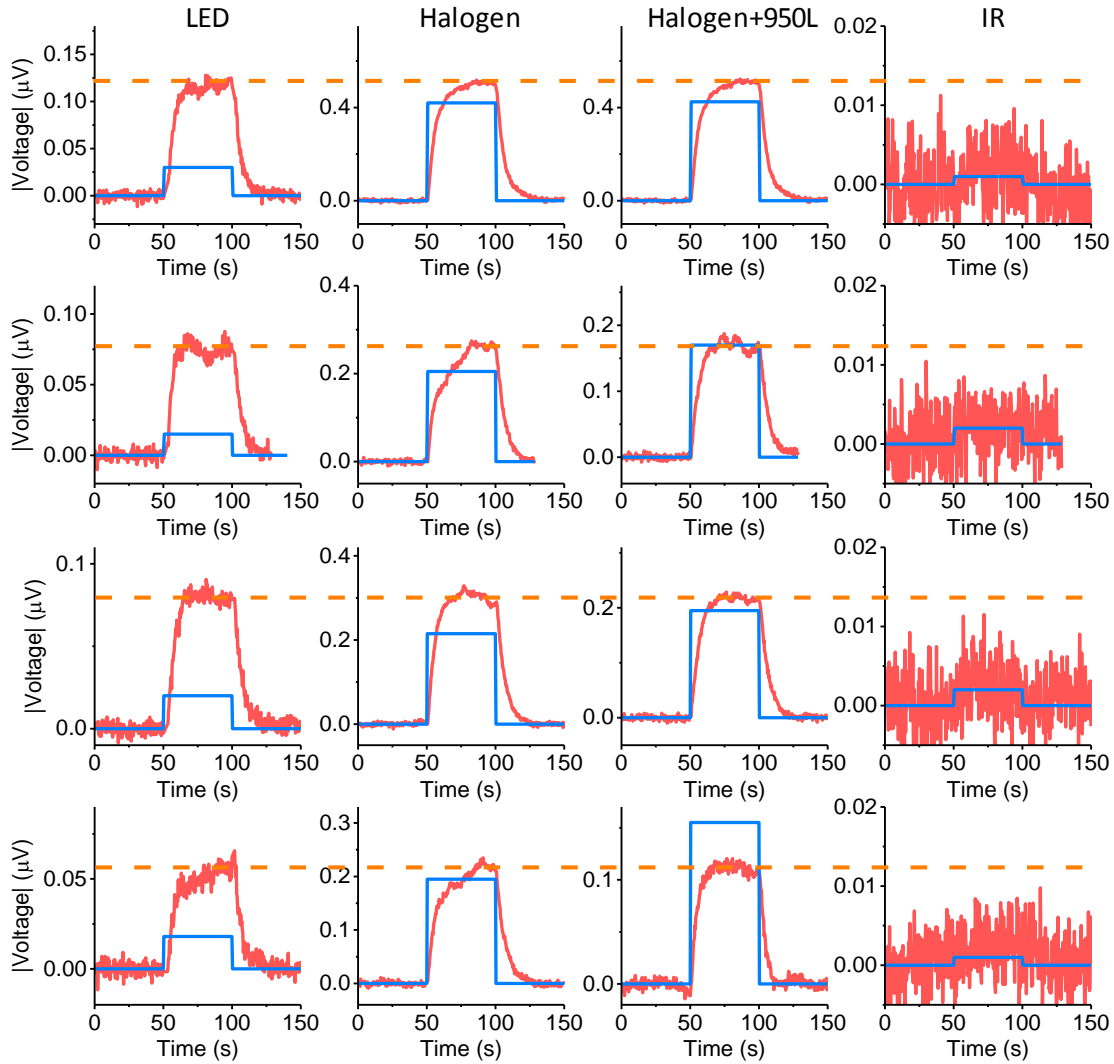


Figure 5.8 Comparison of PSV and SSE signals for Cr/YIG sample. The separated V_{PSV} and V_{SSE} signals are shown in blue and red, respectively, obtained from measurements with the light source shown on top. Each row is a different measurement instance. Between each measurement, the sample was removed and repositioned before repeating the data collection.

signals are stronger for the NM-side-down configuration, because the metal is in contact with the bottom heat sink and it is easier to establish a larger temperature gradient in the sample. Finally, when using the infrared light, the NM-side-up configuration does not yield any SSE signals, while the NM-side-down configuration does give a signal. Figure 5.9 shows the data when the Pd/YIG sample was placed Pd-side-up on the heat sink and measured. The comparison of the data in Figure 5.9 with those in Figure 5.3 provides clear justifications to the discussions above.

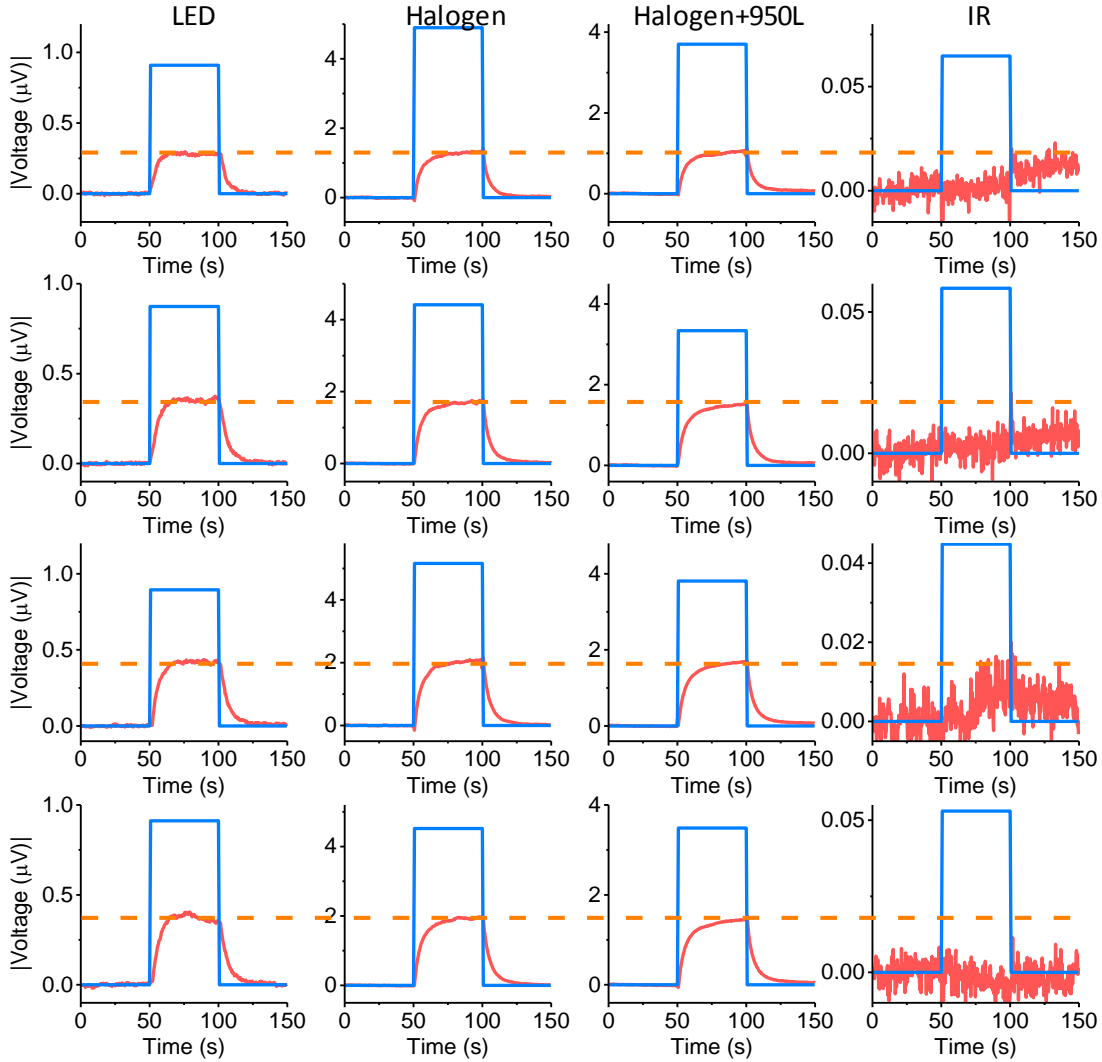


Figure 5.9 Comparison of PSV and SSE signals in the Pd/YIG sample using the Pd-side-up configuration. The separated V_{PSV} and V_{SSE} signals are shown in blue and red, respectively, obtained from measurements with the light source shown on top. Each row is a different measurement instance. Between each measurement, the sample was removed and repositioned before repeating the data collection.

5.5.3 Comparison of voltage sign in different metals

The previous measurements (from Figure 5.3 onward) have looked only at the absolute value of the PSV and SSE voltage signals. As seen in Figure 5.2 V_{PSV} and V_{SSE} have opposite signs. Furthermore, the sign of both V_{PSV} and V_{SSE} depends on the sign of the spin Hall angle, θ_{SH} , in the

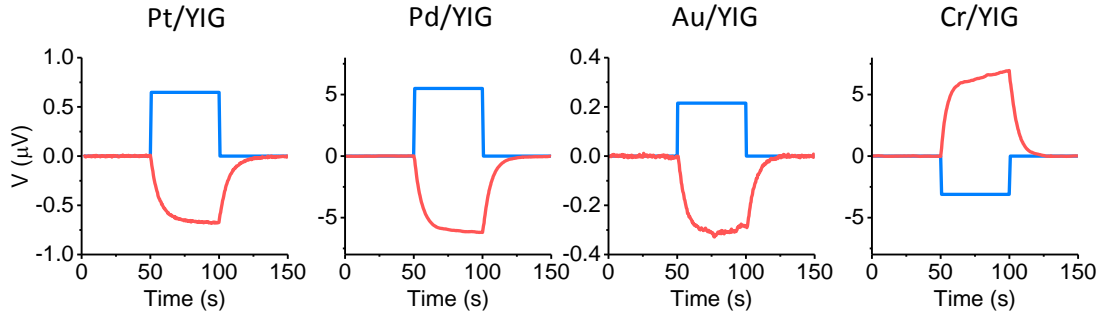


Figure 5.10 Comparison of PSV and SSE voltages. The separated V_{PSV} and V_{SSE} voltage signals are shown in blue and red, respectively, for four different samples, as labeled above the graphs. The data shown are for the halogen light source.

particular metal.^{85,93} For Pt, Pd, and Au the spin Hall angle is positive, while for Cr the spin Hall angle is negative. This means that the voltages measured from the Pt/YIG, Pd/YIG, and Au/YIG samples should share the same sign, while the Cr/YIG sample should have the opposite sign. This is indeed the case as shown in Figure 5.10.

5.5.4 Temperature measurements

In order to confirm the slow time response of the temperature gradient, and thus the SSE voltage signal, the temperature of the Pt was measured with two different methods simultaneously. The first method was by placing a type T thermocouple directly on the Pt surface. The second method was by measuring the change in voltage with a constant current applied. This voltage change is due to temperature dependence of the resistance in Pt.⁹⁴ Because the resistance of the nm-thick Pt films is rather large, around 1 k Ω , a Wheatstone bridge was used to measure the change in voltage.⁹⁵

A circuit diagram of the Wheatstone bridge is shown in Figure 5.11(a). A constant current of 10 μ A is applied to the electrical circuit. The resistors R_1 and R_2 have equal resistance and the variable resistor R_3 is tuned so that it has the same resistance as the Pt layer of the sample at room temperature in the absence of light illumination. The nanovoltmeter measures the bridge voltage,

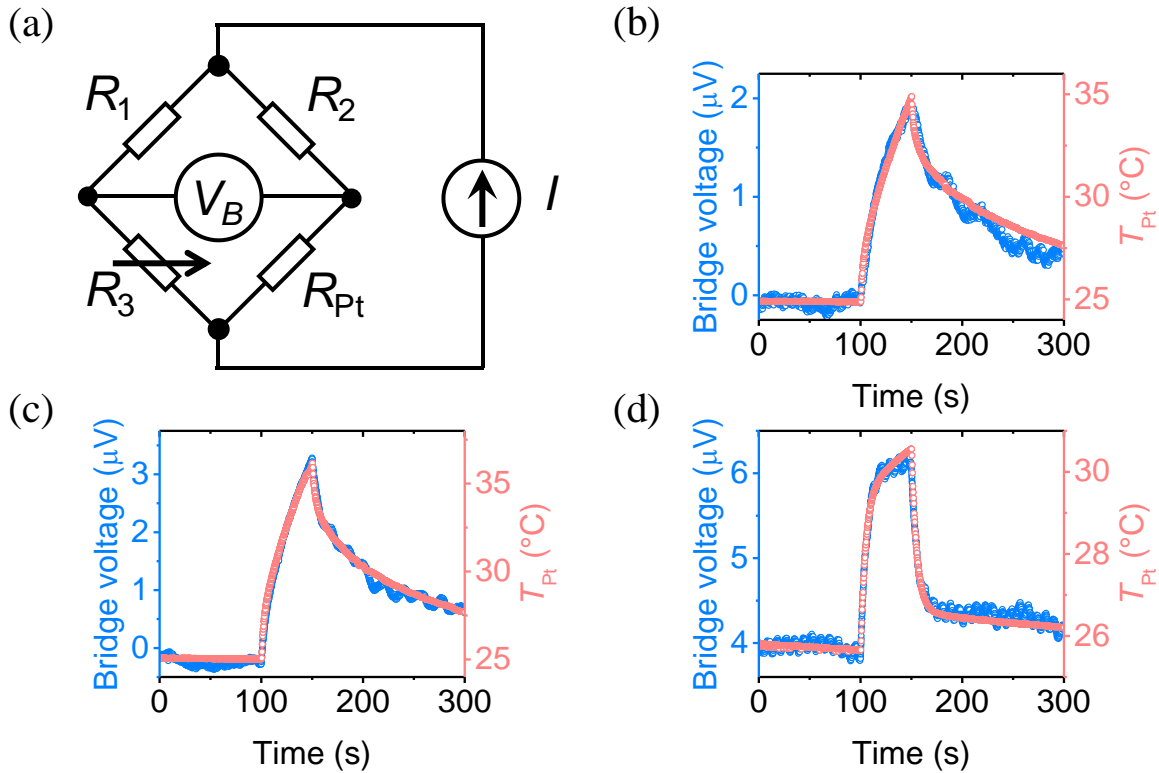


Figure 5.11 Pt temperature measurements. (a) Circuit diagram of the experimental setup. R_1 is equal to R_2 , and R_3 was tuned such that $R_3 = R_{Pt}$ at room temperature. The temperature of the Pt was measured via the change in V_B , due to the temperature dependence of the Pt resistance, (shown in blue) and direct thermocouple measurement (shown in red). The temperature response is demonstrated in three measurements: (a) Pt(3.5 nm)/YIG(10.4 μm)/GGG(0.5 mm), (b) Pt(3 nm)/YIG(40 nm)/GGG(0.5 mm), and (c) the same sample as (b) but was placed Pt-side-down on a heatsink. For all the measurements, the light was turned on at 100 s and off at 150 s.

V_B . When the circuit is properly tuned, one can have $V_B = 0$ at room temperature. When the sample heats up the resistance of the Pt layer changes and V_B is proportional to the change in resistance and therefore the change in the temperature of the Pt layer.

Figure 5.11 shows the results of three temperature measurements. Figure 5.11(b) shows the result for a Pt(3.5 nm)/YIG(10.4 μm)/GGG(0.5 mm) sample and Figure 5.11(c) shows the result for a (Pt 3 nm)/YIG(40 nm)/GGG(0.5 mm) sample. In Figure 5.11(b) and (c) the sample was set up in the same manner as in Ref. [61], except the sample was connected to the Wheatstone bridge

instead of directly to the nanovoltmeter. Figure 5.11(d) shows the data for the same sample as Figure 5.11(c), except it was placed Pt-side-down on a heatsink.

In each case the thermocouple-measured and voltage bridge-measured data change in response to the light activation in exactly the same manner, and this result is true for each of the three measurements. These data indicate that the previous temperature measurements, as seen in Chapter 4, are accurate. This means that the PSV signals, which show a fast time response, are not due to either bulk or interface SSE, which are due to thermal effects and show the same time domain response as the change in temperature of across the thickness of the sample, in the case of the bulk effect, or the temperature of the Pt layer, in the case of the interface effect. If the interfacial SSE was the reason for the fast increase in voltage which was observed a corresponding fast increase in the Pt temperature should also be measured.⁹⁶ A comparison of the time response of the voltage and temperature signals can be seen in Figure 4.2(d) and Figure 4.9. The PSV effect voltage and temperature signals have entirely different responses in the time domain. In the case where a temperature gradient is induced across the thickness of the sample, the voltage changes in the same manner as the temperature gradient, as would be expected for the SSE.

5.5.5 Optical properties of the samples

Figure 5.12 shows the light transmission of each sample, and its substrate without any metal, as a function of wavelength. Two points should be made for these data. First, despite the small amount of metal deposited there is a substantial change in transmission. Second, the absorption for the samples is relatively flat and there is also no significant spike in the absorption for any of the samples, which would indicate that the sample preferentially absorbs one particular wavelength of light. This means that the preferential absorption of one particular wavelength of

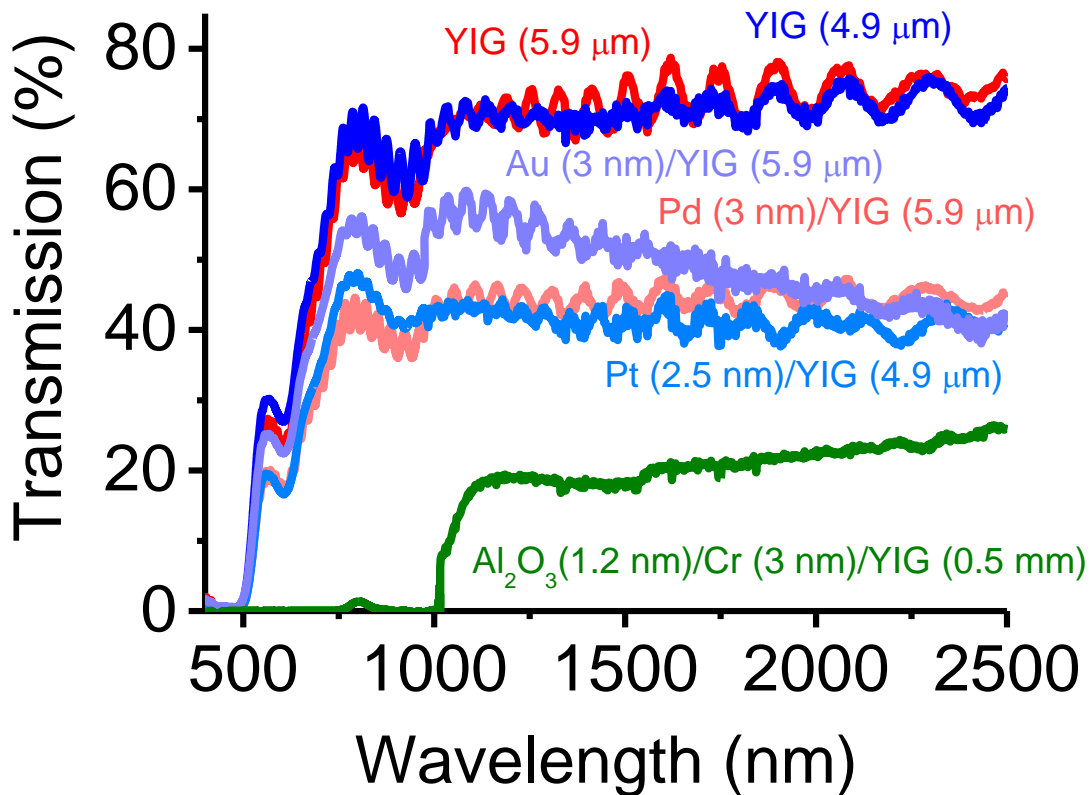


Figure 5.12 Optical transmission data for five samples.

light is not responsible for the voltage signal which is observed. The effect is instead due to spin-dependent excitation, which cannot be measured with a spectrometer.

5.6 Summary

This work demonstrates the distinction between the PSV effect and the SSE through the use of different light sources that cover the different portions of the optical spectrum. These results indicate the PSV effect has significantly different physical characteristics compared to the SSE. The voltage signal due to the PSV does not show the same time characteristic as the SSE induced voltage. The PSV voltage signal also shows a wavelength dependence different from the SSE. The results of this work also demonstrate the universal feature of the PSV effect through the use of

four NM/MI samples with four different NMs. Further, it is found that the trend of PSV strength in response to different light sources varies for different NMs. Future work is of great interest that utilizes monochromatic light sources with the same power to determine the specific wavelength dependence of the PSV and SSE effects in different samples. Note also that future experimental and theoretical studies that search for NM/MI systems with the strongest PSV effect is also very interesting.

CHAPTER 6 Ferromagnetic resonance

6.1 Introduction

Magnetization dynamics is a field with both a detailed history of research^{43,97-100} and currently relevant applications both on a fundamental scientific level¹⁰¹⁻¹⁰⁴ and in industry.¹⁰⁵⁻¹⁰⁹ Detailed knowledge of the dynamics of a magnetic system is critical for understanding both the physical mechanisms present in the system and optimizing device performance. For example, magnetization dynamics are of particular interest in the magnetic recording and memory industry.¹¹⁰⁻¹¹² In a hard drive, for example, information is stored in the magnetization of the material. When the information needs to be changed, the magnetization needs to be reversed. How the magnetization changes when this happens is of critical importance for optimizing device characteristics such as writing speed and power consumption.

One of the most widely used techniques to measure magnetization dynamics is ferromagnetic resonance (FMR). This flexible method gives insight into both dynamic properties of samples, such as damping and loss mechanisms, and the static magnetic properties, such as saturation induction and anisotropy fields. This chapter will introduce the fundamental dynamic motion of magnetization, precession, as well as how the FMR is measured and what the results of FMR measurements tell us about the system being measured.

6.2 Magnetization precession

6.2.1 Uniform motion

Uniform precessional motion is the simplest model for magnetization dynamics. The simple principles for uniform motion form the foundation for the FMR measurement technique.

6.2.1.1 Single electron dynamics

For most materials magnetism arises from the magnetic dipole moment of orbital electrons in transition metals.¹¹³ Due to the electric field of neighboring ions the orbital component of angular momentum is quenched. This leaves the spin angular momentum \mathbf{S} as the origin of the magnetic moment $\boldsymbol{\mu}$ given by

$$\boldsymbol{\mu} = -g \frac{e}{2m_e} \mathbf{S} = \gamma \mathbf{S} = -|\gamma| \mathbf{S} \quad 6.1$$

where γ is the gyromagnetic ratio which can be written as

$$\gamma = -g \frac{e}{2m_e} \quad 6.2$$

where g is the Landé g factor, e is the electron charge, and m_e is the electron mass. For a single electron the absolute value of the gyromagnetic ratio is 2.8 MHz/Oe. From Equation 6.1 and Figure 6.1(a), it is clear that the magnetic moment and spin angular momentum point in opposite directions.

In the presence of an external magnetic field, \mathbf{H} , a torque will be exerted on \mathbf{S} according to Newton's second law

$$\frac{d\mathbf{S}}{dt} = \boldsymbol{\mu} \times \mathbf{H} \quad 6.3$$

Plugging Equation 6.1 into Equation 6.3 the dynamics can be expressed in terms of $\boldsymbol{\mu}$ and \mathbf{H} only

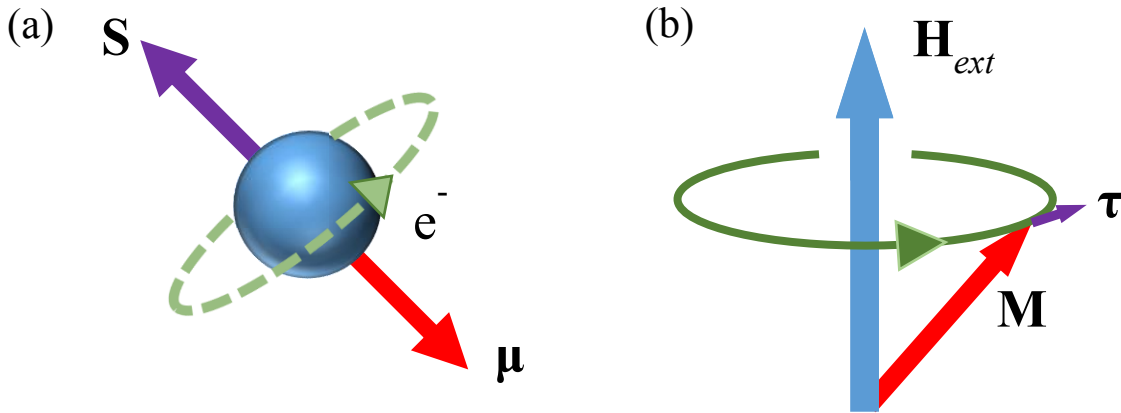


Figure 6.1 Schematic of precessional motion. (a) Precession of an electron with spin angular momentum \mathbf{S} and magnetic moment $\boldsymbol{\mu}$. (b) Precession of magnetization \mathbf{M} around an external field \mathbf{H}_{ext} due to torque $\boldsymbol{\tau}$.

$$\frac{d\boldsymbol{\mu}}{dt} = -|\gamma|\boldsymbol{\mu} \times \mathbf{H} \quad 6.4$$

Here, the gyromagnetic ratio and the strength of the magnetic field determine the frequency at which the moment precesses. This simple torque equation describes the precessional motion of a single electron spin in the presence of an external field.

6.2.1.2 Collective magnetization

Moving from a single spin to the collective magnetization of a material, the total magnetization of a material, \mathbf{M} , can be expressed as a sum of individual spins $\boldsymbol{\mu}$ in a volume V

$$\mathbf{M} = \sum \frac{\boldsymbol{\mu}}{V} \quad 6.5$$

When such a collection of spins is placed in an external magnetic field \mathbf{H} the system will attempt to align such that its potential energy

$$E = -\mathbf{M} \cdot \mathbf{H} \quad 6.6$$

is a minimum. When the system is not at an energy minimum, in other words when the magnetization and field are not aligned, the magnetization will experience a torque which will cause it to precess around the external field. In a simple lossless system, this torque is given by

$$\frac{d\mathbf{M}}{dt} = -|\gamma|\mathbf{M}\times\mathbf{H} \quad 6.7$$

in analogy to Equation 6.4. This precession is shown schematically in Figure 6.1(b).

6.2.2 Modifications to the torque equation

From this simple system, additional factors can be introduced to more closely approximate real experimental systems. In this subsection, the effects of finite size, anisotropy, and loss will be considered.

6.2.2.1 Demagnetization field

In a sample with finite size there will be a demagnetization field, \mathbf{H}_{dem} , which creates one or more preferred axes in non-spherical samples and changes the effective field felt by the magnetization in all cases. The demagnetization field can be expressed in terms of a 3×3 demagnetization tensor \mathbf{N} where

$$\mathbf{N} = \begin{pmatrix} N_x & 0 & 0 \\ 0 & N_y & 0 \\ 0 & 0 & N_z \end{pmatrix} \quad 6.8$$

and $N_x + N_y + N_z = 1$. The demagnetization field can then be written as

$$\mathbf{H}_{dem} = -4\pi\mathbf{N} \cdot \mathbf{M} \quad 6.9$$

In this subsection only the thin film geometry will be considered, that is, where the in-plane dimensions are much greater than the sample thickness and may be considered as infinite, thus only the component of \mathbf{N} is entirely along the film normal is nonzero. Two common situations are illustrated in Figure 6.2, that of field out of plane, $N_z = 1$, and field in plane, $N_x = 1$.

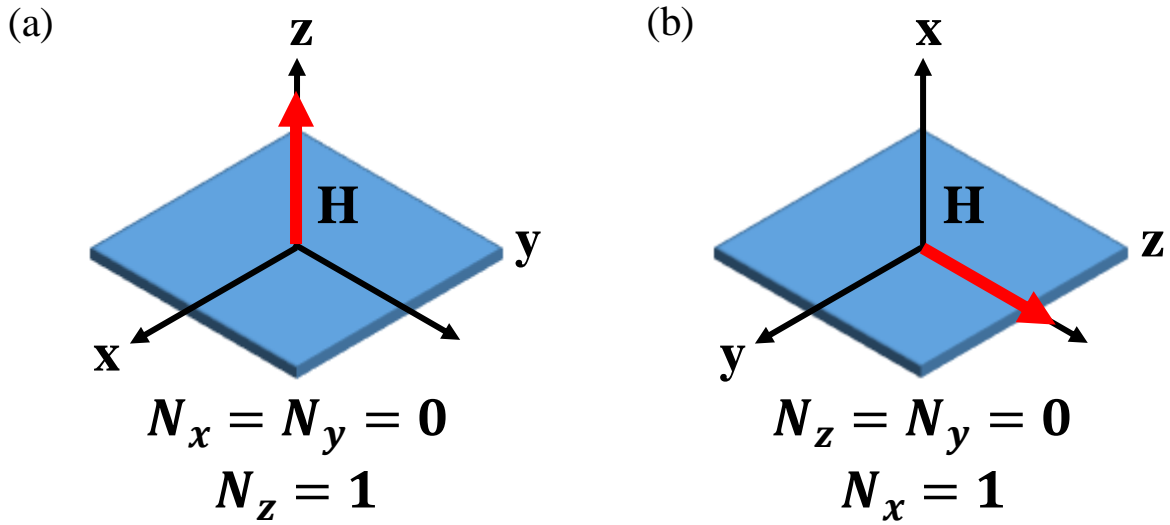


Figure 6.2 Components of the demagnetization tensor. Two common situations are illustrated: (a) external field out of the film plane and (b) external field in the film plane. The components of the demagnetization tensor, Equation 6.8, are shown for each case.

6.2.2.2 Uniaxial anisotropy

Next, an isotropic system is analyzed. Including anisotropy in the system is a concession to the dependence of the energy of the magnetic system on the orientation of the crystal lattice in some materials. The result of this is a preference for the magnetization to lie along certain crystal axes. In the case of uniaxial anisotropy, considered below, this is the easy axis. There exist more complicated systems which may have multiple easy axes or easy planes, which are an extension of this principle, but will not be discussed here.

For a sample with uniaxial anisotropy along the z -axis the magnetization will experience an effective anisotropy field, $H_u \hat{z}$, of the form

$$H_u \hat{z} = H_a \cos \theta_M \hat{z} \quad 6.10$$

where θ_M is the magnetization angle from the z axis, $H_a = 2K/M_s$ and K is the anisotropy constant.

6.2.2.3 Loss and damping

No experimental system can completely avoid loss, and many methods of incorporating loss into the torque equation have been studied over the years.^{9,49,97,114-118} The most widely used method is the Gilbert damping model which adds a phenomenological damping term to Equation 6.7 as shown here

$$\frac{d\mathbf{M}}{dt} = -|\gamma|\mathbf{M}\times\mathbf{H} + \frac{\alpha}{M_s}\mathbf{M}\times\frac{d\mathbf{M}}{dt} \quad 6.11$$

where α is the Gilbert damping constant which is proportional to the rate at which the precessing magnetization loses energy. This damping constant is one of the most important results from FMR measurements as it is closely related to the characteristic time scales for magnetization dynamics as well as the amount of energy required to change or reverse the magnetization direction.⁴⁹

6.2.3 Torque equation solution

The results of considering both the demagnetization field and the anisotropy field is a change in both the direction and magnitude of the total magnetic field the precessing magnetization experiences. This new effective field can be written as a sum of the different field components

$$\mathbf{H}_{eff} = \mathbf{H}_{ext} + \mathbf{H}_{dem} + \mathbf{H}_u \quad 6.12$$

To obtain a solution, one can substitute this new \mathbf{H}_{eff} into Equation 6.7 and solve the differential equation

$$\frac{d\mathbf{M}}{dt} = -|\gamma|\mathbf{M}\times\mathbf{H}_{eff} \quad 6.13$$

A solution is assumed of the following form

$$\mathbf{m}(t) = m_{0x}e^{i\omega t}\hat{\mathbf{x}} + m_{0y}e^{i\omega t}\hat{\mathbf{y}} \quad 6.14$$

In the discussion below, a small angle precession is assumed such that both m_{0x} and m_{0y} are much smaller than M_s . Because m_{0x} and m_{0y} are small, terms beyond first order in m_{0x} or m_{0y} are ignored. The terms of Equation 6.13 can be explicitly written for $\mathbf{H}_{ext} = H_0 \hat{\mathbf{z}}$ starting with the derivative of magnetization

$$\frac{d\mathbf{M}}{dt} = i\omega \begin{pmatrix} m_{0x} \\ m_{0y} \\ 0 \end{pmatrix} e^{i\omega t} \quad 6.15$$

Next, the cross product is evaluated using Equation 6.9 for demagnetization field and neglecting anisotropy

$$\mathbf{M} \times \mathbf{H}_{eff} = \begin{pmatrix} (H_0 + 4\pi M_s(N_y - N_z))m_{0y} \\ -(H_0 + 4\pi M_s(N_x - N_z))m_{0x} \\ 0 \end{pmatrix} e^{i\omega t} \quad 6.16$$

The stiffness fields, H_x and H_y , are defined as

$$\begin{aligned} H_x &= H_0 + 4\pi M_s(N_y - N_z) \\ H_y &= H_0 + 4\pi M_s(N_x - N_z) \end{aligned} \quad 6.17$$

and stiffness frequencies, ω_x and ω_y , are defined as

$$\begin{aligned} \omega_x &= |\gamma|H_x \\ \omega_y &= |\gamma|H_y \end{aligned} \quad 6.18$$

thus, the torque equation can be written as

$$i\omega \begin{pmatrix} m_{0x} \\ m_{0y} \\ 0 \end{pmatrix} = \begin{pmatrix} -\omega_y m_y \\ \omega_x m_x \\ 0 \end{pmatrix} \quad 6.19$$

In order for this set of equations to have nonzero solutions, it is necessary that $\omega^2 = \omega_x \omega_y$. The final solution for the precession frequency, known as the Kittel equation⁶², is

$$\omega = |\gamma| \sqrt{[H_{ext} + 4\pi M_s(N_x - N_z)][H_{ext} + 4\pi M_s(N_y - N_z)]} \quad 6.20$$

For the two common sample orientation cases illustrated in Figure 6.2, Equation 6.20 simplifies to

$$\omega = |\gamma|(H_{ext} - 4\pi M_s) \quad 6.21$$

for field out of plane and

$$\omega = |\gamma|\sqrt{H_{ext}(H_{ext} + 4\pi M_s)} \quad 6.22$$

for field in plane.

6.3 Ferromagnetic resonance

In order to compensate loss an AC magnetic field can be applied perpendicular to the static bias field and may be thus used to drive the magnetization precession. When the microwave frequency is the same as the magnetization precession frequency, given by Equation 6.20, the system is at resonance and maximum power is transferred from the microwave to the sample. This situation is FMR, and by examining the microwave power absorption profile the collective behavior of the sample can be characterized.

There are two common methods for generating FMR profiles, field-swept and frequency-swept. In the field-swept case a microwave magnetic field of a fixed frequency is used to excite the sample, the static magnetic field is then swept near the resonance field. The opposite situation occurs for frequency-swept; a fixed static magnetic field is applied and the microwave frequency is swept near the resonance frequency. In the discussions below only the field-swept case is considered.

The Gilbert equation can be modified to include a time varying magnetic field such that $\mathbf{H}_{ext} = \mathbf{h}(t) + H_0\hat{\mathbf{z}}$ where

$$\mathbf{h}(t) = h_{0x}e^{i\omega t}\hat{\mathbf{x}} + h_{0y}e^{i\omega t}\hat{\mathbf{y}} \quad 6.23$$

Following the same procedure as with Equation 6.13, a solution to Equation 6.11 can be obtained

$$\begin{pmatrix} i\omega m_{0x} + \omega_y m_{0y} - \alpha i\omega m_{0y} \\ i\omega m_{0y} - \omega_x m_{0x} + \alpha i\omega m_{0x} \\ 0 \end{pmatrix} = \begin{pmatrix} |\gamma| M_s h_{0y} \\ -|\gamma| M_s h_{0x} \\ 0 \end{pmatrix} \quad 6.24$$

This solution can be written in the form $\mathbf{m} = \chi \cdot \mathbf{h}$ where χ is the susceptibility tensor. For uniform precession, this takes the form

$$\begin{pmatrix} m_{0x} \\ m_{0y} \end{pmatrix} = 4\pi \begin{pmatrix} \chi_{xx} & -i\kappa \\ i\kappa & \chi_{yy} \end{pmatrix} \begin{pmatrix} h_{0x} \\ h_{0y} \end{pmatrix} \quad 6.25$$

The elements of the susceptibility tensor will be given below. The expression for m_{0x} and m_{0y} can be written as below, neglecting terms second order in α

$$m_{0x} = \frac{\omega_M(\omega_y h_{0x} + i\alpha\omega h_{0x} - ih_{0y})}{\omega_x\omega_y + i\alpha\omega(\omega_x + \omega_y) - \omega^2} \quad 6.26$$

$$m_{0y} = \frac{\omega_M(\omega_x h_{0y} + i\alpha\omega h_{0y} - ih_{0x})}{\omega_x\omega_y + i\alpha\omega(\omega_x + \omega_y) - \omega^2}$$

where $\omega_M = |\gamma|4\pi M_s$. It is then straightforward to write down the susceptibility tensor coefficients

$$\chi_{xx} = \frac{\omega_M(\omega_y + i\alpha\omega)}{\omega_x\omega_y + i\alpha\omega(\omega_x + \omega_y) - \omega^2}$$

$$\chi_{yy} = \frac{\omega_M(\omega_x + i\alpha\omega)}{\omega_x\omega_y + i\alpha\omega(\omega_x + \omega_y) - \omega^2} \quad 6.27$$

$$\kappa = \frac{\omega_M\omega}{\omega_x\omega_y + i\alpha\omega(\omega_x + \omega_y) - \omega^2}$$

Note that each of these coefficients is complex. This has an important physical consequence. The real part of χ is governed by the dispersive properties of the material, while the

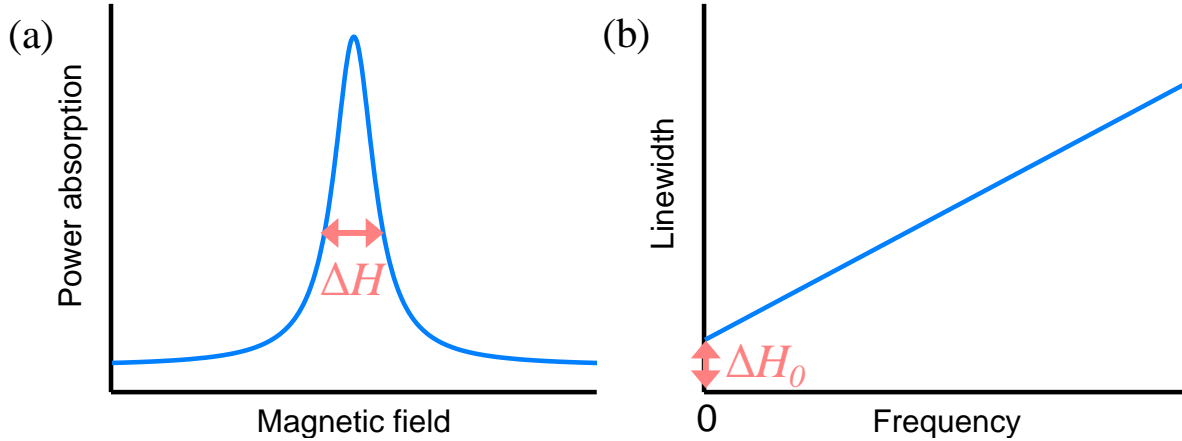


Figure 6.3 Schematic of ferromagnetic resonance absorption. (a) Diagram of Lorentzian FMR power absorption profile at a fixed microwave frequency as a function of the external static field showing FMR linewidth ΔH . (b) Diagram of FMR linewidth as a function of microwave frequency, including inhomogeneous line broadening (ILB) ΔH_{ILB} .

imaginary part of χ is connected to the microwave loss in the material. This property leads to the finite linewidth of the power absorption profile measured in FMR, as seen in Figure 6.3(a). The peak-to-peak FMR linewidth is given by the following expression

$$\Delta H_{FMR} = \Delta H_{ILB} + \frac{2\alpha}{\sqrt{3}|\gamma|} \frac{\omega}{2\pi} \quad 6.28$$

The factor of $\sqrt{3}$ is due to using the peak-to-peak linewidth. If using the full width at half maximum linewidth it should be omitted. The term ΔH_{ILB} is the inhomogeneous line broadening (ILB), a zero-frequency line broadening due to spatial variations in the saturation magnetization, anisotropy, external magnetic field, or other experimental parameters. The linear dependence on frequency can be seen in Figure 6.3(b), as well as the contribution from inhomogeneous line broadening at zero frequency.

6.4 Shorted waveguide and cavity FMR

One of the most common techniques for measuring FMR is using rectangular air-filled waveguides terminated in a short or microwave cavity.⁴³ In a shorted waveguide measurement, the sample is placed at the end of the waveguide on top of the short. A microwave magnetic field with constant frequency, generated by a microwave generator, is applied to the sample. The microwaves reflect off the short and are redirected by a circulator to a microwave diode which is connected to a measurement device, either a voltmeter or lock-in amplifier. An external DC bias field, \mathbf{H} , is applied and swept for FMR measurements. In order to increase the measurement sensitivity and eliminate any DC bias, a weak low-frequency AC field, $\mathbf{h}_{\text{mod}}(t)$, is added parallel to the external field. This modulation field frequency, typically on the order of tens of Hz, is linked to a lock-in amplifier. The modulated signal coming from the diode is passed through a high-pass filter and is then measured by the lock-in amplifier. A schematic of this measurement setup is shown in Figure 6.4(a).

Due to the use of the lock-in amplifier, the measurement output is a Lorentzian derivative, instead of the Lorentzian profile shown in Figure 6.3(a). Sample data taken at 13 GHz for a 46-nm-thick YIG film sample is presented in Figure 6.4(b) as blue circles. The data are fit with a Lorentzian derivative trial function, illustrated by the red dashed line, and two important parameters are extracted for further analysis: the resonance field, 3949 Oe, indicated by the green dashed line, and the peak-to-peak linewidth, 6 Oe, indicated by the purple dashed lines. By repeating the FMR measurements at different microwave frequencies the resonance fields can be used with Equation 6.20 to determine the $4\pi M_s$ or anisotropy field, and linewidth can be used with Equation 6.28 to determine the damping and inhomogeneous line broadening.

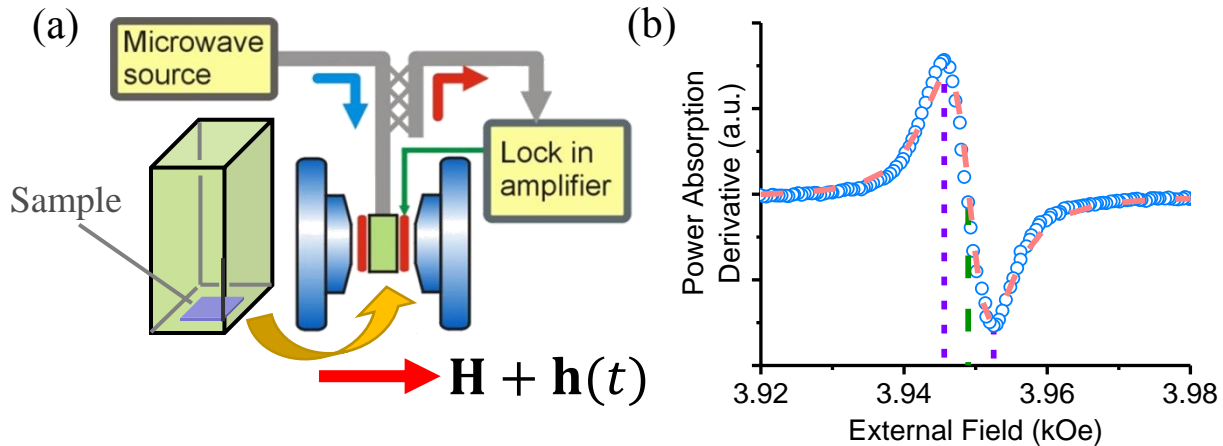


Figure 6.4 Shorted waveguide FMR measurement technique. (a) Diagram of the shorted waveguide measurement system. (b) Sample FMR profile measured in a shorted waveguide. The blue circles are measurement data. The red dashed curve is a fit of a Lorentzian derivative function. The green dashed line indicates the resonance field and the purple dashed lines show the peak-to-peak linewidth.

Experimentally, shorted waveguides are convenient to use because they support propagating microwaves in a band of frequencies defined by the waveguide's dimensions.¹¹⁹ This makes it easy to perform multiple measurements at the different frequencies required for damping analyses, for example. However, for some samples, such as ultra-thin films or films with very large FMR linewidth, the signal-to-noise ratio is too low to measure a clear signal, even with field modulation and lock-in detection. In this case, a microwave cavity may be used. Microwave cavities have much higher signal-to-noise ratios compared to shorted waveguides. They, however, only operate at one frequency defined by the dimensions of the cavity.¹¹⁹ Thus, in order to perform frequency-dependent analyses, multiple microwave cavities with different operating frequencies must be used.

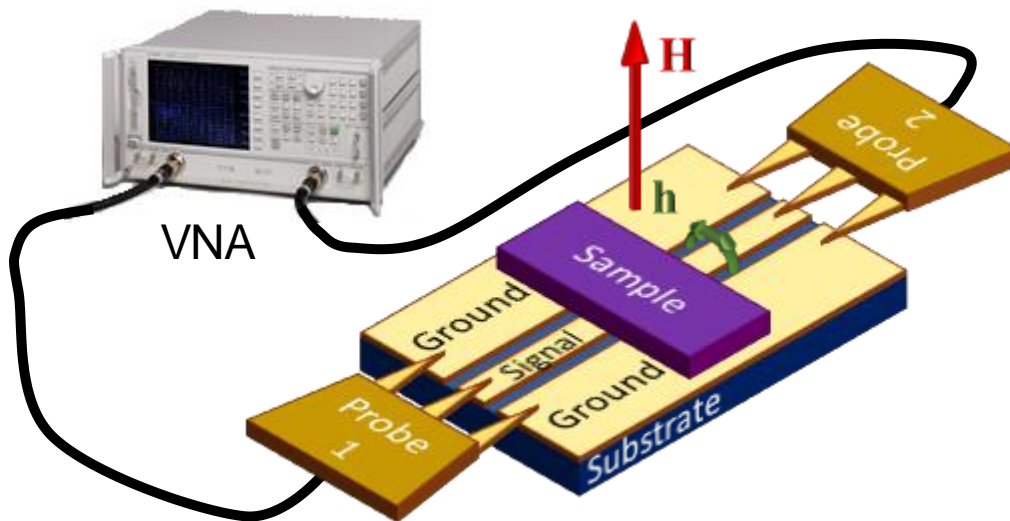


Figure 6.5 Schematic of VNA-FMR measurement technique. The VNA is connected to two ground-signal-ground RF probes, shown in brown, which are connected to the coplanar waveguide. The generated RF microwave field is shown in green and the perpendicular external DC magnetic field is shown in red. The sample is placed on top of the coplanar waveguide with the magnetic film facing the waveguide.

6.5 Vector network analyzer ferromagnetic resonance

One FMR measurement method which has both a broad frequency range and a high signal-to-noise ratio is the so-called vector network analyzer FMR (VNA-FMR) technique.^{43,120-122} Instead of using air-filled rectangular waveguides this system uses a coplanar waveguide (CPW) connected to a vector network analyzer (VNA). The coplanar waveguide with the VNA is capable of measuring over a wide range of microwave frequencies with high sensitivity.

A schematic of the experimental setup is shown in Figure 6.5. A VNA is connected to two ground-signal-ground high-frequency microwave probes via low-noise low-loss high-frequency RF cables. The probes are mounted on precision translation stages which are used to align the probes with the coplanar waveguide. For the measurement data presented below, the waveguides

are made of 250-nm-thick Au films deposited on a-plane sapphire substrates. The waveguide structures were made by photolithography. The waveguide is 6.5 mm in length with a central conductor which is 100 μm wide and ground planes which are 300 μm wide. The gaps between the signal line and the ground planes are 50 μm . The characteristic impedance of the waveguide is designed to be 50 Ω to match with the rest of the microwave circuit.

The sample is placed over the CPW with the magnetic film facing the CPW. For metallic samples, a layer of Shipley Microposit S1813 photoresist is spin coated at 4000 rpm for 30 seconds onto the sample, which results in a layer thickness which is about 1.5 μm . This is to avoid shorting the ground planes to the signal line. An external static magnetic field is applied out of plane. By adjusting the separation between the magnet pole pieces a maximum magnetic field of up to 20 kOe can be applied. The field strength is measured with a Hall probe. The VNA generates an RF current, with a frequency range of 10 MHz to 67 GHz, in the signal line of the waveguide, and this creates an oscillating magnetic field which couples to the sample.¹²³ The VNA then measures both the real and imaginary parts of the complex transmission coefficient, the scattering parameter S_{21} .¹²⁴ A LabView program controls the VNA and magnet power supply outputs, and collects data from the VNA and the Hall probe to generate field-swept FMR measurements. In order to increase the signal-to-noise ratio, the individual field-swept measurements are averaged. Typically, around 30 averages are used, depending on the level of signal for a particular sample.

A set of exemplary VNA-FMR data are shown in Figure 6.6. The sample measured for this data set is a 2-nm-thick CoFeB film sample. Because this sample is conducting, a 1.5- μm -thick layer of photoresist was added to insulate the sample from the waveguide. The data were taken at a fixed frequency of 17 GHz. Figure 6.6(a) shows the real part of S_{21} , while Figure 6.6(b) shows

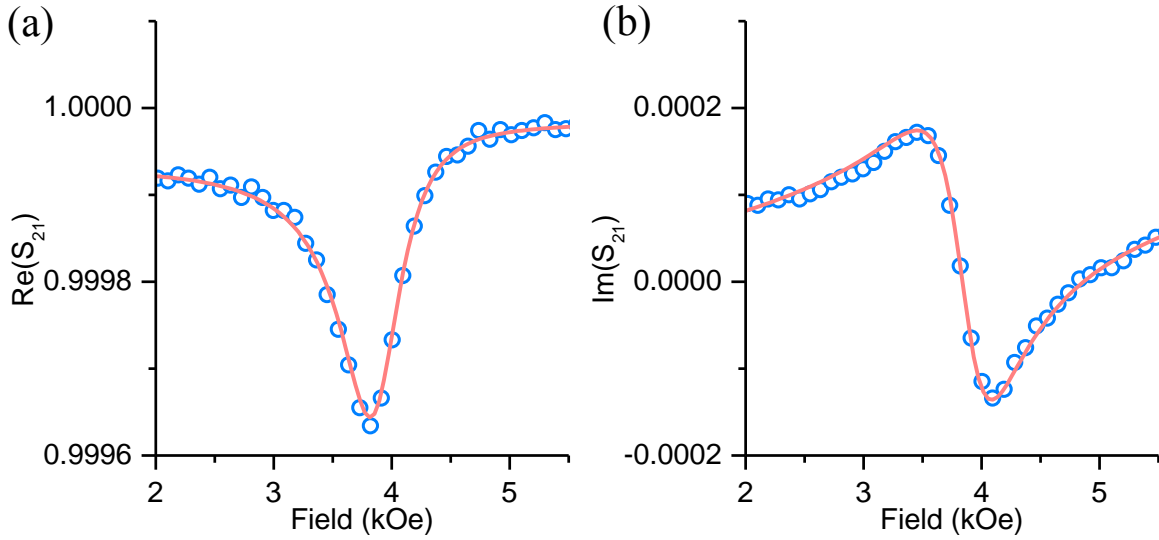


Figure 6.6 Example VNA-FMR data. (a) Real and (b) Imaginary parts of S_{21} as a function of external magnetic field. The blue circles are the data and the red curve is a fit described in Section 6.5.2.

the imaginary part. The blue circles represent the data collected by the VNA, and the red curves are the fits. The fitting method is discussed in the next subsection.

6.5.1 Susceptibility in terms of S-parameters

The VNA measures microwave transmission in terms of the complex transmission coefficient, S_{21} . In order to extract the damping and other magnetic information about the sample from the S_{21} data, there must be a method for relating S_{21} to the magnetic parameters discussed earlier in this chapter.¹²⁵

When a magnetic film is placed on a CPW, it changes the effective impedance of the CPW. This change in impedance is correlated to the excitations happening in the magnetic film. This can be expressed as a perturbation to the scattering parameters

$$\begin{aligned}
 S_{11} &= S_{11}^0 + \Delta S_{11} \\
 S_{21} &= S_{21}^0 + \Delta S_{21}
 \end{aligned}
 \tag{6.29}$$

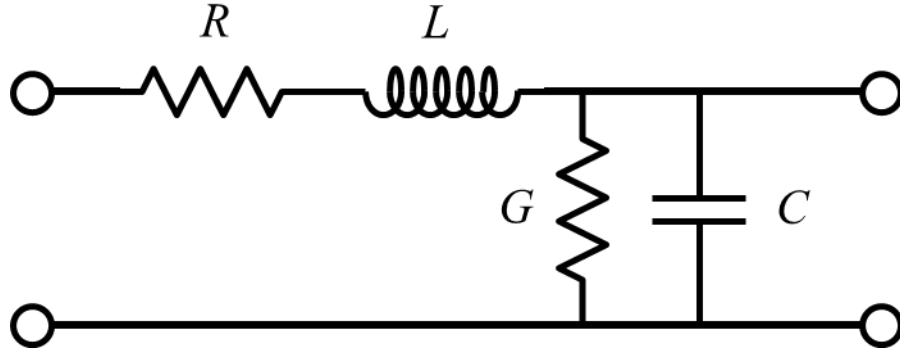


Figure 6.7 Schematic diagram of effective CPW-sample lumped circuit element. R is the series resistance, L is the inductance, G is the shunt conductance, and C is the capacitance.

where S^0 and ΔS are the non-magnetic and magnetic contributions, respectively. The CPW-sample system can be considered as a lumped circuit element with effective series resistance R , inductance L , shunt conductance G , and capacitance C , as shown in Figure 6.7. The reflection, S_{11} , and transmission, S_{21} , coefficients can be written as¹²⁶

$$S_{11} = \frac{i\omega L + R + \frac{Z_0}{1 + Z_0(G + i\omega C)} - Z_0}{i\omega L + R + \frac{Z_0}{1 + Z_0(G + i\omega C)} + Z_0} \quad 6.30$$

$$S_{21} = \frac{\frac{2Z_0}{1 + Z_0(G + i\omega C)}}{i\omega L + R + \frac{Z_0}{1 + Z_0(G + i\omega C)} + Z_0}$$

where Z_0 is the characteristic impedance of the CPW. Equation 6.30 can be solved to obtain

$$i\omega L = \frac{1 + S_{11} - S_{21}}{1 - S_{11}} Z_0 - R \quad 6.31$$

The inductance can be rewritten in terms of L_0 , the self-inductance of the CPW; a geometry factor, c , with dimensions of m^{-1} ; the length of the sample, l ; the thickness of the magnetic film, t ; the relative susceptibility which is approximately equal to the relative permeability, $\chi \approx \mu$; and the permeability of free space, μ_0

$$L \approx L_0 + clt\chi\mu_0 \quad 6.32$$

An expression for the susceptibility can now be written in terms of the scattering matrix parameters

$$\chi = \frac{Z_0 \left(\frac{1 + S_{11} - S_{21}}{1 - S_{11}} - \frac{1 + S_{11}^0 - S_{21}^0}{1 - S_{11}^0} \right)}{icl t \mu_0 \omega} \quad 6.33$$

In the limit of weak reflection of microwave power from the sample (i.e. $|S_{11}| \ll 1$), the susceptibility can be reduced to

$$\chi \cong \chi_0 [(2 + 2S_{11}^0 - S_{21}^0)\Delta S_{11} - (1 + S_{11}^0)\Delta S_{21}] \quad 6.34$$

where χ_0 is a phenomenological parameter incorporating the experimental constants. In the quasi-static limit $\Delta S_{11} = -\Delta S_{21}$,¹²⁰ and Equation 6.34 can be further reduced to

$$\chi \cong -\chi_0 (3(1 + S_{11}^0) - S_{21}^0)\Delta S_{21} \quad 6.35$$

In the limit of perfect transmission when the system is far for magnetic excitation, that is when $S_{11}^0 = 0$ and $S_{21}^0 = 1$, a final simplification can be achieved

$$\chi \cong -2\chi_0\Delta S_{21} \quad 6.36$$

Equation 6.29 can now be written as

$$S_{21} = S_{21}^0 - \frac{\chi}{\chi_0} = S_{21,R}^0 + S_{21,I}^0 - \text{Re}\left(\frac{\chi}{\chi_0}\right) - \text{Im}\left(\frac{\chi}{\chi_0}\right) \quad 6.37$$

where $S_{21,R}^0$ and $S_{21,I}^0$ are the real and imaginary parts of S_{21}^0 . If Equation 6.27 is substituted for χ , S_{21} can be written fully in terms of the film's magnetostatic properties, the external field, the demagnetization field, and the damping parameter.

6.5.2 Fitting of experimental data

The data shown in Figure 6.6 can now be fit by combining Equations 6.27 and 6.37; however, note that for generic complex functions a and b

$$\operatorname{Re}\left(\frac{a}{b}\right) \neq \frac{\operatorname{Re}(a)}{\operatorname{Re}(b)} \quad 6.38$$

Thus, the real and imaginary parts of S_{21} are not independent and fitting of the real and imaginary parts of S_{21} must be done simultaneously using the same fitting parameters.

For the out-of-plane field configuration, because of $\chi_{xx} = \chi_{yy} = \chi$ we can write Equation 6.27 as

$$\chi = \frac{|\gamma|4\pi M_s(|\gamma|(H + M_{eff}) + i\alpha\omega)}{|\gamma|^2(H + M_{eff})^2 - \omega^2 + 2i\alpha\omega|\gamma|(H + M_{eff})} \quad 6.39$$

where $M_{eff} = H_k - 4\pi M_s$ accounts for the perpendicular anisotropy field of the film, H_k . The real part of Equation 6.37 can be written as

$$\begin{aligned} S_{21,R} &= S_{21,R}^0 + D_R H \\ &+ \frac{4\pi M_s \left\{ \begin{aligned} &\left[\chi_{0,R}(H + M_{eff}) + \chi_{0,I} \frac{\Delta H}{2} \right] \left[(H + M_{eff})^2 - \left(\frac{\omega}{\gamma}\right)^2 \right] + \\ &\left[\chi_{0,I}(H + M_{eff}) - \chi_{0,R} \frac{\Delta H}{2} \right] \left[\Delta H \frac{\omega}{|\gamma|} \right] \end{aligned} \right\}}{(\chi_{0,R}^2 + \chi_{0,I}^2) \left\{ \left[(H + M_{eff})^2 - \left(\frac{\omega}{\gamma}\right)^2 \right]^2 + \left[\Delta H \frac{\omega}{\gamma} \right]^2 \right\}} \end{aligned} \quad 6.40$$

and the imaginary as

$$\begin{aligned}
S_{21,I} &= S_{21,I}^0 + D_I H \\
&+ \frac{4\pi M_s \left\{ \begin{aligned} &\left[\chi_{0,I}(H + M_{eff}) - \chi_{0,R} \frac{\Delta H}{2} \right] \left[(H + M_{eff})^2 - \left(\frac{\omega}{\gamma} \right)^2 \right] - \\ &\left[\chi_{0,R}(H + M_{eff}) + \chi_{0,I} \frac{\Delta H}{2} \right] \left[\Delta H \frac{\omega}{|\gamma|} \right] \end{aligned} \right\}}{(\chi_{0,R}^2 + \chi_{0,I}^2) \left\{ \left[(H + M_{eff})^2 - \left(\frac{\omega}{\gamma} \right)^2 \right]^2 + \left[\Delta H \frac{\omega}{\gamma} \right]^2 \right\}} \quad 6.41
\end{aligned}$$

where subscripts R and I denote the real and imaginary parts, respectively, of the parameter they are attached to. A complex term, D , which is linear in H has been added to account for any first-order drift in the system, which is common due to the low signal level in many measurements on ultra-thin films. The mixing of the real and imaginary coefficients is explicit in Equations 6.40 and 6.41.

For a particular set of data there are four fitting parameters: M_{eff} correlates to the FMR field, ΔH is the linewidth, $\chi_{0,R}$ and $\chi_{0,I}$ are related to the amplitude and phase differences, respectively, between the transmission coefficient and the magnetic susceptibility, which manifests itself in the shape of the curves. As an example, the simultaneous fit of data shown in Figure 6.6(a) and (b) yielded $M_{eff} = 1.6$ kOe, $\Delta H = 626$ Oe, $\chi_{0,R} = 37470$ and $\chi_{0,I} = -88761$. Using Equation 6.21 and replacing $4\pi M_s$ with M_{eff} we can calculate the resonance field to be 3.85 kOe.

6.6 Summary

The physics of the dynamic motion of magnetization has been examined. When a magnetic moment is placed in a static external field which is not parallel to the moment, the moment will precess around the external field. From the model of uniform precession some real-world factors have been taken into account. The effects of finite sample size or demagnetization field, anisotropy

field, and loss have all been considered and the resulting changes to the equation of motion have been detailed.

When the magnetization is driven with an AC magnetic field to offset loss in the sample the phenomenon of ferromagnetic resonance may be observed. The measurement of this resonance can be used as a tool to extract information about both the static and dynamic physical properties of a sample. The experimental methods for rectangular waveguide and VNA FMR measurements have been demonstrated.

CHAPTER 7 Effects of lamination on damping of FeCo thin films

7.1 Overview

The damping properties of magnetic ultra-thin films are of critical importance for high-data-rate magnetic recording.¹²⁷⁻¹²⁹ The damping in recording media not only sets a natural limit on the time of magnetization switching, but also plays a critical role in microwave-assisted magnetization switching and domain wall-assisted switching.^{130,131} In magnetic thin film-based devices the bandwidth, insertion loss, and response time are all critically associated with the damping in the film.¹³²

Previous work as demonstrated four approaches for the tuning of the damping in ferromagnetic thin films: (1) addition of non-magnetic elements, (2) doping of rare earth elements, (3) film growth on different seed layers, and (4) composition variation in the case of alloy films. Approaches (1) and (3) add non-magnetic elements or use different seed layers to control the microstructural properties of the films and, thereby, control the two-magnon scattering (TMS) processes in the films.^{133,134} For approach (2) the damping of the films are enhanced through the slow relaxing impurity mechanism.¹³⁵ For method (4), one relies on the change of the alloy composition to manipulate the band structure and thereby tune the strength of magnon-electron scattering.¹²³ Although these approaches are all effective in tailoring the damping, they unfortunately give rise to significant changes in the other film properties, such as inhomogeneity, anisotropy, or saturation magnetization.

In this chapter the changes in damping properties of FeCo thin films with differing lamination layers are examined. FeCo is commonly used in magnetic recording write heads. The FeCo films were grown on Ru seed layers with non-magnetic Al₂O₃ laminating layers. Samples with no lamination and with 1-3 laminate layers were prepared. The Al₂O₃ laminate layers are 1 nm thick, and the total film thickness, including the Al₂O₃ layers, was kept constant at 30 nm. The Gilbert damping constants, α , of the samples were determined by ferromagnetic resonance (FMR) measurements. The FMR data indicate that, depending on the number of lamination layers, the damping of the FeCo thin film can vary over a range of 0.0027-0.0041, while both the anisotropy field and the inhomogeneity-caused FMR line broadening change no more than 5 Oe compared to the samples without lamination. These results not only demonstrate a new approach for tailoring the damping of magnetic thin films in general, but also provide significant implication for the design of future write heads in particular.

7.2 Experimental setup

The samples were deposited by Seagate Technology at room temperature by magnetron sputtering. The substrates were (100) Si wafers with 300-nm-thick SiO₂ capping layer. Prior to the growth of each film, a 1 nm thick Ru seed layer was deposited. During film deposition, a field of 75 Oe was applied in the film plane, which induced an in-plane uniaxial anisotropy in the film. The FMR measurements were carried out using an X-band microwave cavity, an X-band shorted waveguide, and a Ku-band shorted waveguide, with field modulation and lock-in detection techniques, as described in Chapter 6.4. The measurements performed in shorted waveguides permitted an FMR analysis across a broad frequency range of 8-18 GHz. All the FMR measurements were performed with external fields applied in the film planes. The measurements

in an X-band cavity allowed for simple and sensitive measurements as a function of the angle between an in-plane field relative to the easy axis due to anisotropy. The resonant frequency of the cavity is 9.5 GHz. The sizes of the samples are about 5 mm by 5 mm.

7.3 Measurement results

Figure 7.1 shows representative FMR data. The data were obtained with sample 4, which was FeCo(9.3 nm)/Al₂O₃(1 nm)/FeCo(9.3 nm)/ Al₂O₃ (1 nm)/FeCo(9.3 nm). In graph (a), the blue circles show a representative FMR profile measured in a Ku-band shorted waveguide at 16 GHz. The solid red line shows a fit to a Lorentzian trial function and the dashed green line shows a fit to a Gaussian trial function. One can see that the Lorentzian function fits the data much better than the Gaussian function. This indicates that the film has good uniformity.

Figure 7.1(b) and (c) present the FMR field, H_{FMR} , and linewidth, ΔH , as a function of frequency, $\omega/2\pi$, respectively. The blue symbols show the experimental data, which were obtained from fitting the measured FMR profiles, measured in X-, 8.5-12 GHz, and Ku-, 13-18 GHz, band shorted waveguides, with a Lorentzian derivative, as shown representatively in Figure 7.1(a) and discussed in Chapter 6.4. The error bars represent the standard error from the Lorentzian fitting function. The curve gives the fit to the Kittel equation, Equation 6.20, for an in-plane field configuration

$$\omega = 2\pi|\gamma|\sqrt{H_{FMR}(H_{FMR} + 4\pi M_s)} \quad 7.1$$

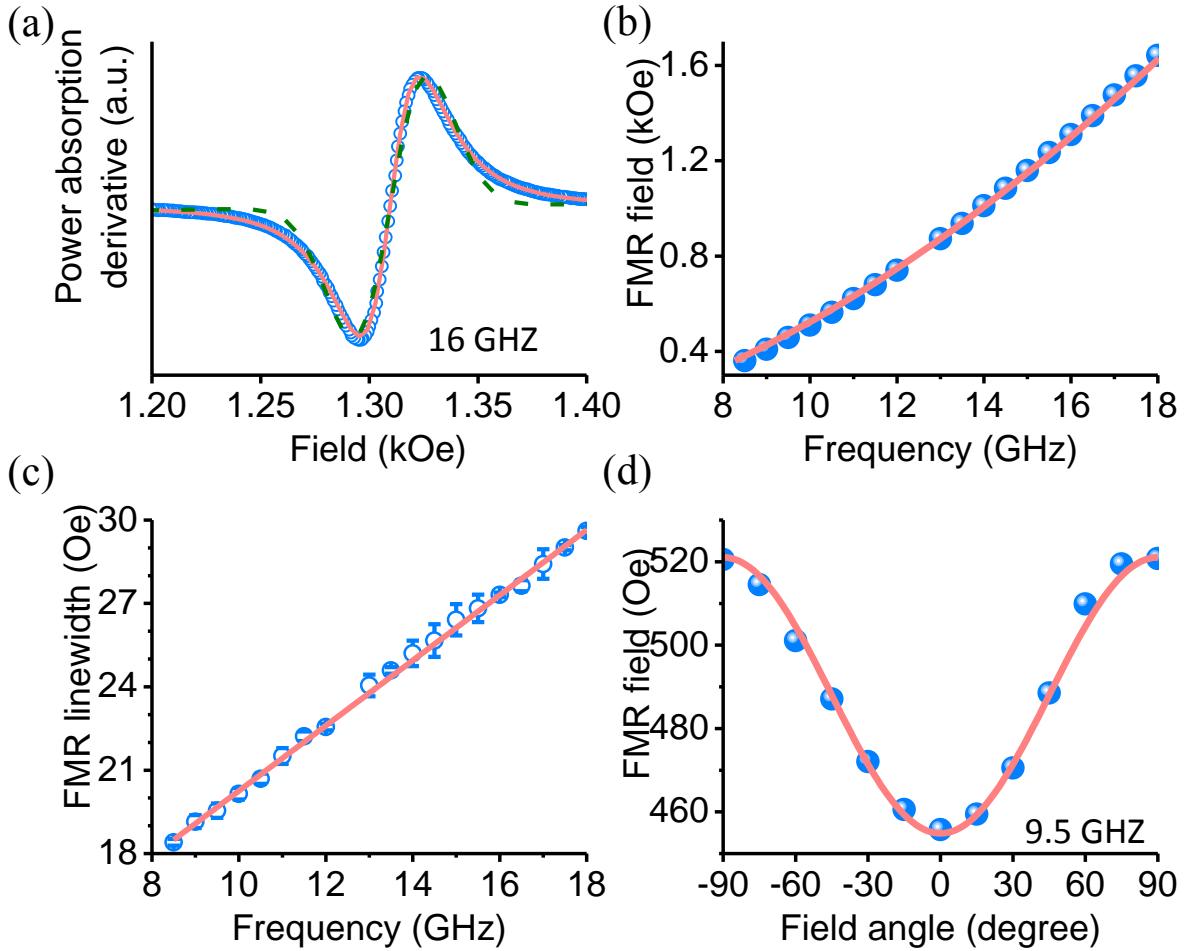


Figure 7.1 FMR data obtained with sample 4 - FeCo(9.3 nm)/Al₂O₃(1 nm)/FeCo(9.3 nm)/Al₂O₃ (1 nm)/FeCo(9.3 nm). In (a), the blue circles show a representative FMR profile measured at 16 GHz. The solid red and dashed green lines show fits to a Lorentzian function and Gaussian function, respectively. Graphs (b) and (c) present the FMR field and the peak-to-peak linewidth, respectively, as a function of frequency. The blue circles are the data from fitting. The red curve in (b) is a fit to Equation 7.1, while the red line in (c) shows a fit to Equation 7.2. Graph (d) presents the FMR field as a function of an in-plane field relative to the easy axis. The blue symbols show the data, while the curve is a fit to Equation 7.3. For the data in (a)-(c), the measurements were performed with an in-plane field applied along the easy axis.

where $|\gamma|$ is the absolute gyromagnetic ratio and $4\pi M_s$ is the saturation induction. The fitting used $4\pi M_s = 24$ kG and took $|\gamma|$ as the fitting parameter. The fitting yielded $|\gamma| = 2.79$ MHz/Oe, which agrees almost perfectly with the standard value of 2.8 MHz/Oe. The line in Figure 7.1(c) shows a linear fit to

$$\Delta H = \Delta H_{ILB} + \frac{2\alpha}{\sqrt{3}|\gamma|} \frac{\omega}{2\pi} \quad 7.2$$

where ΔH_{ILB} denotes film inhomogeneity line broadening. The fitting gave $\alpha = (2.84 \pm 0.06) \times 10^{-3}$ and $\Delta H_{ILB} = 8.52$ Oe.

Figure 7.1(d) presents H_{FMR} as a function of the in-plane field angle, ϕ , relative to the easy axis. The blue symbols show the data. They were determined through fitting the FMR profile measured in a X-band cavity with a frequency fixed at $f = 9.5$ GHz and by rotating the field in the sample plane. The data indicate the existence of a weak in-plane uniaxial anisotropy in the sample. The curve in Figure 7.1(d) shows a fit to

$$\omega = 2\pi|\gamma|\sqrt{[H_{FMR} + H_u \cos(2\phi)][H_{FMR} + H_u \cos^2 \phi + 4\pi M_s]} \quad 7.3$$

where H_u is the effective anisotropy field. The fitting made use of the above measured $|\gamma|$ and $4\pi M_s$ values and yielded $H_u = 33.4$ Oe.

Similar FMR measurements and numerical analyses were carried out on the other four samples. The FMR data from all five samples are presented in Table 7.1 and Figure 7.2. In Table 7.1, the second column gives the layered structures of the samples. Samples 1 and 2 have no lamination. Samples 3, 4, and 5 have 1, 2, and 3 laminating layers, respectively. Regardless of the lamination situations, all the samples have the same thickness which is 30 nm. The third column gives the $|\gamma|$ values obtained by fitting the H_{FMR} vs. $\omega/2\pi$ responses to Equation 7.1, as shown representatively in Figure 7.1(b). The fitting used $4\pi M_s = 24$ kG for all the samples. The fourth and fifth columns present the α and ΔH_{ILB} values. The determination of these values is shown in Figure 7.2, where the symbols show the measured ΔH data and the lines show the fits to Equation 7.2. The right most column in Table 7.1 presents the H_u values obtained by fitting the H_{FMR} vs. ϕ responses to Equation 7.3, as shown representatively in Figure 7.1(d).

7.4 Impact of lamination on film properties

The representative data shown in Figure 7.1 and the complete data shown in Table 7.1 and Figure 7.2 indicate several important properties of these samples. First, the α value determined is highly reliable as there is good agreement between the ΔH data in the X and Ku bands, and the linear fitting in Figure 7.2 is almost perfect with a fit error as low as $\pm 3 \times 10^{-5}$. Second, the film is uniform and homogeneous. This is indicated by two observations, namely, that the Lorentzian function fits the FMR profile much better than the Gaussian function in Figure 7.1(a) and the ΔH_{ILB} values are relatively small as shown in Table 7.1. Finally, the values for $|\gamma|$, α , and H_u obtained from fitting are all nearly identical to the values expected for FeCo thin films with no lamination.

Table 7.1 FMR results of FeCo thin films with different lamination configurations.

Sample	Structure	$ \gamma $ (MHz/Oe)	α ($\times 10^{-3}$)	ΔH_{ILB} (Oe)	H_u (Oe)
1	FeCo(30nm)	2.99	4.09 \pm 0.06	7.69	31.0
2	FeCo(30nm)	2.98	4.02 \pm 0.08	7.44	29.9
3	FeCo(14.5nm)/Al ₂ O ₃ (1nm) /FeCo(14.5nm)	2.83	2.70 \pm 0.08	10.36	26.7
4	FeCo(9.3nm)/Al ₂ O ₃ (1nm) /FeCo(9.3nm)/Al ₂ O ₃ (1nm) /FeCo(9.3nm)	2.79	2.84 \pm 0.06	8.52	33.4
5	FeCo(6.7nm)/Al ₂ O ₃ (1nm) /FeCo(6.7nm)/Al ₂ O ₃ (1nm) /FeCo(6.7nm)/Al ₂ O ₃ (1nm) /FeCo(6.7nm)	2.67	3.02 \pm 0.03	6.93	33.0

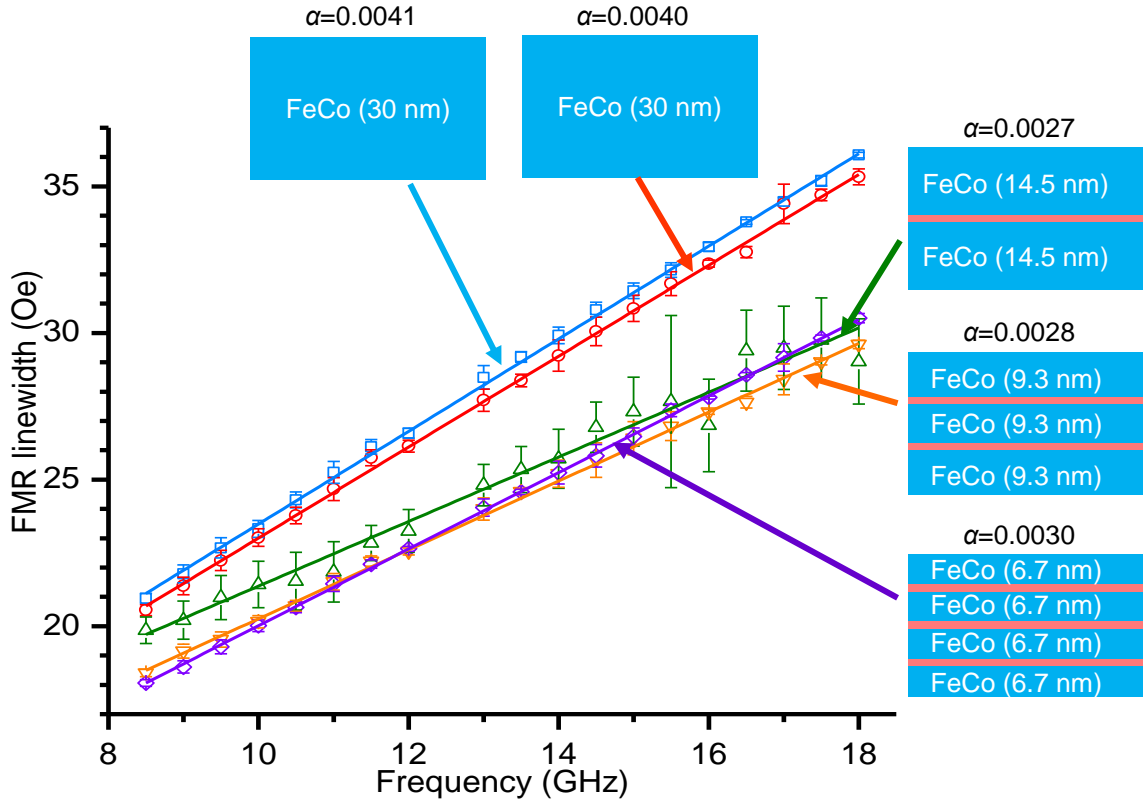


Figure 7.2 Peak-to-peak FMR linewidth as a function of frequency for five FeCo thin film samples, as indicated. For the three samples shown on the right, the red layers represent 1 nm thick Al_2O_3 laminating layers. For each data set, the symbols show the data and the line shows a fit to Equation 7.2.

This indicates that the incorporation of the two lamination layers does not significantly deteriorate the quality of the FeCo thin films.

The data shown in Table 7.1 and Figure 7.2 indicate two additional results about the magnetostatic properties of the films. First, $|\gamma|$ decreases with the number of lamination layers. One possible reason for this is that the $4\pi M_s$ was assumed the same for all the samples in the fitting process but might be slightly smaller in the samples with more laminating layers. Nevertheless, all the $|\gamma|$ values are close to the standard value of 2.8 MHz/Oe, with differences less than 7%. Second, the changes of ΔH_{ILB} and H_u with the number of laminating layers are both very small. The average

of ΔH_{ILB} is 8.2 Oe, and the corresponding standard deviation is 1.3 Oe. For H_u , the average and the standard deviation are 30.8 Oe and 2.7 Oe, respectively.

In terms of the dynamic properties of the films Table 7.1 and Figure 7.2 show two important results. First, the α values of the three samples with laminating layers are all notably smaller than those of the two samples with no lamination. This observation is believed to be due to lamination-caused reduction in eddy current associated damping. In general, the eddy current damping decreases with the square of the film thickness.^{136,137} Second, for the samples with lamination, α increases with the number of laminating layers. The correlation is related to surface damping produced by, for example, surface imperfection-associated two-magnon scattering.^{49,138} Such surface damping is negligible in relatively thick films and becomes important in ultra-thin films. For the three samples concerned here it is most likely that the FeCo layers are so thin that the eddy current damping is small and shows relatively weak thickness dependence, while the surface damping is comparatively large and strongly depends on the film thickness.

7.5 Summary

The effects of lamination on the properties of FeCo thin films have been studied experimentally. It is found that one can make use of lamination to reduce the damping of FeCo thin films, by as much as about 34%, without producing notable changes in the other properties of the films, such as the anisotropy field and the inhomogeneity. This study demonstrates a new approach for manipulation of damping in ferromagnetic metallic thin films. Future study is of great interest that combines this approach and other approaches^{123,133-135} for the realization of larger damping tuning with only moderate changes to the other properties. It is also of great interest to take advantage of this approach to optimize write heads for better performance.

CHAPTER 8 Increased sensitivity VNA-FMR measurement technique

8.1 Overview

Across technology and engineering fields it is highly desirable to create devices at ever smaller length scales.¹³⁹ This interest in nano-scale devices is present in the field of magnetization dynamics as well. For example, one promising technology for magnetic recording is bit patterned media. In bit patterned media, the bits are stored on a small (about 14 nm diameter) isolated magnetic dots, as opposed to the grains in a continuous media that current magnetic recording technology uses.¹⁴⁰ This technology has the potential to allow much higher areal density; however, at such small length scales the magnetization dynamics, and thus the switching of bits, are strongly affected by lateral confinement of spin waves and demagnetization fields.¹⁴¹ As ferromagnetic resonance is the standard measurement for characterizing magnetization dynamics, it is natural to apply this technique to nano devices. However, the signal-to-noise ratio of conventional FMR discussed in Chapter 6.4 is not high enough to distinguish clear resonance signals on samples with low magnetization volume.

There exist many different techniques for characterizing magnetization dynamics of small nanoscale devices, but there are a variety of strengths, restrictions, and weaknesses to these methods.¹⁴²⁻¹⁴⁹ For this reason, it is desirable to extend the classic FMR technique to higher sensitivity. In this work, the sensitivity of the FMR measurement has been extended by combining the field modulation and lock-in method of traditional FMR, the high sensitivity of the VNA-FMR

measurement, and the improvement in signal-to-noise ratio, via background subtraction, of a microwave interferometer.¹⁴²

8.2 Experimental setup

Figure 8.1 shows the schematic diagram of the high-sensitivity FMR system. The system has three major subsystems: (1) the magnetic field subsystem, (2) the microwave subsystem, and (3) the computer control subsystem.

The magnetic field system, shown in green in Figure 8.1, has two parts. The first part is a GMW 3473-70 electromagnet which is powered by a Danfysik system 8500 power supply. This creates a large DC bias magnetic field for FMR measurements. Depending on the positioning of the pole pieces, fields up to 20 kOe directed out of the film plane can be reached. During field-swept FMR measurements the field is set and allowed to stabilize for 5 seconds before the measurement is taken. The field is measured with a Lakeshore model 450 gauss meter and a Hall probe placed next to the sample. Then a new field is set accordingly and allowed to stabilize before the next data collection. The VNA-FMR measurement experiences background drifts so an AC detection technique is used. In addition to the large DC magnet a smaller Helmholtz coil is used as a modulation field source which adds a weaker low-frequency AC component to the DC bias field. A Wavetek model 81 function generator is used to generate a sine wave output with a frequency of 37 Hz. This signal is fed to a low-frequency audio amplifier to boost the output current such that the root mean square field output of the modulation Helmholtz coil is 5 Oe. This modulation field strength can be modified as necessary to suit the experiment.

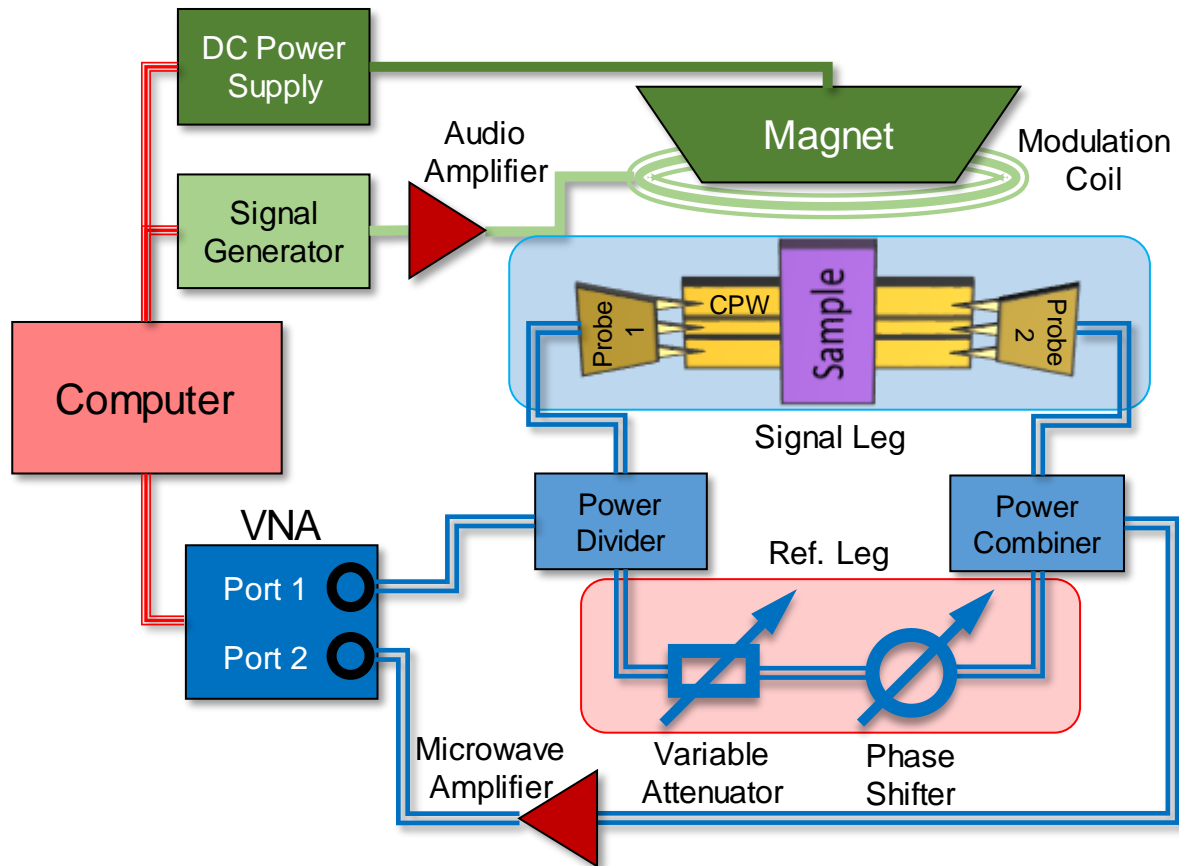


Figure 8.1 Diagram of the high sensitivity VNA-FMR system. The experimental setup consists of three main subsystems. (1) The magnetic field subsystem, connected with solid green lines, consists of the magnet and modulation coil, which are powered by the DC power supply and amplified signal generator outputs, respectively. This subsystem generates a large DC magnetic field with a small, low frequency, AC component out of the sample plane. (2) The microwave subsystem, connected with hollow blue lines, splits the microwave output of the VNA with a power divider and has two parts: the signal leg, highlighted in blue, which consists of two RF probes connected to a CPW, with the sample to be measured placed on the top of the CPW; and the reference leg, highlighted in red, which consists of a variable attenuator and phase shifter. The signals from the two legs are then combined via a power combiner and then amplified with a low-noise microwave amplifier before returning to the VNA, which acts as a detector. (3) The computer control subsystem, connected with red triple lines, is centered around the computer and its LabView program which controls the DC power supply, signal generator, and VNA. The computer also collects data from the VNA and a gauss meter (not shown).

The microwave subsystem, connected via hollow blue lines in Figure 8.1, uses an Agilent E8364 vector network analyzer as both a microwave source and a detector. The microwaves generated by the VNA, with frequency from 10 MHz to 67 GHz, are passed to a microwave

interferometer used for background subtraction. Port 1 of the VNA is connected to a Marki Microwave PD-0165 microwave power divider which splits the microwave signal into the two legs of the interferometer: the signal leg, highlighted in blue in Figure 8.1, and the reference leg, highlighted in red in Figure 8.1.

The first leg, the signal leg, uses the same experimental configuration as the VNA-FMR system described in Section 6.5. The sample is placed on a coplanar waveguide which is connected to two custom Picoprobe P-19-5641-B nonmagnetic ground-signal-ground probes. The probes are then connected to the power divider and power combiner. The power combiner is a reversely connected Marki Microwave power divider PD-0165.

The second leg, the reference leg, consists of a Narda Microwave model 4796 variable attenuator, with a low minimum insertion loss and an attenuation up to 30 dB, and a API Technologies 6705K-5 phase shifter. To tune the reference leg of the microwave interferometer, the magnetic field is set far higher than the sample resonance so that there is no magnetic signal from the signal leg. Next the phase shifter is tuned such that the signal and reference legs are 180° out of phase. Then the variable attenuator is tuned such that the reference and signal leg have the sample signal amplitude. The result of this is the cancellation of any non-magnetic signal emerging from the power combiner at the microwave frequency which will be measured. This is a Mach-Zehnder interferometer working as a notch filter.

The final part of the microwave subsystem is a B&Z Technologies BZ-01002650-451032-202525 low-noise microwave amplifier, with a gain of up to 34 dB, which boosts the signal returning to port 2 of the VNA. An example of this cancellation is shown in Figure 8.2(a). The magnitude of S_{21} is shown as a function of frequency with the interferometer tuned to cancel signal at 13 GHz. Minima in microwave transmission are seen roughly every 72 MHz with the strongest

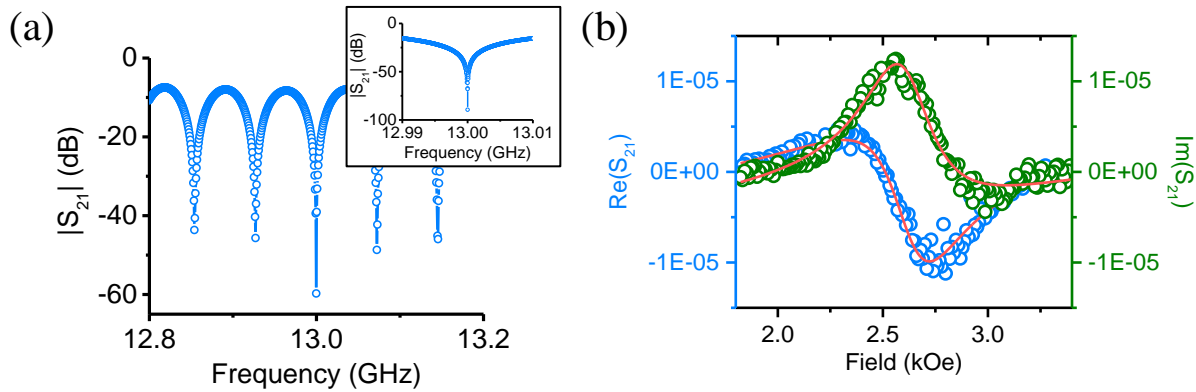


Figure 8.2 Results of interferometer tuning. (a) Magnitude of S_{21} as a function of frequency. The cancellation due to the interferometer tuned to 13 GHz over a range of 400 MHz is visible. The inset shows the cancellation in a narrower frequency range of 20 MHz centered around 13 GHz. The cancellation in this case is 89 dB. (b) Sample improved VNA-FMR data taken at 13 GHz. The blue and green circles show the real and imaginary parts of S_{21} , respectively. The red curves show fits to Equations 6.40 and 6.41.

cancellation at the tuned frequency of 13 GHz. The background cancellation can be tuned to around 90 dB, as seen in the inset of Figure 8.2(a).

The third subsystem is the computer control, which is shown connected with triple red lines in Figure 8.1. The computer runs a LabView program which controls the DC power supply, signal generator, and VNA output and reads the signals generated by the gauss meter and VNA. In order to accurately set the magnetic field, a calibration program is run which sweeps the output of the DC power supply and reads the corresponding field values from the gauss meter. After the magnet output has been calibrated, the desired frequency is set and the microwave interferometer tuned to that frequency as described above.

A field-swept FMR measurement may then be carried out as follows. The field is set and allowed to stabilize. Then the computer triggers a burst output from the signal generator to output the modulation field while triggering the measurement from the VNA after a small delay to ensure that the measurement is taken with a stable AC field. The program then collects the modulated real and imaginary S_{21} data from the VNA. The signal magnitude is averaged over 40 modulation field

cycles. This AC detection technique is functionally equivalent to the lock-in detection method. Due to the AC detection and background subtraction, this S_{21} signal has had noise or background drift removed and is only the result of the FMR response of the sample under test. The field is then set to a new value and the measurement is repeated. The end results are the real and imaginary FMR spectra shown in Figure 8.2(b), where the blue and green circles represent the data for the real and imaginary parts of S_{21} , respectively. These data are then fit via the method described in Section 6.5.2, shown by the red curves, and the relevant experimental parameters are extracted. The measurement can then be repeated at another frequency.

8.3 FMR measurement results with different systems

The improved VNA-FMR technique described above offers improved sensitivity and a larger frequency range compared to traditional shorted waveguide or cavity FMR technique and improved sensitivity, better field resolution, and faster measurements compared to the standard VNA-FMR technique. A comparison of the three measurement methods for a 1-nm-thick CoFeB sample are shown in Figure 8.3, Figure 8.4, and Figure 8.5.

The sample structure is Si substrate/Pd (3 nm)/CoFeB (1 nm)/MgO (1.6 nm)/Al (5 nm) deposited by sputtering and annealed in a rapid thermal annealing furnace at 450° C for 30 s. A 1- μ m-layer of photoresist was spin coated to prevent shorting the CPW signal line and grounds. The sample was provided by National Tsing Hua University in Taiwan.¹⁵⁰

The sample is sufficiently thin such that it is not possible to resolve a signal using traditional shorted waveguide FMR. A single frequency data point at 9.7 GHz is available via a microwave cavity as shown in Figure 8.3. Note that the data, represented by the blue circles, is very weak and close to the resolution limit of the system. Fitting this data with a Lorentzian fitting

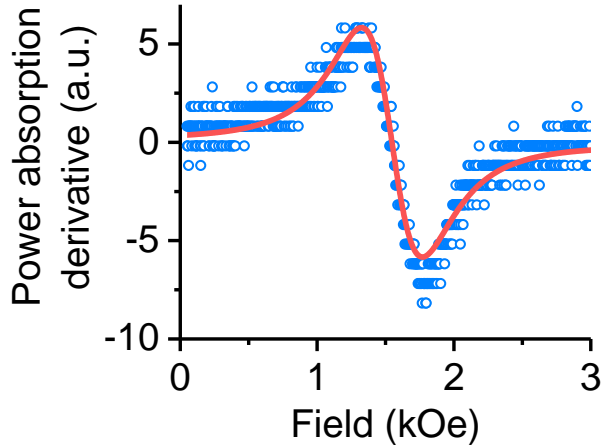


Figure 8.3 Microwave cavity FMR measurement. FMR data of 1-nm-thick CoFeB film sample measured with a 9.7 GHz microwave cavity and a lock-in detection technique. Blue circles show the data and the red curve is a Lorentzian derivative fit.

function, represented by the red curve, yields an FMR field of 1.54 kOe and an FMR linewidth of 444 Oe.

The measurement results for the VNA-FMR technique are shown in Figure 8.4. Figure 8.4(a) shows representative data taken at 12.9 GHz, where the blue and green circles represent the data for the real and imaginary parts of S_{21} , respectively. This technique, described in more detail in Section 6.5, gives better results than the cavity technique and the signal at 13 GHz is clearly visible. The data presented is the average of 40 field swept data sets. The data can be fit with the method described in Section 6.5.2, represented by the red curves. The fit yields an FMR field of 2.52 kOe and an FMR linewidth of 622 Oe. Note that there are relatively few data points near the resonance and there is significant linewidth broadening, both of which are the results of the fast field sweep. Figure 8.4(b) shows the FMR field as a function of microwave frequency. The data, shown by the blue circles, was obtained from the fitting of each individual constant frequency field-swept measurement, such as Figure 8.4(a). The data were fit by Equation 6.21, the Kittel equation for field out-of-plane. The fitting resulted in $|\gamma| = 3.12$ GHz/Oe and $M_{\text{eff}} = -1.61$ kG.

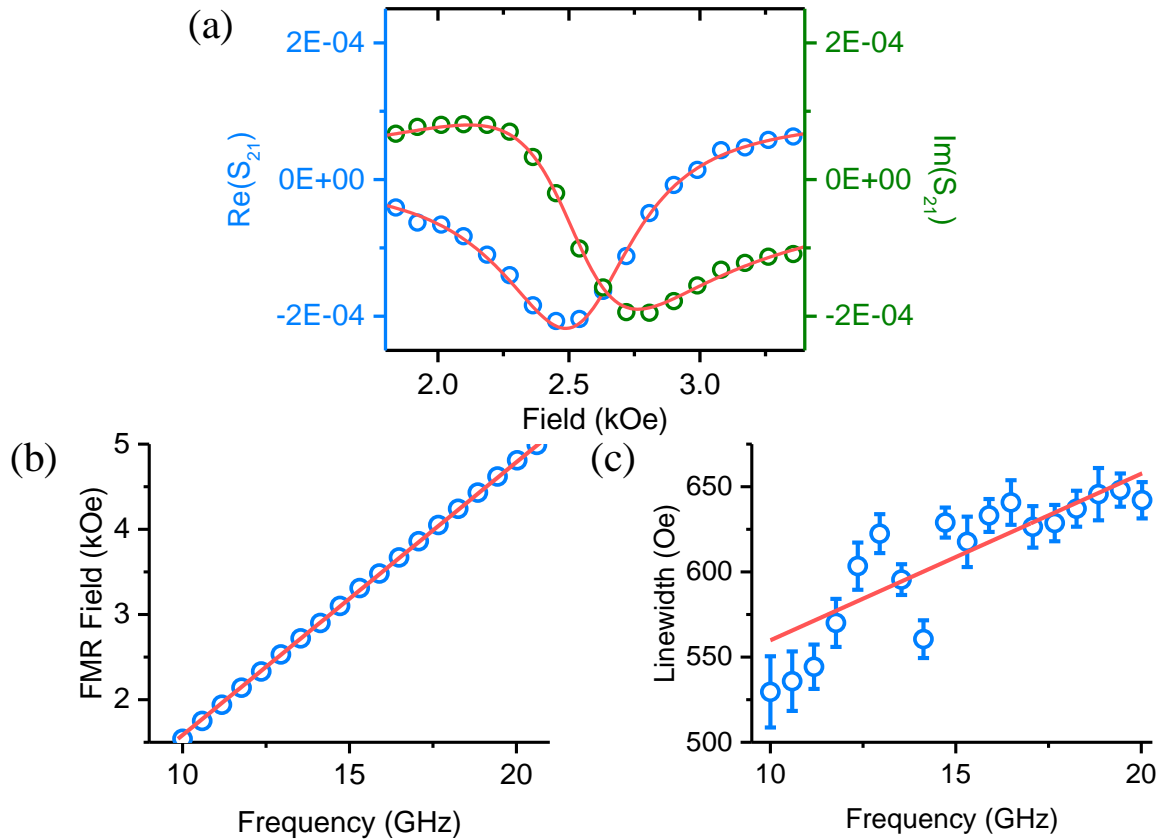


Figure 8.4 VNA-FMR measurements. (a) Representative FMR data of 1-nm-thick CoFeB film sample measured with the VNA-FMR technique at 12.9 GHz. The blue and green circles show the real and imaginary parts of the S_{21} data, respectively. The red curves are fits to Equations 6.40 and 6.41. (b) FMR field as a function of microwave frequency. The blue circles are the data extracted from each field swept measurement, and the red curve is a fit to the Kittel equation, Equation 6.21. (c) FMR linewidth as a function of frequency. Blue circles are data extracted from field-swept measurements, with error bars from fitting, and the red curve is a fit to Equation 6.28

Figure 8.4(c) shows the FMR linewidth, which was determined from the fitting of the field-swept data, such as Figure 8.4(a), as a function of frequency. The data were fit with Equation 6.28, which resulted in $\alpha = 0.026$ and $\Delta H_{ILB} = 462$ Oe.

The results of the improved VNA-FMR technique are shown in Figure 8.5. Figure 8.5(a) shows representative data taken at 13 GHz, with the blue and green circles representing the data for the real and imaginary parts of S_{21} , respectively. Each data point is the result of 40 field

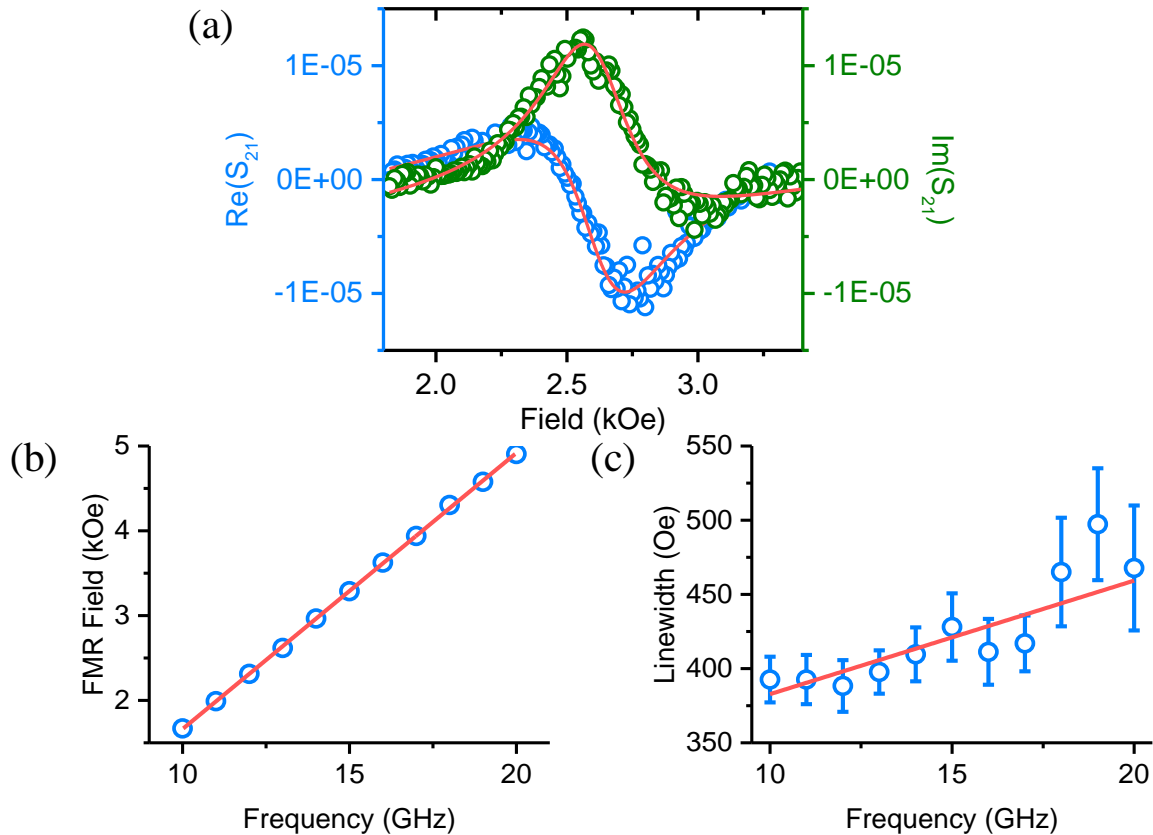


Figure 8.5 Improved VNA-FMR measurement. (a) Representative FMR data of 1-nm-thick CoFeB film sample measured with the improved VNA-FMR technique at 13 GHz. The blue and green circles show the real and imaginary parts of the S_{21} data, respectively. The red curves are fits to Equations 6.40 and 6.41. (b) FMR field vs. frequency. The blue circles are the data extracted from each field-swept measurement, and the red curve is a fit to the Kittel equation, Equation 6.21. (c) FMR linewidth as a function of frequency. Blue circles are data extracted from field-swept measurements, with error bars from fitting, and the red curve is a fit to Equation 6.28

modulation cycles. The signal from the improved VNA-FMR technique is clear and there is little background drift. Fitting the data with Equations 6.40 and 6.41, represented by the red curves, yields an FMR field of 2.61 kOe and an FMR linewidth of 397 Oe. Note that the linewidth is much narrower with this technique due to the slower field sweep. Figure 8.4(b) shows the FMR field as a function of microwave frequency. The data, shown by the blue circles, was obtained from the fitting of each individual constant frequency field-swept measurement. The data were fit by Equation 6.21, the Kittel equation for field out-of-plane. The fitting resulted in $|\gamma| = 3.07 \text{ GHz/Oe}$

and $M_{\text{eff}} = -1.59$ kG. Figure 8.5(c) shows the FMR linewidth, which was determined from the fitting of the field-swept data, as a function of frequency. The data were fit with Equation 6.28, which resulted in $\alpha = 0.020$ and $\Delta H_{\text{ILB}} = 306$ Oe.

8.4 Comparison of different ferromagnetic resonance techniques

It is clear that the cavity FMR technique is not a viable means of FMR measurements for such low-volume samples, as the signal is very weak and limited to only a single frequency point.

The standard VNA-FMR technique is a reasonable means for measuring the CoFeB sample presented in the previous section. It does, however, have limitations. In order to reduce signal drift, the magnetic field is swept as fast as possible. There are two important consequences. First, there are not very many data points in the field range of interest. The effective field step size in Figure 8.4(a) is about 90 Oe. If the linewidth of the sample is narrow, as would be the case with YIG or other magnetic oxides, it would be impossible to measure the linewidth accurately. Second, the fast field sweep results in artificial linewidth broadening. This is because the field is not stable during each measurement and the magnetization precession is not in a steady state. Compared to the cavity or improved VNA-FMR techniques, the linewidth is about 150 Oe larger. This linewidth broadening manifests itself primarily as increased frequency independent linewidth broadening in ΔH_{ILB} , but also shows up as a small increase of the Gilbert damping parameter, α . This system is also nearing the limit of its detection sensitivity. For samples with a greatly reduced magnetic volume it may be impossible to distinguish a signal from noise, even with extensive averaging.

The improved VNA-FMR measurement technique represents a significant advance in the capabilities of the system. The signal measured does not show any artificial linewidth broadening due to fast field sweeping. With the improved VNA-FMR technique, the field step size and stabilization time are both fully configurable. In the data in Figure 8.5(a) the field step size is 10 Oe and the field stabilization time is 4 s. This leads to more accurate measurements of ΔH_{ILB} and α as shown in Figure 8.5(c). Additionally, the sensitivity of this system is much greater, and has much greater capability for scaling. While it is not practical to increase the averaging of the VNA-FMR technique, due to the amount of time required to make a measurement, the number of modulation field cycles over which the improved VNA-FMR technique measures can be significantly increased without impacting the measurement time. This enables this measurement technique to measure samples with much lower signal levels than the standard VNA-FMR technique.

8.5 Summary

A new VNA-FMR measurement technique has been developed which uses a microwave interferometer and AC detection to achieve ultrahigh sensitivity. Improved sensitivity has been demonstrated by comparing FMR measurements performed on a 1-nm-thick CoFeB film with microwave cavity FMR, standard VNA-FMR, and improved VNA-FMR techniques. These results demonstrate the very high measurement sensitivity and accuracy achieved by the new FMR system. This improved measurement technique will enable observations of extremely small FMR signals and open avenues to characterize magnetization dynamics in a new realm of low-volume samples.¹⁴²

CHAPTER 9 **Summary**

9.1 **Summary**

This dissertation provides experimental measurements of spin currents and ferromagnetic resonance (FMR).

In Chapter 3 the light-induced generation of pure spin currents were reported in both Pt/YIG and Pt/BaM via the SSE. The BaM had strong in-plane uniaxial anisotropy and was therefore self-biased. Upon exposure to light, a temperature difference is established across the film thickness, which gives rise to a pure spin current in the Pt via the SSE. In BaM, this experiment demonstrates a spin current source which requires neither magnetic field, microwave source, nor heating/cooling device, but light only.

Chapter 4 demonstrated an entirely new means for spin current generation, the photo-spin-voltaic effect. This work reported that a spin voltage can be created by photons in a non-magnetic metal in close proximity to a magnetic insulator. The experiments used bi-layered structures consisting of nm-thick Pt films grown on magnetic insulators. When illuminated by light, for the Pt layer in proximity to a magnetic insulator there exists a spin-dependent excitation which results in a spin voltage near the interface and a corresponding pure spin current across the Pt thickness.

The results of the previous chapter were expanded in Chapter 5, which reported the PSV effect in Pd, Au, and Cr, in addition to Pt. The experiments in this work were conducted in a regime where the PSV effect and the SSE coexist, and the PSV strength is comparable to the SSE strength. The data show that the PSV effect can be stronger than, similar to, or weaker than the SSE depending on the light source, providing further evidence for the wavelength dependence of the

PSV effect. The trend of PSV strength using different light sources changes in different samples, indicating the unique wavelength-dependent excitation for each metal.

The effects of lamination on the damping properties of FeCo thin films were studied in Chapter 7. It was found that the lamination could significantly reduce the Gilbert damping constant (α) of FeCo thin films, by as much as 34%. It was also found that α increased with the number of laminating layers in the films. In spite of the significant change in α , however, the lamination produces only small changes in the other properties of the film, such as uniaxial anisotropy.

The VNA-FMR measurement technique was improved in Chapter 8 with the use of field modulation, lock-in detection, and background subtraction. These improvements led to increased measurement sensitivity and can enable the measurement of ultra-low-volume magnetic samples.

9.2 Future work

The research summarized above has opened several exciting avenues of future investigation.

The photo-spin-voltaic effect, in particular, naturally leads to a wide variety of possible future work of both fundamental and practical significance. There is still much to consider in terms of different materials which can be used for this effect, both for the magnetic layer and the non-magnetic metal layer. Additionally, there are fundamental questions about the nature of the effect which can be explored in greater detail. For example, the exact wavelength dependence of the effect is of great interest. More qualitative measurements of the wavelength dependence are called for. For example, a measurement of the PSV voltage signal excited with narrow-bandwidth light can produce a measurement of the PSV signal as a function of wavelength, which would be a significant result that can be compared to the existing theoretical model. It is especially important

to compare the wavelength dependence of different metal layers. The limits of the time-domain response of the PSV signal have also yet to be probed. The effects of interface quality on the PSV signal are another possible research path. From a practical perspective, there are several possible uses of the PSV effect which warrant further investigation. The possibility of using light to induce switching in a magnetic layer is one such opportunity.

In addition to the wealth of opportunities presented by the PSV effect, the upgraded VNA-FMR system also opens appealing research avenues. With increased sensitivity, it may be possible to measure ultra-thin nano-patterned devices, such as the nano-dots which may potentially be used in bit-patterned media, and other samples with extremely weak FMR signals.

References

- 1 Dayarathna, M., Wen, Y. & Fan, R., "Data Center Energy Consumption Modeling: A Survey". *IEEE Communications Surveys & Tutorials* **18**, 732 (2016).
- 2 Poess, M. & Nambiar, R. O., "Energy cost, the key challenge of today's data centers: a power consumption analysis of TPC-C results". *Proc. VLDB Endow.* **1**, 1229 (2008).
- 3 Van Heddeghem, W., Lambert, S., Lannoo, B., Colle, D., Pickavet, M. & Demeester, P., "Trends in worldwide ICT electricity consumption from 2007 to 2012". *Computer Communications* **50**, 64 (2014).
- 4 Hall, E. H., "On a New Action of the Magnet on Electric Currents". *American Journal of Mathematics* **2**, 287 (1879).
- 5 D'yakonov, M. & Perel, V., "Possibility of orienting electron spins with current". *Soviet Journal of Experimental and Theoretical Physics Letters* **13**, 467 (1971).
- 6 Hirsch, J., "Spin hall effect". *Physical Review Letters* **83**, 1834 (1999).
- 7 Dyakonov, M., "Spin Hall Effect". *International Journal of Modern Physics B* **23**, 2556 (2009).
- 8 Hoffmann, A., "Spin Hall effects in metals". *IEEE transactions on magnetics* **49**, 5172 (2013).
- 9 Tserkovnyak, Y., Brataas, A. & Bauer, G. E., "Enhanced Gilbert damping in thin ferromagnetic films". *Physical review letters* **88**, 117601 (2002).
- 10 Heinrich, B. in *Ultrathin Magnetic Structures III* 143 (Springer, 2005).
- 11 Tserkovnyak, Y., Brataas, A. & Bauer, G. E., "Spin pumping and magnetization dynamics in metallic multilayers". *Physical Review B* **66**, 224403 (2002).

- 12 Heinrich, B., Tserkovnyak, Y., Woltersdorf, G., Brataas, A., Urban, R. & Bauer, G. E., "Dynamic exchange coupling in magnetic bilayers". *Physical review letters* **90**, 187601 (2003).
- 13 Boone, C. T., Shaw, J. M., Nembach, H. T. & Silva, T. J., "Spin-scattering rates in metallic thin films measured by ferromagnetic resonance damping enhanced by spin-pumping". *Journal of Applied Physics* **117**, 223910 (2015).
- 14 Burrowes, C., Heinrich, B., Kardasz, B., Montoya, E., Girt, E., Sun, Y., Song, Y.-Y. & Wu, M., "Enhanced spin pumping at yttrium iron garnet/Au interfaces". *Applied Physics Letters* **100**, 092403 (2012).
- 15 Sandweg, C., Kajiwara, Y., Ando, K., Saitoh, E. & Hillebrands, B., "Enhancement of the spin pumping efficiency by spin wave mode selection". *Applied Physics Letters* **97**, 252504 (2010).
- 16 Heinrich, B., Burrowes, C., Montoya, E., Kardasz, B., Girt, E., Song, Y.-Y., Sun, Y. & Wu, M., "Spin pumping at the magnetic insulator (YIG)/normal metal (Au) interfaces". *Physical review letters* **107**, 066604 (2011).
- 17 Wang, H., Du, C., Hammel, P. C. & Yang, F., "Antiferromagnonic spin transport from $\text{Y}_3\text{Fe}_5\text{O}_{12}$ into NiO". *Physical review letters* **113**, 097202 (2014).
- 18 Jungfleisch, M., Chumak, A., Kehlberger, A., Lauer, V., Kim, D., Onbasli, M., Ross, C., Kläui, M. & Hillebrands, B., "Thickness and power dependence of the spin-pumping effect in $\text{Y}_3\text{Fe}_5\text{O}_{12}$ /Pt heterostructures measured by the inverse spin Hall effect". *Physical Review B* **91**, 134407 (2015).
- 19 Chumak, A., Vasyuchka, V., Serga, A. & Hillebrands, B., "Magnon spintronics". *Nature Physics* **11**, 453 (2015).

- 20 Janantha, P. A. P., *Nonlinear spin waves in magnetic thin films–foldover, dispersive shock waves, and spin pumping*, Colorado State University, (2016).
- 21 Seebeck, T. J., "Ueber die magnetische Polarisation der Metalle und Erze durch Temperatur-Differenz". *Annalen der Physik* **82**, 133 (1826).
- 22 Uchida, K., Takahashi, S., Harii, K., Ieda, J., Koshibae, W., Ando, K., Maekawa, S. & Saitoh, E., "Observation of the spin Seebeck effect". *Nature* **455**, 778 (2008).
- 23 Xiao, J., Bauer, G. E., Uchida, K.-c., Saitoh, E. & Maekawa, S., "Theory of magnon-driven spin Seebeck effect". *Physical Review B* **81**, 214418 (2010).
- 24 Jaworski, C., Yang, J., Mack, S., Awschalom, D., Myers, R. & Heremans, J., "Spin-Seebeck effect: A phonon driven spin distribution". *Physical review letters* **106**, 186601 (2011).
- 25 Qu, D., Huang, S., Hu, J., Wu, R. & Chien, C., "Intrinsic spin Seebeck effect in Au/YIG". *Physical review letters* **110**, 067206 (2013).
- 26 Sanders, D. & Walton, D., "Effect of magnon-phonon thermal relaxation on heat transport by magnons". *Physical Review B* **15**, 1489 (1977).
- 27 Foros, J., Brataas, A., Tserkovnyak, Y. & Bauer, G. E., "Magnetization noise in magnetoelectronic nanostructures". *Physical review letters* **95**, 016601 (2005).
- 28 Uchida, K.-i., Adachi, H., Ota, T., Nakayama, H., Maekawa, S. & Saitoh, E., "Observation of longitudinal spin-Seebeck effect in magnetic insulators". *Applied Physics Letters* **97**, 172505 (2010).
- 29 Schmid, M., Srichandan, S., Meier, D., Kuschel, T., Schmalhorst, J.-M., Vogel, M., Reiss, G., Strunk, C. & Back, C. H., "Transverse spin Seebeck effect versus anomalous and planar Nernst effects in permalloy thin films". *Physical review letters* **111**, 187201 (2013).

- 30 Chang, H., Janantha, P. P., Ding, J., Liu, T., Cline, K., Gelfand, J. N., Li, W., Marconi, M. C. & Wu, M., "Role of damping in spin Seebeck effect in yttrium iron garnet thin films". *Science Advances* **3**, e1601614 (2017).
- 31 Schreier, M., Kamra, A., Weiler, M., Xiao, J., Bauer, G. E., Gross, R. & Goennenwein, S. T., "Magnon, phonon, and electron temperature profiles and the spin Seebeck effect in magnetic insulator/normal metal hybrid structures". *Physical Review B* **88**, 094410 (2013).
- 32 Huebener, R. & Seher, A., "Nernst effect and flux flow in superconductors. I. Niobium". *Physical Review* **181**, 701 (1969).
- 33 Pu, Y., Johnston-Halperin, E., Awschalom, D. & Shi, J., "Anisotropic thermopower and planar Nernst effect in Ga_{1-x}Mn_xAs ferromagnetic semiconductors". *Physical review letters* **97**, 036601 (2006).
- 34 Ky, V. D., "The planar Nernst effect in permalloy films". *physica status solidi (b)* **17** (1966).
- 35 Avery, A., Pufall, M. & Zink, B., "Observation of the planar Nernst effect in permalloy and nickel thin films with in-plane thermal gradients". *Physical review letters* **109**, 196602 (2012).
- 36 Uchida, K., Ota, T., Harii, K., Takahashi, S., Maekawa, S., Fujikawa, Y. & Saitoh, E., "Spin-Seebeck effects in films". *Solid State Communications* **150**, 524 (2010).
- 37 Jaworski, C., Yang, J., Mack, S., Awschalom, D., Heremans, J. & Myers, R., "Observation of the spin-Seebeck effect in a ferromagnetic semiconductor". *Nature materials* **9**, 898 (2010).
- 38 Jaworski, C., Myers, R., Johnston-Halperin, E. & Heremans, J., "Giant spin Seebeck effect in a non-magnetic material". *Nature* **487**, 210 (2012).

- 39 Uchida, K., Xiao, J., Adachi, H., Ohe, J.-i., Takahashi, S., Ieda, J., Ota, T., Kajiwara, Y., Umezawa, H. & Kawai, H., "Spin seebeck insulator". *Nature materials* **9**, 894 (2010).
- 40 Adachi, H., Uchida, K.-i., Saitoh, E., Ohe, J.-i., Takahashi, S. & Maekawa, S., "Gigantic enhancement of spin Seebeck effect by phonon drag". *Applied Physics Letters* **97**, 252506 (2010).
- 41 Meier, D., Kuschel, T., Shen, L., Gupta, A., Kikkawa, T., Uchida, K.-i., Saitoh, E., Schmalhorst, J.-M. & Reiss, G., "Thermally driven spin and charge currents in thin NiFe₂O₄/Pt films". *Physical Review B* **87**, 054421 (2013).
- 42 Ramos, R., Kikkawa, T., Uchida, K., Adachi, H., Lucas, I., Aguirre, M., Algarabel, P., Morellón, L., Maekawa, S. & Saitoh, E., "Observation of the spin Seebeck effect in epitaxial Fe₃O₄ thin films". *Applied Physics Letters* **102**, 072413 (2013).
- 43 Kalarickal, S. S., Krivosik, P., Wu, M., Patton, C. E., Schneider, M. L., Kabos, P., Silva, T. & Nibarger, J. P., "Ferromagnetic resonance linewidth in metallic thin films: Comparison of measurement methods". *Journal of Applied Physics* **99**, 093909 (2006).
- 44 Chang, H., Li, P., Zhang, W., Liu, T., Hoffmann, A., Deng, L. & Wu, M., "Nanometer-thick yttrium iron garnet films with extremely low damping". *IEEE Magnetics Letters* **5**, 1 (2014).
- 45 Li, P., Ellsworth, D., Chang, H., Janantha, P., Richardson, D., Shah, F., Phillips, P., Vijayarathy, T. & Wu, M., "Generation of pure spin currents via spin Seebeck effect in self-biased hexagonal ferrite thin films". *Applied Physics Letters* **105**, 242412 (2014).
- 46 Winkler, G. D., *Magnetic garnets*. (Vieweg, 1981).
- 47 Smit, J. & Wijn, H. P. J., *Ferrites: physical properties of ferrimagnetic oxides in relation to their technical applications*. (Wiley, 1959).

- 48 Von Aulock, W. H., *Handbook of microwave ferrite materials*. (ProQuest, 1965).
- 49 Sparks, M., *Ferromagnetic-relaxation theory*. (McGraw-Hill, 1964).
- 50 Song, Y.-Y., Kalarickal, S. & Patton, C. E., "Optimized pulsed laser deposited barium ferrite thin films with narrow ferromagnetic resonance linewidths". *Journal of applied physics* **94**, 5103 (2003).
- 51 Lax, B. & Button, K. J., *Microwave ferrites and ferrimagnetics*. (1962).
- 52 Wigen, P., McMichael, R. & Jayaprakash, C., "Route to chaos in the magnetic garnets". *Journal of magnetism and magnetic materials* **84**, 237 (1990).
- 53 Kimura, T., Otani, Y., Sato, T., Takahashi, S. & Maekawa, S., "Room-temperature reversible spin Hall effect". *Physical review letters* **98**, 156601 (2007).
- 54 Valenzuela, S. O. & Tinkham, M., "Direct electronic measurement of the spin Hall effect". *Nature* **442**, 176 (2006).
- 55 Saitoh, E., Ueda, M., Miyajima, H. & Tataru, G., "Conversion of spin current into charge current at room temperature: Inverse spin-Hall effect". *Applied Physics Letters* **88**, 182509 (2006).
- 56 Sun, Y. & Wu, M., *Yttrium iron garnet nano films: Epitaxial growth, spin-pumping efficiency, and Pt-capping-caused damping*. Vol. 64 (2013).
- 57 DiSalvo, F. J., "Thermoelectric cooling and power generation". *Science* **285**, 703 (1999).
- 58 Urban, R., Woltersdorf, G. & Heinrich, B., "Gilbert damping in single and multilayer ultrathin films: role of interfaces in nonlocal spin dynamics". *Physical Review Letters* **87**, 217204 (2001).

- 59 Mizukami, S., Ando, Y. & Miyazaki, T., "Effect of spin diffusion on Gilbert damping for a very thin permalloy layer in Cu/permalloy/Cu/Pt films". *Physical Review B* **66**, 104413 (2002).
- 60 Day, C., "Two groups observe the spin hall effect in semiconductors". *Physics Today* **58**, 17 (2005).
- 61 Ellsworth, D., Lu, L., Lan, J., Chang, H., Li, P., Wang, Z., Hu, J., Johnson, B., Bian, Y. & Xiao, J., "Photo-spin-voltaic effect". *Nature Physics* **12**, 861 (2016).
- 62 Kittel, C., *Introduction to Solid State Physics*. 8th edn, (John Wiley, 2005).
- 63 Linares, R., "Epitaxial growth of narrow linewidth yttrium iron garnet films". *Journal of Crystal Growth* **3**, 443 (1968).
- 64 Liu, T., Chang, H., Vlaminc, V., Sun, Y., Kabatek, M., Hoffmann, A., Deng, L. & Wu, M., "Ferromagnetic resonance of sputtered yttrium iron garnet nanometer films". *Journal of Applied Physics* **115**, 17A501 (2014).
- 65 Huang, S., Wang, W., Lee, S., Kwo, J. & Chien, C., "Intrinsic spin-dependent thermal transport". *Physical review letters* **107**, 216604 (2011).
- 66 Yin, S., Mao, Q., Meng, Q., Li, D. & Zhao, H., "Hybrid anomalous and planar Nernst effect in permalloy thin films". *Physical Review B* **88**, 064410 (2013).
- 67 Kehlberger, A., Ritzmann, U., Hinzke, D., Guo, E.-J., Cramer, J., Jakob, G., Onbasli, M. C., Kim, D. H., Ross, C. A. & Jungfleisch, M. B., "Length scale of the spin Seebeck effect". *Physical review letters* **115**, 096602 (2015).
- 68 Jakubisova-Liskova, E., Visnovsky, S., Chang, H. & Wu, M., "Optical spectroscopy of sputtered nanometer-thick yttrium iron garnet films". *Journal of Applied Physics* **117**, 17B702 (2015).

- 69 Hughes, J. L. & Sipe, J., "Calculation of second-order optical response in semiconductors". *Physical Review B* **53**, 10751 (1996).
- 70 Huang, S.-Y., Fan, X., Qu, D., Chen, Y., Wang, W., Wu, J., Chen, T., Xiao, J. & Chien, C., "Transport magnetic proximity effects in platinum". *Physical review letters* **109**, 107204 (2012).
- 71 Lu, Y., Choi, Y., Ortega, C., Cheng, X., Cai, J., Huang, S., Sun, L. & Chien, C., "Pt magnetic polarization on Y₃Fe₅O₁₂ and magnetotransport characteristics". *Physical review letters* **110**, 147207 (2013).
- 72 Zhou, X., Ma, L., Shi, Z., Guo, G., Hu, J., Wu, R. & Zhou, S., "Tuning magnetotransport in PdPt/Y₃Fe₅O₁₂: Effects of magnetic proximity and spin-orbit coupling". *Applied Physics Letters* **105**, 012408 (2014).
- 73 Weiler, M., Althammer, M., Czeschka, F. D., Huebl, H., Wagner, M. S., Opel, M., Imort, I.-M., Reiss, G., Thomas, A. & Gross, R., "Local charge and spin currents in magnetothermal landscapes". *Physical review letters* **108**, 106602 (2012).
- 74 Agrawal, M., Vasyuchka, V., Serga, A., Kiriara, A., Pirro, P., Langner, T., Jungfleisch, M., Chumak, A., Papaioannou, E. T. & Hillebrands, B., "Role of bulk-magnon transport in the temporal evolution of the longitudinal spin-Seebeck effect". *Physical Review B* **89**, 224414 (2014).
- 75 Roschewsky, N., Schreier, M., Kamra, A., Schade, F., Ganzhorn, K., Meyer, S., Huebl, H., Geprägs, S., Gross, R. & Goennenwein, S. T., "Time resolved spin Seebeck effect experiments". *Applied Physics Letters* **104**, 202410 (2014).
- 76 Ganichev, S., Ivchenko, E., Bel'Kov, V., Tarasenko, S., Sollinger, M., Weiss, D., Wegscheider, W. & Prettl, W., "Spin-galvanic effect". *Nature* **417**, 153 (2002).

- 77 Leyder, C., Romanelli, M., Karr, J. P., Giacobino, E., Liew, T. C., Glazov, M. M., Kavokin, A. V., Malpuech, G. & Bramati, A., "Observation of the optical spin Hall effect". *Nature Physics* **3**, 628 (2007).
- 78 Miah, M. I., "Observation of the anomalous Hall effect in GaAs". *Journal of Physics D: Applied Physics* **40**, 1659 (2007).
- 79 Wunderlich, J., Park, B.-G., Irvine, A. C., Zârbo, L. P., Rozkotová, E., Nemeč, P., Novák, V., Sinova, J. & Jungwirth, T., "Spin Hall effect transistor". *Science* **330**, 1801 (2010).
- 80 Ando, K., Morikawa, M., Trypiniotis, T., Fujikawa, Y., Barnes, C. & Saitoh, E., "Direct conversion of light-polarization information into electric voltage using photoinduced inverse spin-Hall effect in Pt/GaAs hybrid structure: Spin photodetector". *Journal of Applied Physics* **107**, 113902 (2010).
- 81 Kampfrath, T., Battiato, M., Maldonado, P., Eilers, G., Nötzold, J., Mährlein, S., Zbarsky, V., Freimuth, F., Mokrousov, Y. & Blügel, S., "Terahertz spin current pulses controlled by magnetic heterostructures". *Nature nanotechnology* **8**, 256 (2013).
- 82 Endres, B., Ciorga, M., Schmid, M., Utz, M., Bougeard, D., Weiss, D., Bayreuther, G. & Back, C., "Demonstration of the spin solar cell and spin photodiode effect". *Nature communications* **4** (2013).
- 83 Uchida, K., Adachi, H., Kikuchi, D., Ito, S., Qiu, Z., Maekawa, S. & Saitoh, E., "Generation of spin currents by surface plasmon resonance". *Nature communications* **6** (2015).
- 84 Sinova, J., Valenzuela, S. O., Wunderlich, J., Back, C. & Jungwirth, T., "Spin hall effects". *Reviews of Modern Physics* **87**, 1213 (2015).

- 85 Fullerton, E. E., Riggs, K., Sowers, C., Bader, S. & Berger, A., "Suppression of biquadratic coupling in Fe/Cr (001) superlattices below the Néel transition of Cr". *Physical review letters* **75**, 330 (1995).
- 86 Arrott, A., Werner, S. & Kendrick, H., "First-order magnetic phase change in chromium at 38.5 c". *Physical Review Letters* **14**, 1022 (1965).
- 87 Wilhelm, F., Angelakeris, M., Jaouen, N., Pouloupoulos, P., Papaioannou, E. T., Mueller, C., Fumagalli, P., Rogalev, A. & Flevaris, N., "Magnetic moment of Au at Au/ Co interfaces: A direct experimental determination". *Physical Review B* **69**, 220404 (2004).
- 88 Wilhelm, F., Pouloupoulos, P., Kapaklis, V., Kappler, J.-P., Jaouen, N., Rogalev, A., Yaresko, A. & Politis, C., "Au and Fe magnetic moments in disordered Au-Fe alloys". *Physical Review B* **77**, 224414 (2008).
- 89 Bartolomé, J., García, L., Bartolomé, F., Luis, F., López-Ruiz, R., Petroff, F., Deranlot, C., Wilhelm, F., Rogalev, A. & Bencok, P., "Magnetic polarization of noble metals by Co nanoparticles in M-capped granular multilayers (M= Cu, Ag, and Au): An x-ray magnetic circular dichroism study". *Physical Review B* **77**, 184420 (2008).
- 90 Banerjee, S., Raja, S., Sardar, M., Gayathri, N., Ghosh, B. & Dasgupta, A., "Iron oxide nanoparticles coated with gold: enhanced magnetic moment due to interfacial effects". *Journal of Applied Physics* **109**, 123902 (2011).
- 91 Pouloupoulos, P., Wilhelm, F., Wende, H., Ceballos, G., Baberschke, K., Benea, D., Ebert, H., Angelakeris, M., Flevaris, N. & Rogalev, A., "X-ray magnetic circular dichroic magnetometry on Ni/Pt multilayers". *Journal of Applied Physics* **89**, 3874 (2001).

- 92 Fullerton, E. E., Stoeffler, D., Ounadjela, K., Heinrich, B., Celinski, Z. & Bland, J., "Structure and magnetism of epitaxially strained Pd (001) films on Fe (001): experiment and theory". *Physical Review B* **51**, 6364 (1995).
- 93 Hung, H., Luo, G., Chiu, Y., Chang, P., Lee, W., Lin, J., Lee, S., Hong, M. & Kwo, J., "Detection of inverse spin Hall effect in epitaxial ferromagnetic Fe₃Si films with normal metals Au and Pt". *Journal of Applied Physics* **113**, 17C507 (2013).
- 94 Siemens, W., "On the increase of electrical resistance in conductors with rise of temperature and its application to the measure of ordinary and furnace temperatures; also on a simple method of measuring electrical resistances". *Proc. Roy. Soci. Lond* **19**, 443 (1871).
- 95 Wheatstone, C., "An Account of Several New Instruments and Processes for Determining the Constants of a Voltaic Circuit". *Philosophical Transactions of the Royal Society of London* **4**, 469 (1837).
- 96 Choi, G.-M., Moon, C.-H., Min, B.-C., Lee, K.-J. & Cahill, D. G., "Thermal spin-transfer torque driven by the spin-dependent Seebeck effect in metallic spin-valves". *Nature Physics* **11**, 576 (2015).
- 97 Kittel, C., "On the theory of ferromagnetic resonance absorption". *Physical Review* **73**, 155 (1948).
- 98 Farle, M., "Ferromagnetic resonance of ultrathin metallic layers". *Reports on Progress in Physics* **61**, 755 (1998).
- 99 Bloembergen, N. & Wang, S., "Relaxation effects in para-and ferromagnetic resonance". *Physical Review* **93**, 72 (1954).

- 100 Arias, R. & Mills, D., "Extrinsic contributions to the ferromagnetic resonance response of ultrathin films". *Physical review B* **60**, 7395 (1999).
- 101 Sklenar, J., Zhang, W., Jungfleisch, M. B., Jiang, W., Chang, H., Pearson, J. E., Wu, M., Ketterson, J. B. & Hoffmann, A., "Driving and detecting ferromagnetic resonance in insulators with the spin Hall effect". *Physical Review B* **92**, 174406 (2015).
- 102 Zhou, Z., Trassin, M., Gao, Y., Gao, Y., Qiu, D., Ashraf, K., Nan, T., Yang, X., Bowden, S. & Pierce, D., "Probing electric field control of magnetism using ferromagnetic resonance". *Nature communications* **6** (2015).
- 103 Zhou, X. & Adeyeye, A., "Magnetostatic spin wave modes in trilayer nanowire arrays probed using ferromagnetic resonance spectroscopy". *Physical Review B* **94**, 054410 (2016).
- 104 Schoen, M. A., Shaw, J. M., Nembach, H. T., Weiler, M. & Silva, T. J., "Radiative damping in waveguide-based ferromagnetic resonance measured via analysis of perpendicular standing spin waves in sputtered permalloy films". *Physical Review B* **92**, 184417 (2015).
- 105 Mitchell, P., Layadi, A., VanderVen, N. & Artman, J., "Direct observation of magnetically distinct regions in Co-Cr perpendicular recording media using ferromagnetic resonance". *Journal of applied physics* **57**, 3976 (1985).
- 106 Mizunuma, K., Yamanouchi, M., Sato, H., Ikeda, S., Kanai, S., Matsukura, F. & Ohno, H., "Size dependence of magnetic properties of nanoscale CoFeB–MgO magnetic tunnel junctions with perpendicular magnetic easy axis observed by ferromagnetic resonance". *Applied Physics Express* **6**, 063002 (2013).

- 107 Yang, T., Suto, H., Nagasawa, T., Kudo, K., Mizushima, K. & Sato, R., "Readout method from antiferromagnetically coupled perpendicular magnetic recording media using ferromagnetic resonance". *Journal of Applied Physics* **114**, 213901 (2013).
- 108 Suto, H., Kudo, K., Nagasawa, T., Kanao, T., Mizushima, K. & Sato, R., "Three-dimensional magnetic recording using ferromagnetic resonance". *Japanese Journal of Applied Physics* **55**, 07MA01 (2016).
- 109 Brataas, A., Tserkovnyak, Y., Bauer, G. E. & Halperin, B. I., "Spin battery operated by ferromagnetic resonance". *Physical Review B* **66**, 060404 (2002).
- 110 Plumer, M. L., Van Ek, J. & Weller, D., *The physics of ultra-high-density magnetic recording*. Vol. 41 (Springer Science & Business Media, 2012).
- 111 Bertotti, G. & Mayergoyz, I. D., *The Science of Hysteresis: Physical modeling, micromagnetics, and magnetization dynamics*. Vol. 2 (Gulf Professional Publishing, 2006).
- 112 McDaniel, T. W., "Application of Landau-Lifshitz-Bloch dynamics to grain switching in heat-assisted magnetic recording". *Journal of Applied Physics* **112**, 013914 (2012).
- 113 Stancil, D. D., *Theory of magnetostatic waves*. (Springer Science & Business Media, 2012).
- 114 Gilbert, T. L., "A phenomenological theory of damping in ferromagnetic materials". *IEEE Transactions on Magnetics* **40**, 3443 (2004).
- 115 Landau, L. & Lifshitz, E., "On the theory of the dispersion of magnetic permeability in ferromagnetic bodies". *Phys. Z. Sowjetunion* **8**, 101 (1935).
- 116 Bloembergen, N. & Pound, R., "Radiation damping in magnetic resonance experiments". *Physical Review* **95**, 8 (1954).

- 117 Kambersky, V. & Patton, C., "Spin-wave relaxation and phenomenological damping in ferromagnetic resonance". *Physical Review B* **11**, 2668 (1975).
- 118 Kamberský, V., "On ferromagnetic resonance damping in metals". *Czechoslovak Journal of Physics B* **26**, 1366 (1976).
- 119 Jackson, J. D., *Classical electrodynamics*. 3rd ed. edn, (Wiley, 1999).
- 120 Nembach, H., Silva, T., Shaw, J., Schneider, M., Carey, M., Maat, S. & Childress, J., "Perpendicular ferromagnetic resonance measurements of damping and Landé g-factor in sputtered (Co₂Mn)_{1-x}Ge_x thin films". *Physical Review B* **84**, 054424 (2011).
- 121 Shaw, J. M., Nembach, H. T. & Silva, T., "Damping phenomena in Co₉₀Fe₁₀/Ni multilayers and alloys". *Applied Physics Letters* **99**, 012503 (2011).
- 122 Bilzer, C., Devolder, T., Crozat, P., Chappert, C., Cardoso, S. & Freitas, P., "Vector network analyzer ferromagnetic resonance of thin films on coplanar waveguides: Comparison of different evaluation methods". *Journal of applied physics* **101**, 074505 (2007).
- 123 Schoen, M. A., Thonig, D., Schneider, M. L., Silva, T., Nembach, H. T., Eriksson, O., Karis, O. & Shaw, J. M., "Ultra-low magnetic damping of a metallic ferromagnet". *Nature Physics* (2016).
- 124 Pozar, D. M., *Microwave engineering*. (John Wiley & Sons, 2009).
- 125 Barry, W., "A broad-band, automated, stripline technique for the simultaneous measurement of complex permittivity and permeability". *IEEE Transactions on Microwave Theory and Techniques* **34**, 80 (1986).

- 126 Ding, Y., Klemmer, T. & Crawford, T., "A coplanar waveguide permeameter for studying high-frequency properties of soft magnetic materials". *Journal of applied physics* **96**, 2969 (2004).
- 127 Scholz, W. & Batra, S., "Micromagnetic modeling of ferromagnetic resonance assisted switching". *Journal of Applied Physics* **103**, 07F539 (2008).
- 128 Ertl, O., Hrkac, G., Suess, D., Kirschner, M., Dorfbauer, F., Fidler, J. & Schrefl, T., "Multiscale micromagnetic simulation of giant magnetoresistance read heads". *Journal of applied physics* **99**, 08S303 (2006).
- 129 Smith, N., "Micromagnetic modeling of magnoise in magnetoresistive read sensors". *Journal of Magnetism and Magnetic Materials* **321**, 531 (2009).
- 130 Zhu, J.-G., Zhu, X. & Tang, Y., "Microwave assisted magnetic recording". *IEEE Transactions on Magnetics* **44**, 125 (2008).
- 131 Heinonen, O. & Gao, K., "Extensions of perpendicular recording". *Journal of Magnetism and Magnetic Materials* **320**, 2885 (2008).
- 132 Camley, R., Celinski, Z., Fal, T., Glushchenko, A., Hutchison, A., Khivintsev, Y., Kuanr, B., Harward, I., Veerakumar, V. & Zagorodnii, V., "High-frequency signal processing using magnetic layered structures". *Journal of Magnetism and Magnetic Materials* **321**, 2048 (2009).
- 133 Lou, J., Insignares, R., Cai, Z., Ziemer, K. S., Liu, M. & Sun, N. X., "Soft magnetism, magnetostriction, and microwave properties of FeGaB thin films". *Applied Physics Letters* **91**, 182504 (2007).

- 134 Lu, L., Young, J., Wu, M., Mathieu, C., Hadley, M., Krivosik, P. & Mo, N., "Tuning of magnetization relaxation in ferromagnetic thin films through seed layers". *Applied Physics Letters* **100**, 022403 (2012).
- 135 Woltersdorf, G., Kiessling, M., Meyer, G., Thiele, J.-U. & Back, C., "Damping by slow relaxing rare earth impurities in Ni 80 Fe 20". *Physical review letters* **102**, 257602 (2009).
- 136 Lock, J., "Eddy current damping in thin metallic ferromagnetic films". *British Journal of Applied Physics* **17**, 1645 (1966).
- 137 Scheck, C., Cheng, L. & Bailey, W., "Low damping in epitaxial sputtered iron films". *Applied physics letters* **88**, 252510 (2006).
- 138 Sun, Y., Song, Y.-Y., Chang, H., Kabatek, M., Jantz, M., Schneider, W., Wu, M., Schultheiss, H. & Hoffmann, A., "Growth and ferromagnetic resonance properties of nanometer-thick yttrium iron garnet films". *Applied Physics Letters* **101**, 152405 (2012).
- 139 Feynman, R. P., "There's plenty of room at the bottom". *Engineering and science* **23**, 22 (1960).
- 140 Richter, H., Dobin, A., Heinonen, O., Gao, K., vd Veerdonk, R., Lynch, R., Xue, J., Weller, D., Asselin, P. & Erden, M., "Recording on bit-patterned media at densities of 1 Tb/in² and beyond". *IEEE Transactions on Magnetics* **42**, 2255 (2006).
- 141 Demokritov, S. O. & Hillebrands, B. in *Spin Dynamics in Confined Magnetic Structures I* 65 (Springer, 2002).
- 142 Tamaru, S., Yakushiji, K., Fukushima, A., Yuasa, S. & Kubota, H., "Ultra-high Sensitivity Ferromagnetic Resonance Measurement Based on Microwave Interferometer". *IEEE Magnetics Letters* **5**, 1 (2014).

- 143 Edwards, E. R., Kos, A. B., Weiler, M. & Silva, T. J., "A microwave interferometer of the Michelson-type to improve the dynamic range of broadband ferromagnetic resonance measurements". *IEEE Magnetics Letters* **8**, 1 (2017).
- 144 Bartell, J. M., Jermain, C. L., Aradhya, S. V., Brangham, J. T., Yang, F., Ralph, D. C. & Fuchs, G. D., "Imaging Magnetization Structure and Dynamics in Ultrathin Y₃Fe₅O₁₂/Pt Bilayers with High Sensitivity Using the Time-Resolved Longitudinal Spin Seebeck Effect". *Physical Review Applied* **7**, 044004 (2017).
- 145 Kong, W., Fan, X., Zhou, H., Cao, J., Guo, D., Gui, Y., Hu, C.-M. & Xue, D., "Electrical detection of magnetization dynamics in an ultrathin CoFeB film with perpendicular anisotropy". *Applied Physics Letters* **109**, 182406 (2016).
- 146 Woo, S., Litzius, K., Krüger, B., Im, M.-Y., Caretta, L., Richter, K., Mann, M., Krone, A., Reeve, R. M. & Weigand, M., "Observation of room-temperature magnetic skyrmions and their current-driven dynamics in ultrathin metallic ferromagnets". *Nature materials* (2016).
- 147 Szerenos, K., Kisielewski, J., Maziewski, A. & Stupakiewicz, A., "Photoinduced ultrafast magnetization dynamics in yttrium-iron garnet and ultrathin Co films". *IEEE Magnetics Letters* **7**, 1 (2016).
- 148 Silva, T., Turgut, E., Mathias, S., Grychtol, P., Adam, R., Rudolf, D., Nembach, H., Aeschlimann, M., Schneider, C. & Kapteyn, H. in *Ultrafast Magnetism I* 300 (Springer, 2015).
- 149 Iihama, S., Mizukami, S., Naganuma, H., Oogane, M., Ando, Y. & Miyazaki, T., "Gilbert damping constants of Ta/CoFeB/MgO (Ta) thin films measured by optical detection of precessional magnetization dynamics". *Physical Review B* **89**, 174416 (2014).

150 Wang, D.-S., Lai, S.-Y., Lin, T.-Y., Chien, C.-W., Ellsworth, D., Wang, L.-W., Liao, J.-W., Lu, L., Wang, Y.-H. & Wu, M., "High thermal stability and low Gilbert damping constant of CoFeB/MgO bilayer with perpendicular magnetic anisotropy by Al capping and rapid thermal annealing". *Applied Physics Letters* **104**, 142402 (2014).